Signal Processing Methods for Ultra High Resolution Scatterometry

Brent Allen Williams

A dissertation submitted to the faculty of
Brigham Young University
in partial fulfillment of the requirements for the degree of

Doctor of Philosophy

David G. Long, Chair
Karl F. Warnick
Brian D. Jeffs
Richard W. Christiansen
Dah-Jye Lee

Department of Electrical and Computer Engineering

Brigham Young University

August 2010

ABSTRACT

Signal Processing Methods for Ultra High Resolution Scatterometry

Brent Allen Williams

Department of Electrical and Computer Engineering

Doctor of Philosophy

This dissertation approaches high resolution scatterometry from a new perspective. Three related general topics are addressed: high resolution σ^0 imaging, wind estimation from high resolution σ^0 images over the ocean, and high resolution wind estimation directly from the scatterometer measurements. Theories of each topic are developed, and previous approaches are generalized and formalized. Improved processing algorithms for these theories are developed, implemented for particular scatterometers, and analyzed. Specific results and contributions are noted below.

The σ^0 imaging problem is approached as the inversion of a noisy aperture-filtered sampling operation–extending the current theory to deal explicitly with noise. A maximum aposteriori (MAP) reconstruction estimator is developed to regularize the problem and deal appropriately with noise. The method is applied to the SeaWinds scatterometer and the Advanced Scatterometer (ASCAT). The MAP approach produces high resolution σ^0 images without introducing the ad-hoc processing steps employed in previous methods. An ultra high resolution (UHR) wind product has been previously developed and shown to produce valuable high resolution information, but the theory has not been formalized. This dissertation develops the UHR sampling model and noise model, and explicitly states the implicit assumptions involved. Improved UHR wind retrieval methods are also developed. The developments in the σ^0 imaging problem are extended to deal with the nonlinearities involved in wind field estimation. A MAP wind field reconstruction estimator is developed and implemented for the SeaWinds scatterometer. MAP wind reconstruction produces a wind field estimate that is consistent with the conventional product, but with higher resolution. The MAP reconstruction estimates have a resolution similar to the UHR estimates, but with less noise. A hurricane wind model is applied to obtain an informative prior used in MAP estimation, which reduces noise and ameliorates ambiguity selection and rain contamination.

Keywords: scatterometry, image reconstruction, irregular sampling, aperture-filtered sampling, wind, ambiguity selection, hurricane, maximum aposteriori estimation, inverse problems

ACKNOWLEDGMENTS

I want to thank my wife, Linnae, for all her support, and my adviser, Dr. Long, for years of good council.

Table of Contents

List of Tables

List of Figures

Chapter 1

Introduction

1.1 Overview

A scatterometer is a radar that measures the normalized radar cross section σ^0 of the surface of the Earth. The σ^0 measurements contain information about the condition of the surface (e.g., the roughness). Scatterometers are principally designed to measure large scale ocean surface winds. Over the ocean the σ^0 measurements are related to the wind velocity through an empirically derived geophysical model function (GMF). Because the GMF is nonlinear, multiple different wind vectors can map to the same σ^0 value. When estimating the wind from multiple scatterometer measurements, the nonlinearity results in multiple wind vector estimates called ambiguities. It is difficult to determine which ambiguity is correct from the σ^0 data alone. The problem of ambiguity selection is often considered separately from the problem of wind estimation (i.e., finding the multiple ambiguous solutions).

Although scatterometers are designed for large scale wind estimation, other types of products may be derived from the σ^0 measurements. For example, high resolution wind products and σ^0 images can be derived from the raw σ^0 measurements. These products provide valuable additional information for geoscience over land, sea ice, and oceans.

1.2 Motivation

Conventional scatterometry is based on simplified processing methods. Standard processing employs a drop-in-the-bucket griding technique, which assumes a simplified measurement process. With this griding method, both σ^0 imaging and wind vector estimation can be approached as point-wise parameter estimation problems (i.e., for σ^0 imaging, a single σ^0 value is estimated separately for each grid element, while for wind estimation, a single wind vector is estimated separately for each wind vector cell).

Actual σ^0 measurements contain information from scatterers distributed over an area, which generally extend into multiple σ^0 griding bins or wind vector cells (WVCs). Each σ^0 measurement represents the superposition of the returns from scatterers over an area weighted by the spatial response function (or aperture function) of the measurement. The aperture functions of different measurements overlap irregularly and have different shapes. Griding methods solve a simplified problem for both σ^0 imaging and wind estimation. These methods ignore the aperture functions entirely. Furthermore, griding methods assume that the scattering return is uniform over the area of each σ^0 bin or WVC. However, within a particular σ^0 bin or WVC there may be a significant variability among the scatterers. Subcell variability that is unaccounted for results in estimation biases. Also, the resolution of griding methods is limited.

σ^0 imaging methods have been developed to exploit the irregular overlap of the spatial response functions. These methods, classified as reconstruction algorithms, attempt to invert a more general measurement sampling operation. Several σ^0 image reconstruction methods have been developed, all based on a noise-free linear model. Processing methods have been developed to ameliorate the effects of scatterometer noise, but these approaches are somewhat ad-hoc.

An ultra high resolution (UHR) wind product has been produced for the SeaWinds scatterometer that employs σ^0 reconstruction methods to obtain σ^0 images from which the wind is estimated on a point-wise basis (i.e., a single wind vector is estimated separately for each pixel of the reconstructed σ^0 images). In order to estimate the wind point-wise, the scatterometer noise model is modified in UHR processing. This modification simplifies the problem, but also changes it. The errors and artifacts introduced by this modification are difficult to analyze without understanding the more general problem.

1.3 Approach

Although scatterometry is a relatively well-established field, there are several theoretical and practical issues that have not been considered in detail. This dissertation provides the theoretical framework for solving the scatterometer σ^0 imaging and wind estimation problems in a more general manner, not relying on the approximations conventionally made to simplify the problems. The general σ^0 measurement sampling operation is presented and a more general approach to the inverse problem is developed, which deals with the sampling operation and the scatterometer noise. Both the scatterometer σ^0 imaging problem, and the wind field estimation problem are addressed. The σ^0 imaging problem is approached as a noisy linear inverse problem, extending previous scatterometer image reconstruction methods to appropriately account for noise. The wind inversion problem is approached as a noisy, nonlinear inverse problem. A general method is proposed to estimate the wind field at high resolution from the σ^0 measurements, which appropriately accounts for spatial correlation imposed by the sampling. The new developments unify the various approaches to wind scatterometry as simplified special cases of the more general solution. The dissertation also formalizes the UHR wind retrieval theory and develops methods to ameliorate noise and ambiguity selection.

1.4 Summary of Results

The material in this dissertation is addressed in one published journal article [1], two submitted journal papers [2] [3], and several conference papers [4] [5] [6] [7]. The contributions include both new theoretical contributions as well as development and analysis of improved processing algorithms.

The first journal paper [1] develops a method to improve UHR wind estimates in hurricanes. The material of this paper is presented in Chapter 6. A maximum aposteriori (MAP) estimation method for point-wise UHR wind retrieval is developed, which improves ambiguity selection and reduces the variability of the estimates. A hurricane wind field model is derived from SeaWinds data and this is used to obtain the prior distribution required for MAP estimation. The MAP approach produces wind field estimates that by design are more consistent with what is expected for hurricanes, while also providing estimates of useful hurricane parameters such as the eye center location.

The second journal paper [2] considers the theory of aperture-filtered sampling and reconstruction, develops a new reconstruction approach, and applies the method to the scatterometer image reconstruction problem. The material in [2] is presented in Chapters 3 and 4 of the dissertation. This new approach provides a theoretical way to obtain enhanced pixel resolution in image reconstruction. For scatterometry, the σ^0 imaging problem is generally ill-posed (i.e., the sampling operation is underdetermined). This results in an effective resolution that may differ from the pixel resolution used in reconstruction. The new reconstruction approach is applied to the SeaWinds scatterometer and the Advanced Scatterometer (ASCAT) and the results are compared to previous methods. The new procedure produces results comparable with the previous methods, but without the ad-hoc processing steps.

The third journal article [3] extends the linear reconstruction approach developed in [2] to wind field estimation, appropriately handling the nonlinearity introduced by the GMF. This paper is the subject of Chapter 7. Theoretical issues are explored and a MAP wind field reconstruction estimator is developed for scatterometry. The method is applied to the SeaWinds scatterometer and the results are compared to the conventional and UHR products. The MAP reconstruction method produces a high resolution product that is consistent with the conventional and UHR products. The MAP estimates have resolution similar to the UHR estimates, but the variability of the estimates is greatly reduced.

1.5 Outline

The dissertation is organized by topic into two major parts. The first part addresses scatterometer σ^0 imaging. The second part discusses scatterometer wind estimation. Chapter 2 presents scatterometry background and reviews previous approaches to the scatterometer σ^0 imaging and wind estimation problems. Chapter 3 presents the theory required to generalize the σ^0 imaging problem as a noisy linear inverse problem. Chapter 4 explores the application of the inverse problem approach to the scatterometer σ^0 imaging or reconstruction problem, focusing on the SeaWinds and ASCAT scatterometers. Chapter 5 formalizes the ultra high resolution (UHR) wind estimation approach. Chapter 6 applies a point-wise MAP estimation approach to improve wind and rain field estimates in hurricanes. Chapter 7 considers the scatterometer wind estimation problem as a noisy, nonlinear inverse problem and applies a wind field reconstruction approach to the SeaWinds scatterometer. Finally, Chapter 8 summarizes the results and contributions. For convenience, a list of acronyms is provided in Appendix A.

Chapter 2

Background

2.1 Introduction

A scatterometer is a radar that transmits microwave frequency energy at the Earth's surface from an aircraft or spacecraft and measures the power of the echo return. Pulse compression or range/Doppler processing is employed to partition the power measurement of a single echo into sub-elements called 'slices' [8] [9] [10]. These slice measurements represent the superposition of the echos over an area on the Earth's surface scaled by the spatial response function, as well as radiometric emissions and receiver noise. The spatial response function for a range/Doppler slice is a combination of the antenna gain pattern and signal processing. Scatterometers also make noise-only measurements. These measurements are subtracted from the power (signal-plus-noise) measurements and scaled by the parameters in the radar equation to produce a noisy measurement of the normalized radar cross section σ^0 [11].

The σ^0 signal describes the scattering properties of the Earth's surface, assuming atmospheric effects are negligible. σ^0 varies with the composition, roughness, and state of the surface. For the same type of material on the surface, a brighter return or higher σ^0 value indicates a rougher surface (on the order of the wavelength of the scatterometer) [11]. Since wind roughens the ocean surface (inducing capillary waves), the σ^0 measurements are related to the surface winds [12]. Stronger returns are obtained from looking directly into or away from the direction of the wind, while weaker returns are obtained for azimuth angles 90^0 from the wind direction. Thus, the wind vector field (speed and direction) over the ocean can be estimated from the scatterometer measurements if there is sufficient azimuth diversity among the measurements. Scatterometers make measurements at different azimuth angles, incidence angles, and possibly different polarizations and frequencies. Large scale ocean vector wind measurement is the principle mission of space-borne scatterometers; however, high resolution products can be obtained [7].

Other useful information over land and ice can be derived from the scatterometer measurements. For example, scatterometer data provides valuable information for studies of vegetation [13] [14], sea ice [15] [16] [17] [18], glacial ice sheets [19] [20] [21], and desert sand dunes [22] [23]. Investigation of the scatterometer data for these land and ice applications is based on σ^0 image products.

This dissertation considers both σ^0 imaging applications over land and ice, and wind applications over the ocean. This chapter provides an overview of previous approaches to scatterometry as applied to σ^0 imaging and wind estimation. More detailed background is provided in subsequent chapters as needed.

2.2 σ^0 Imaging

Each part of a scatterometer swath is observed multiple times at different geometries for each σ^0 measurement. Since the different scatterometer measurements overlap in space, they may be combined to produce σ^0 images. For land and ice applications, measurements from multiple passes can be combined assuming that the surface is stationary over the time spanned by the different passes. Using multiple passes provides a more dense sampling of the surface, which reduces the effects of noise and allows for a finer resolution than possible with a single pass. Note that the σ^0 measurements vary with azimuth angle, incidence angle, polarization, and frequency. Since scatterometers make measurements with different geometries and possibly polarizations and frequencies, these measurements of different ‘flavors’ cannot generally be combined directly to produce a single image. Conventional land and ice σ^0 imaging methods assume that azimuth variation is negligible and combine only measurements of a given frequency and polarization. If there is a wide incidence angle variation among the measurements, the relationship

$$10\log_{10}\sigma = \mathcal{A} + \mathcal{B}(\theta - \theta_0) \tag{2.1}$$

is assumed. Here, $\mathcal{A}$ represents the incidence angle normalized σ^0 in dB, θ is the incidence angle of the measurement, θ_0 is the reference incidence angle, and $\mathcal{B}$ is a parameter [24]. When this relationship is assumed, two different types of images are created from the scatterometer data: an incidence angle normalized σ^0 image (or $\mathcal{A}$ image), and a $\mathcal{B}$ image. Figure 2.1 shows an $\mathcal{A}$ image and a $\mathcal{B}$ image of Antarctica made from data obtained by the NASA scatterometer (NSCAT). The $\mathcal{A}$ image varies with different types of surfaces (e.g., sea ice or glacial ice). The $\mathcal{B}$ image indicates the slope of σ^0 with incidence angle.

Multiple methods of creating σ^0 images from scatterometer data have been developed. The rest of this section overviews the different approaches.

2.2.1 Gridding and AVE

A simple imaging method is to grid up a region on the globe into bins and average each measurement of a given type whose center falls into a given bin. As stated above, gridding methods effectively neglect the aperture functions and assume that the scatterers are uniform over each bin. Furthermore, the spatial resolution is limited.

Another simple method that allows for finer scale details to be resolved is a weighted average where the weighting functions are the aperture functions (or spatial response functions) of the measurements. This is the basis of the averaging (AVE) algorithm [24]. For the linear case this method is equivalent the applying a row normalized adjoint as a pseudo-inverse of the sampling operation. Although this method can produce higher resolution images than gridding, the resolution enhancement from the AVE method is also limited.

2.2.2 Reconstruction

Reconstruction is an imaging approach that can greatly enhance the resolution of the σ^0 images. This involves inverting the sampling operation. For this method, noise is neglected and image reconstruction is approached as an operator inverse problem. Constrained optimization is employed to minimize a constraint on the σ^0 image $\sigma^0(x)$ subject to a consistent forward projection through the sampling operator. This can be expressed more precisely as

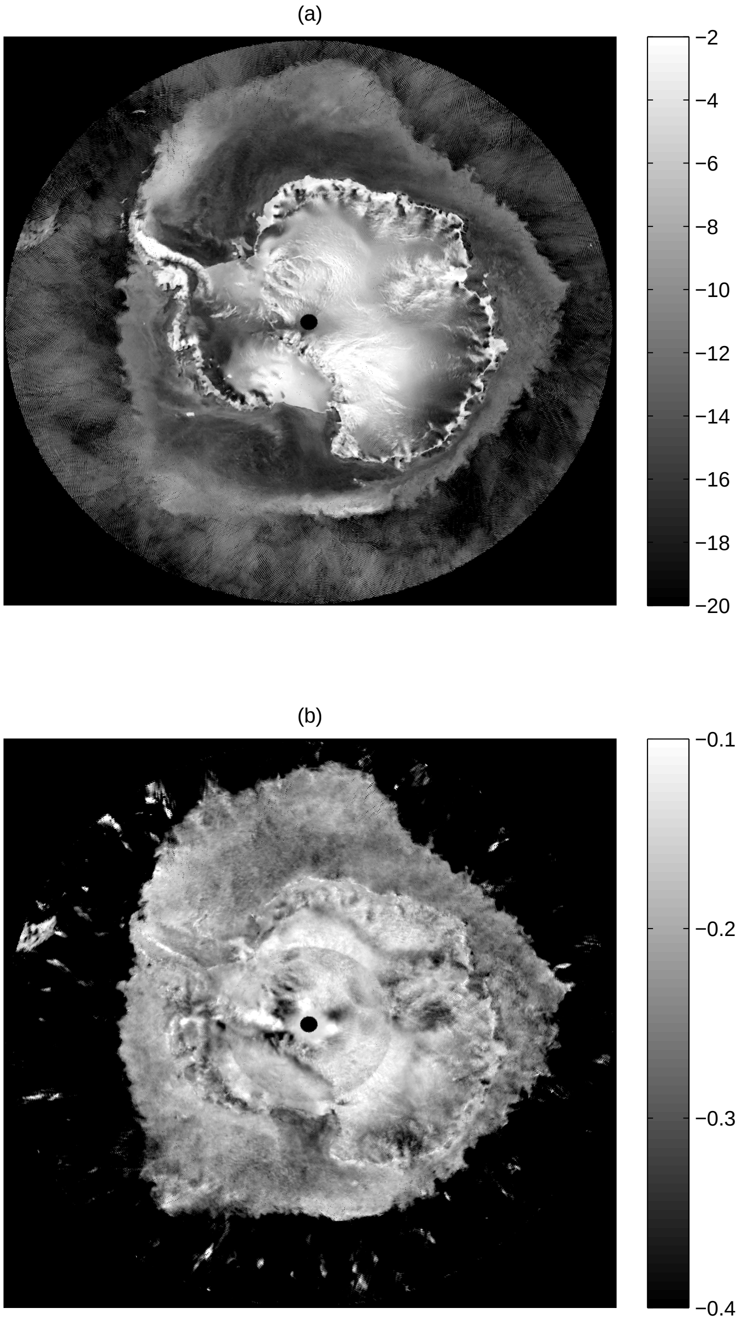

Figure 2.1: An $\mathcal{A}$ (a) image and $\mathcal{B}$ (b) image of Antarctica derived from NSCAT.

minimize $C(\sigma^0(x))$,

subject to $\vec{\sigma}^0_m = \mathcal{H}\sigma^0(x)$

where x represents a two-dimensional spatial variable, $\vec{\sigma}^0_m$ is the vector of scatterometer measurements, $\mathcal{H}$ is the sampling operator, and $C(\sigma^0(x))$ is a constraint. Two particular constraints have been discussed in the literature: the minimum norm constraint (i.e., $C(\sigma^0(x)) = ||\sigma^0(x)||$), and the maximum entropy constraint (i.e., $C(\sigma^0(x)) = \int \sigma^0(x) \log \sigma^0(x) dx$). Instead of gradient search methods, other iterative methods have been adopted for image reconstruction purposes [25].

AART, MART, and SIR

The additive algebraic reconstruction technique (AART) is an iterative method that converges to the minimum norm solution. Although this reconstruction technique is appropriate for the noise-free case and for additive white Gaussian noise, for noisy scatterometer measurements the maximum entropy constraint results in a less noisy σ^0 image estimate. The multiplicative reconstruction technique (MART) is an iterative method that maximizes the entropy of the σ^0 image. For scatterometer applications, the MART algorithm has been adapted based on simulation and Monte Carlo methods to converge faster with less noise. These modifications result in the scatterometer image reconstruction (SIR) technique [25].

Figure 2.2 displays a gridded image, an AVE image, and a SIR image of Greenland derived from h-pol measurements from the SeaWinds instrument on the QuikSCAT platform. The gridded product is pixelated while the AVE and SIR images are more smooth. The SIR image shows more detail than the AVE image which is slightly more blurry.

Note that although these methods are appropriate for the noise free-case, the modifications made to deal with noise in the SIR algorithm are somewhat ad-hoc. A theoretically more appropriate method for image reconstruction that deals with noise explicitly is proposed in Chapter 4. This method is based on solving the noisy inverse problem.

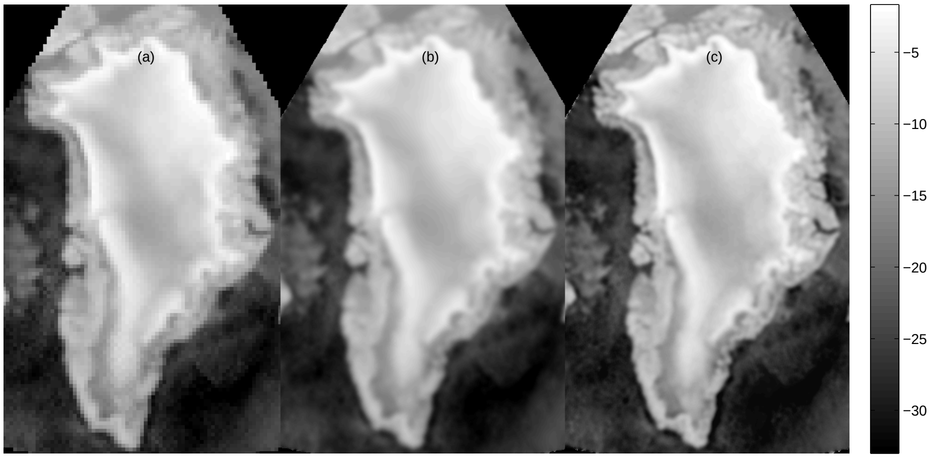

Figure 2.2: A gridded (a), AVE (b), and SIR (c) image of Greenland derived from the SeaWinds scatterometer using h-pol measurements.

2.3 Wind Scatterometry

For wind scatterometry over the ocean, the σ^0 fields (images) are related to the surface wind vector at the particular location through the geophysical model function (GMF). The GMF is an empirically derived mapping, and there are different GMFs for different operating frequencies. The two most common operating frequencies for space-borne scatterometers are C-band and Ku-band. The C-band CMOD5 GMF is currently used for the operational advanced scatterometer ASCAT [9] [26]. For the SeaWinds (or QuikSCAT) scatterometer, which was operation until the fall of 2009, the Ku-band Qmod3 and Qmod4 GMFs are often used [8]. Figure 2.3 plots the Qmod4 for a particular look geometry (an incidence angle of 46 degrees) as a function of wind speed and relative azimuth angle χ. The relative azimuth angle is the angle between the wind direction and the azimuth angle of the measurement (e.g., $\chi = 0$ means looking directly into the wind). Notice that the σ^0 value is a nonlinear function of both speed and direction. The direction modulation is sinusoidal, which results in multiple possible wind solutions (ambiguities) for a given set of measurements.

Because of the possibility of several wind ambiguities, the problem of wind retrieval has been approached in two separate steps: a wind estimation step in which the multiple

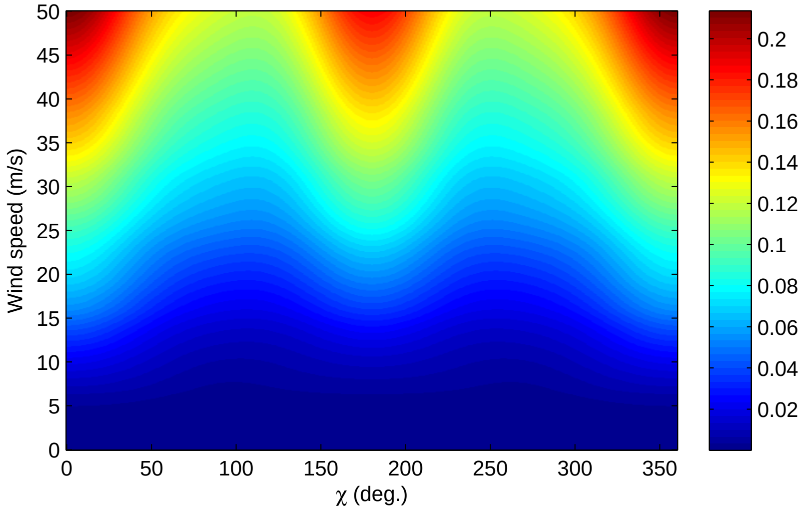

Figure 2.3: σ^0 value (in linear space) as a function of wind speed and relative azimuth angle χ according to the Qmod4 GMF for h-pol measurements at an incidence angle of 46 degrees.

ambiguities are obtained, and an ambiguity selection step. The problem of ambiguity selection is particularly difficult from the scatterometer data alone. Nevertheless, useful results can be obtained by assuming structure for the wind fields (see Chapter 6 and Appendix D). Conventional ambiguity selection algorithms employ external wind field estimates, such as numerical weather predictions, to select appropriate ambiguities.

Unlike the conventional σ^0 reconstruction approach that neglects noise, the wind estimation problem conventionally employs an estimation theory approach. That is, the noisy σ^0 measurements are modeled as random variables whose distributions or probability density functions (pdfs) are functions of the wind. The wind is thus a parameter of the joint distribution of the measurements, which parameter is to be estimated. Such methods rely on an appropriate noise model.

2.3.1 Noise Model

A noisy scatterometer measurement σ_m^0 can be modeled as a Gaussian random variable with a mean of the true or noise-free σ^0 value (i.e., $E\sigma_m^0 = \sigma_t^0$ where E is the expectation) and a variance that is a quadratic function of the mean (i.e., $\xi^2 = \alpha(\sigma_t^0)^2 + \beta\sigma_t^0 + \gamma$ where α, β, and γ are functions of the scatterometer design and the measured noise power) [27]

[28]. This noise model accounts for receiver noise as well as fading. Uncertainty in the GMF can also be modeled by modifying the random variable (i.e., changing the parameters of the quadratic form of the variance) [29]. Conventionally, each measurement is assumed to be statistically independent and so the pdf for the vector of σ^0 measurements $\vec{\sigma}^0_m$ can be expressed as [30]

$$f(\vec{\sigma}^0_m|\vec{\sigma}^0_t) = \prod_i \frac{1}{\sqrt{2\pi}\xi_i} \exp\left\{ \frac{-(\sigma^0_{m,i} - \sigma^0_{t,i})^2}{2\xi_i^2} \right\} \tag{2.2}$$

where i indexes the different scatterometer measurements.

Several methods have been developed for wind estimation from scatterometer measurements. These methods can be classified as point-wise and field-wise approaches. Point-wise approaches estimate each wind vector independently of the others, while field-wise methods simultaneously estimate the entire wind field over a region.

2.3.2 Drop-in-the-bucket Gridding

The standard wind retrieval method is a drop-in-the-bucket gridding technique. For this method each σ^0 measurement whose center falls into a 50km, 25km, or 12.5km wind vector cell (WVC) is used to estimate a single wind vector for that WVC [31]. This method is appropriate for the standard resolution products, but for wind fields with significant fine scale features, other processing methods may be more appropriate.

2.3.3 UHR Wind Processing

Ultra high resolution wind field estimates have been obtained for the SeaWinds scatterometer by reconstructing several σ^0 fields by combining measurements of a given flavor (i.e., with a given polarization and frequency, and a similar geometry) onto a 2.5km grid. These σ^0 images of different flavors are used to estimate the wind on a point-wise basis [7]. This procedure allows fine scale features to be resolved, but the noise level or variability of the estimates is significantly higher than the lower resolution products. Furthermore, ambiguity selection is much more difficult at higher resolutions and higher noise levels.

Figure 2.4 shows images of the wind field estimates from QuikSCAT data using standard drop-in-the-bucket techniques and using the UHR approach. Although the UHR estimate is noisier, the UHR speed field shows important details that are not represented in the conventional product.

Although the UHR method has been applied for years, the details of the theory have not been formalized. The UHR method is formalized in Chapter 5. Chapter 6 and Appendix D develop variations of the UHR wind retrieval method that can ameliorate noise issues and ambiguity selection.

2.3.4 Field-wise Wind Estimation/Model-based Approaches

Although point-wise approaches provide useful results, they neglect spatial correlation among the wind at different WVCs. Field-wise methods, which estimate the entire wind field simultaneously, can account for this spatial structure. Field-wise methods have been explored in the past as model-based estimation [32] [33] [34]. That is, the wind is assumed to be in the span of a wind field model and the model parameters are estimated form the σ^0 measurements. The wind estimate is then obtained by making an instantiation of the model with the estimated model parameters. If the model is relatively low order, the number of field-wise ambiguities may be much fewer than the number of point-wise ambiguities. However, the lower the order, the more structure is imposed on the wind field estimates. That is, the space of possible solutions is small, roughly equating to smooth or low resolution wind field estimates.

Assuming a low-order wind field model may be inappropriate for some applications, such as those requiring fine scale features to be resolved. Alternatively, the wind field may be made discrete on a fine grid and the wind vector at every WVC may be estimated simultaneously. This approach is the subject of Chapter 7.

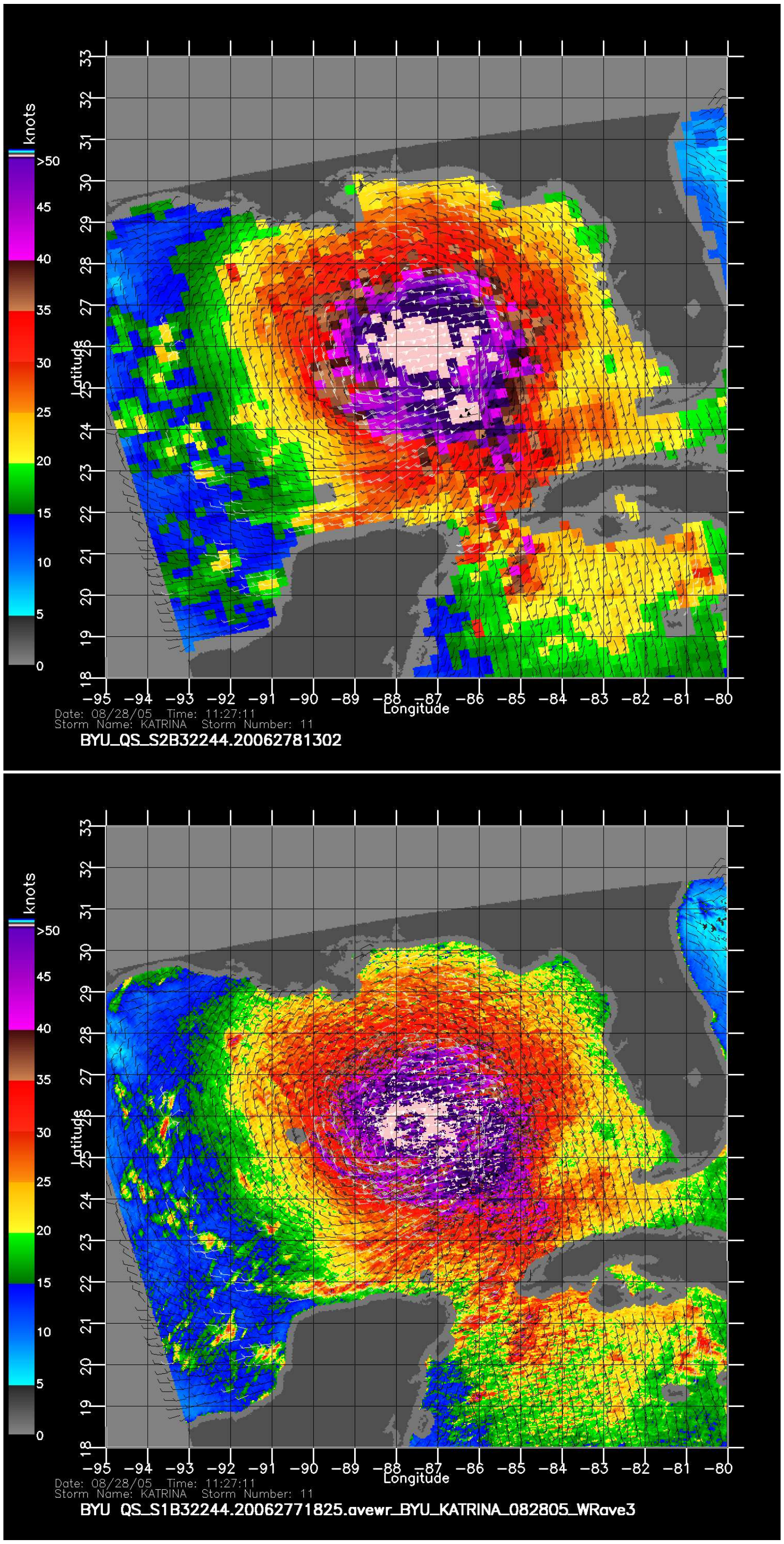

Figure 2.4: Standard resolution wind vector field plotted over the standard speed field (top) and UHR speed field (bottom) for a QuikSCAT observation of Hurricane Katrina.

Chapter 3

Aperture-filtered Sampling and Reconstruction Theory

The σ^0 imaging problem can be expressed as a linear inverse problem, neglecting the nonlinear incidence angle dependence. This chapter presents the theory required to reconstruct the σ^0 images from noisy σ^0 measurements (Chapter 7 extends the theory to include the nonlinearities involved in wind estimation). This chapter generalizes irregular sampling and reconstruction theory to deal with irregular shaped aperture functions and develops a reconstruction estimator that can appropriately deal with noise. It is shown that reconstruction from irregular, bandlimited aperture-filtered samples is expressible as a noisy, discrete linear inverse problem, which has a standard solution in the framework of estimation theory [35] and inverse problems theory [36]. The material in this chapter is part of a journal article submitted for publication [2].

3.1 Introduction

In signal processing, a continuous signal is often converted into a discrete signal so that it can be digitally processed. In most applications the continuous signal is forced to be bandlimited by low-pass filtering the signal before it is uniformly sampled at a rate at least twice the bandlimit or cut-off frequency of the low-pass filter. The sampling formulation is mathematically equivalent to performing a series of inner products of the signal with regularly spaced Dirac delta functions. This is ‘conventional sampling’.

There are, however, practical applications where the sampling cannot be represented by this regular scheme. For example, a scatterometer converts a received electric field which varies continuously in time and space into a sequence of power measurements which are positioned irregularly in space and represent the spatially averaged power over the antenna pattern. The antenna pattern acts as a distributed aperture function (rather than a delta function), which varies in shape and location for different measurements. In this chapter I provide a more general sampling formulation that allows for irregular placement of the samples and for sampling with distributed aperture functions of different shapes. The samples produced using distributed aperture functions are called ‘aperture-filtered samples’ to distinguish them from conventional samples.

It is well known in the signal processing community that bandlimited signals can be reconstructed from regularly spaced samples that satisfy the Nyquist criterion [37]. More generally, it can also be shown that bandlimited signals can be reconstructed from irregularly-spaced samples as long as the samples are sufficiently dense [38] [39] [40]. Similar results can be obtained from samples made with distributed sampling functions (i.e., aperture functions) [40] [41]. These results apply to general bandlimited signals but more practical results may be found for the finite discrete case (i.e., bandlimited periodic signals). Furthermore, previous results assume a signal bandlimit so that the signal can be reconstructed, but do not consider what can be done if the signal has a higher bandlimit than can be recovered from a particular sampling.

Several reconstruction operations have been developed for irregular samples that even include specific types of aperture-filtered sampling schemes [40] [41]. These approaches have been adapted for scatterometer image reconstruction [25] to reconstruct images of the normalized radar cross section σ^0. However, the resolution or grid spacing of the reconstructed fields is chosen somewhat arbitrarily and the reconstruction operations are based on methods derived for the noise-free case. With noise, a reconstruction estimator that explicitly uses the noise model can produce a more appropriate result (i.e., an estimate with a lower bias or variability).

This chapter explores signal reconstruction from irregularly-spaced aperture-filtered samples focusing on bandlimited periodic signals. The question of what types of signals are recoverable from a particular sampling is addressed. The chapter also considers signal recovery from noisy aperture-filtered samples. A reconstruction estimator based on maximum a posteriori probability (MAP) estimation is developed to deal appropriately with noise and to recover the conventional samples of the signal with low variability.

The chapter is organized as follows. Section 3.2 examines and contrasts conventional, irregular, and aperture-filtered sampling theories. Section 3.3 explores inverse operators and the reconstructible subspace determined by the forward and inverse operations. Section 3.4 discusses estimation from noisy samples.

3.2 Sampling

Sampling is the process of converting a continuous-index signal, such as a scalar- or vector-valued function, into a discrete-index signal, termed a sequence. In a Hilbert space (i.e., a complete vector space with an inner product defined [35]) sampling can be represented as a series of inner products with sampling functions [37]. This section contrasts conventional regular sampling, irregular sampling, and sampling with irregularly-spaced aperture functions (i.e., aperture-filtered sampling) in a Hilbert space.

3.2.1 Sampling Formulations

In conventional sampling theory, the sampling of a continuous-index signal $s(x)$ in a Hilbert space can be represented by performing an inner product with a Dirac delta function centered at the sample location x_n for regularly spaced samples (i.e., for the one-dimensional case $x_n = nT_s$ where T_s is the sample spacing and n is an integer) to produce a sequence in which each sample represents the value of the original signal at the corresponding sample location [37]. This formulation also applies to irregular sampling with irregularly placed x_n's. The sampling operation can be written as a vector of inner products

$$\vec{s} = \begin{bmatrix} s[x_1] \\ \vdots \\ s[x_N] \end{bmatrix} = \begin{bmatrix} \int \delta(x - x_1) s(x) dx \\ \vdots \\ \int \delta(x - x_n) s(x) dx \end{bmatrix} \tag{3.1}$$

where $\vec{s}$ is the vector of samples of the continuous-index signal, and N is the total number of samples. While in theory N may be infinite, for all practical applications N must be finite. In this formulation $s[x_n]$ is the value of $s(x)$ evaluated at $x = x_n$.

Note that if $s(x)$ is bandlimited to ω_0 then the delta functions may be replaced with sinc functions, $\text{sinc}(\omega_0(x - x_n)) = \frac{\sin(\pi\omega_0(x-x_n))}{\pi\omega_0(x-x_n)}$, and the same result obtained. Also, if the signal is bandlimited and periodic, the delta functions may be replaced with Dirichlet kernels, $D(\omega_0(x - x_n)) = \frac{\sin((2\omega_0+1)(x-x_n)/2)}{(2\omega_0+1)\sin((x-x_n)/2)}$, with the integration only over one signal period. For regular sampling of bandlimited signals the original continuous-index signal can be reconstructed with sinc-function interpolation, while Dirichlet-kernel interpolation recovers bandlimited periodic signals. These interpolation operations are equivalent to low-pass filtering [37].

More generally, the delta functions in Eq. 3.1 can be replaced with arbitrary aperture functions $A_n(x)$ which may have a different functional form (shape) for each sample. This produces a more general sampling operation

$$\vec{g} = \begin{bmatrix} \int A_1(x)s(x)dx \\ \vdots \\ \int A_N(x)s(x)dx \end{bmatrix} \tag{3.2}$$

where $\vec{g}$ represents the aperture-filtered samples. We use the notation $\vec{g}$ instead of $\vec{s}$ to represent the aperture-filtered samples since the samples do not necessarily represent the value of the original signal at a particular location due to the aperture function.

It can be shown that if the aperture functions are bandlimited, the sampling operation can be expressed as (see Appendix B.1)

$$\vec{g} = \begin{bmatrix} \vec{A}_1^T\vec{s} \\ \vdots \\ \vec{A}_N^T\vec{s} \end{bmatrix} = \mathbf{A}\vec{s} \tag{3.3}$$

where $\mathbf{A}$ is a matrix operator that operates on the conventional, regularly spaced samples $\vec{s}$ of the bandlimited version of the continuous-index signal $s(x)$, the $\vec{A}_n$'s represent conventional sampling of the bandlimited aperture functions, and T represents the transpose (or Hermitian transpose for complex signals). The same result is obtained if $s(x)$ is bandlimited even if each $A_n(x)$ is not bandlimited where the rows of $\mathbf{A}$ are conventional samples of bandlimited versions of the aperture functions. Moreover, if $s(x)$ or each $A_n(x)$ is bandlimited and periodic then $\mathbf{A}$ is a finite-dimensional matrix and can be analyzed with standard linear algebra (see Appendix B.1).

Having a discrete mapping from the conventional samples to the aperture-filtered samples allows a unique approach to reconstruction. Reconstructing the original signal can be thought of as first reconstructing $\vec{s}$ from $\vec{g}$ by inverting $\mathbf{A}$, and then performing Dirichlet-kernel interpolation on the reconstructed $\vec{s}$ to produce the continuous-index signal $s(x)$.

3.2.2 Discrete Processing of Continuous-index Signals

In practice, sampling is limited to a finite number of samples. With a finite number of samples, the signal may be *treated* as bandlimited and periodic. Constraining the signal to be bandlimited and periodic may seem restrictive. Nevertheless as noted below, in most practical applications the bandlimited and periodic assumption is appropriate. That is, most practical signals can be approximated arbitrarily close by a bandlimited, periodic signal. This approximation may introduce aliasing, but the aliasing is negligible if the bandlimit and the period are chosen appropriately.

Note a few fundamental qualities of signals in practical applications: they have finite extent, have finite energy, are bounded, and are generally continuous (or at least piece-wise continuous). Signals with finite extent can be extended to be periodic and if they satisfy the Dirichlet conditions can be exactly represented by the Fourier Series. The Dirichlet conditions for the Fourier Series require that a periodic signal be absolutely integrable over a signal period, be of bounded variation, and have finitely many discontinuities in order to be represented exactly by the Fourier Series [42]. Most practical signals satisfy these conditions. Furthermore, above some frequency the energy in the Fourier Series of the signal must decrease toward zero since practical signals have finite energy. This suggests that for a practical signal a bandlimit and period may be chosen such that a bandlimited, periodic version of the signal exists where the approximation error is sufficiently small. Thus, for practical applications any signal can be approximated arbitrarily close by a bandlimited, periodic signal.

For the rest of the chapter, we restrict our attention to periodic bandlimited signals, although the bandlimit may be arbitrarily high. This greatly simplifies the math and allows the reconstruction analysis to be performed using linear algebra instead of real analysis, i.e., using matrix theory instead of linear operator theory.

The choice of the signal bandlimit and period is problem dependent. A general signal period may be chosen as anything larger than the extent of the data or region that is to be processed. Once a signal period is selected, an appropriate bandlimit can be imposed. If the signal bandlimit or signal spectrum is known, a bandlimit may be chosen to minimize aliasing, but for many applications no a priori knowledge about the signal is available. Nevertheless, there may be a fundamental bandlimit imposed by the aperture functions. If every aperture function is bandlimited by some ω_0 then the sampling operation on the continuous-index signal is equivalent to the same sampling operation on the bandlimited version of the signal. This implies that no portion of the signal with frequency content higher than ω_0 can be recovered. Assuming a bandlimit that is the highest bandlimit of the aperture functions is sufficient to recover all the information about the signal that is possible from the aperture-filtered samples alone. If the aperture-functions are not bandlimited then a high bandlimit may be chosen so that the resulting aliasing is sufficiently small. The bandlimit and period determine the number of conventional samples required to represent the continuous-index signal, and the sample spacing (i.e., pixel resolution).

3.3 Noise-free Reconstruction

This section explores reconstruction from noise-free aperture-filtered samples. The ability to reconstruct the original signal depends on whether the mapping $\mathbf{A}$ is reversible. The system $\vec{g} = \mathbf{A}\vec{s}$ represents a linear system of equations. Depending on the structure of the forward operator $\mathbf{A}$ the system may be fully determined, overdetermined, or underdetermined.

Whether the sampling matrix $\mathbf{A}$ is overdetermined, fully determined, or underdetermined depends on the density of the samples, the signal bandlimit, the signal period, and the linear independence of the aperture functions. A fully determined system results if the number of aperture-filtered samples is the same as the number of conventional samples required to represent the bandlimited, periodic signal and if each aperture-function is linearly independent. An overdetermined system results if there are more aperture-filtered samples than the required number of conventional samples and the number of linearly independent aperture functions is the number of required conventional samples. An underdetermined system results if there are fewer aperture-filtered samples than the required number of conventional samples or if the number of linearly independent aperture functions is less than the required number of conventional samples.

Reconstructing the conventional samples $\vec{s}$ from the aperture-filtered samples $\vec{g}$ requires a slightly different reconstruction operation for each of the three cases: fully determined, overdetermined, and underdetermined. First, the aperture-filtered samples are converted to conventional samples, then for each case the reconstruction of the continuous-index signal is performed using Dirichlet-kernel interpolation with the reconstructed conventional samples

$$\hat{s}(x) = \sum_{x_n} \hat{s}[x_n] D(\omega_0(x - x_n)) \tag{3.4}$$

where $\hat{s}[x_n]$ is the reconstructed conventional sample corresponding to location x_n and $D(\omega_0(x - x_n))$ is the Dirichlet kernel with the same period and bandlimit imposed on the signal.

Each of the three cases is considered below and the conditions required for exact reconstruction from the aperture-filtered samples are explored. Optimum inverse mappings that enable reconstruction of $\vec{s}$ from $\vec{g}$ are also derived. It is shown that if the sampling matrix is overdetermined or fully determined, exact reconstruction of any bandlimited signal (or recovery of the bandlimited version) is possible. If the system is underdetermined then not every bandlimited signal is recoverable, nevertheless, the subclass of signals that can be recovered is explored. While the sampling can often be designed in a way such that the sampling matrix is fully or overdetermined, in other applications, such as scatterometer image reconstruction where scatterometer systems are not designed for imaging purposes, underdetermined systems often result. Thus, we focus much of the discussion exploring the underdetermined case.

3.3.1 Fully-Determined Case

For the case where the system is fully determined, the matrix **A** is square and full rank. In this case **A** is invertible and there exists a unique mapping from the aperture-filtered samples $\vec{g}$ back to the conventional samples $\vec{s}$. Therefore, if **A** is an $N \times N$ full-rank matrix then every signal that can be represented by N conventional samples can be reconstructed from the aperture-filtered samples.

For this case, the discrete reconstruction operation is

$$\hat{\vec{s}} = \mathbf{A}^{-1}\vec{g} \tag{3.5}$$

where $\hat{\vec{s}}$ represents the reconstructed conventional samples and $\mathbf{A}^{-1}$ is the standard matrix inverse of **A**. The continuous-index signal is reconstructed using Eq. 3.4 where $\hat{\vec{s}}$ is the vector form of the reconstructed discrete signal $\hat{s}[x_n]$.

3.3.2 Overdetermined Case

The overdetermined case occurs when **A** has more rows than columns and is full-row rank. By throwing out redundant samples, a consistent overdetermined system may be transformed into a determined system without discarding information. That is, the aperture-filtered samples that correspond to the linearly dependent rows of **A** may be discarded, producing a mapping from $\vec{s}$ to the remaining aperture-filtered samples that is square and full rank and represents a fully-determined system. Thus, if **A** is an $M \times N$ matrix with N linearly independent rows then every signal that can be represented by N conventional samples can be reconstructed from the aperture-filtered samples.

When **A** is overdetermined, instead of discarding data, a least-squares inverse may be used for the reconstruction operation. A least-squares approach produces the same result in theory but is numerically more stable. Furthermore, with additive white Gaussian noise the least-squares inverse produces the minimum-variance unbiased estimate of the conventional samples (see Appendix B.2.1). Applying the least-squares inverse results in the discrete reconstruction operation

$$\hat{\vec{s}} = (\mathbf{A}^T\mathbf{A})^{-1}\mathbf{A}^T\vec{g}. \tag{3.6}$$

The continuous-index signal is reconstructed using Eq. 3.4.

3.3.3 Underdetermined Case

The underdetermined case occurs if the row rank of **A** is less than the number of conventional samples required to represent the bandlimited signal. For this case there is no one-to-one mapping that maps the range space of **A** back to the entire domain of **A**. If **A** is an underdetermined $M \times N$ matrix, then only some signals that can be represented by N conventional samples may be reconstructed. That is, there is a subspace of the domain of **A** over which an inverse mapping (i.e., a pseudo-inverse) may be defined. Here, restrictions on the class of signals are investigated that allow every signal of the class to be recovered for a given sampling.

Any class of recoverable signals is a subspace of the signal space. Figure 3.1 illustrates the spaces associated with the sampling matrix, **A**, and a pseudo-inverse, $\mathbf{A}^p$. Here, $\mathbf{A} : \mathcal{S} \rightarrow \mathcal{G}$ where $\mathcal{S}$ is the domain and represents the Hilbert space of conventional discrete signals $\vec{s}$ and $\mathcal{G}$ is the co-domain and represents the Hilbert space of aperture-filtered signals $\vec{g}$. Although **A** is not invertible over the entire domain and co-domain, the domain and co-domain may be restricted so that **A** is bijective over these subspaces. In this case there is a unique inverse over the subspaces and this inverse is a pseudo-inverse of **A**. A pseudo-inverse of **A** is any mapping $\mathbf{A}^p : \mathcal{G} \rightarrow \mathcal{S}$ (see Fig. 3.1) such that $\mathbf{A}^p\mathbf{A}\vec{s} = \vec{s}$ for every $\vec{s}$ in the range space of $\mathbf{A}^p$ where $\mathbf{A}^p$ need not be a linear operator.

There are generally several different subspaces over which we can define an inverse of **A**. Each such subspace is associated with a different pseudo-inverse. Restricting the co-domain to any subspace of the range space of **A** is sufficient to constrain **A** to be a surjection. Moreover, deciding which subspace of $\mathcal{S}$ to use is equivalent to imposing a signal model. That is, a signal model may be chosen whose range space spans a subspace of $\mathcal{S}$. Estimating the parameters of a low-order model and then constructing an estimate of the

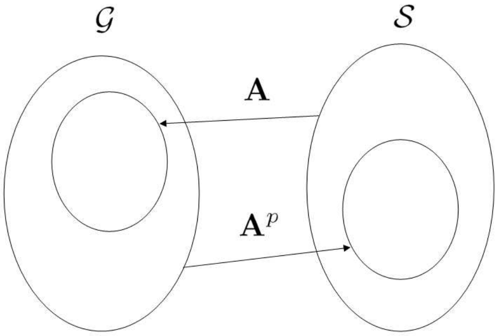

Figure 3.1: Spaces associated with the sampling matrix $\mathbf{A}$ and the mapping $\mathbf{A}^p$.

signal $\vec{s}$ using the model and the estimated parameters constitutes an inverse of $\mathbf{A}$ over a subspace of $\mathcal{S}$ (i.e., a pseudo-inverse of $\mathbf{A}$).

Note that some pseudo-inverses may not preserve all the information in the aperture-filtered samples. In order to preserve all the information in the samples, the pseudo-inverse must be reversible by $\mathbf{A}$. This information preserving constraint can be thought of as requiring each point in the range space of $\mathbf{A}$ to map back to itself through the pseudo-inverse followed by the forward projection (i.e., $\mathbf{A}\mathbf{A}^p\vec{g} = \vec{g}$ for all $\vec{g}$ in the range space of $\mathbf{A}$). This property does not necessarily hold for every pseudo-inverse mapping $\mathbf{A}^p$, but there always exists a pseudo-inverse mapping that is information preserving (e.g., see the constrained optimization approach described below).

An information-preserving pseudo-inverse can be defined using constrained optimization, i.e., by choosing for each point $\vec{g}$ in the range space of $\mathbf{A}$ the point $\vec{s}$ in $\mathcal{S}$ that maps to the point $\vec{g}$ that minimizes some metric $d(\vec{s}, \vec{z})$ defined in $\mathcal{S}$. In other words, we minimize $d(\vec{s}, \vec{z})$ subject to $\vec{g} = \mathbf{A}\vec{s}$ where $d(\vec{s}, \vec{z})$ is a metric that represents the distance between the vector $\vec{s}$ and some predetermined vector $\vec{z}$. $\vec{z}$ may be some particular signal (e.g., an expected signal) for which we want to find the closest signal $\vec{s}$ to $\vec{z}$ that produces the obtained aperture-filtered samples. For many applications $\vec{z}$ is taken to be $\vec{0}$ so that $d(\vec{s}, \vec{0})$ is a vector norm.

Using the L_2-norm, $d(\vec{s}, \vec{0}) = ||x||_2^2$, produces the Moore-Penrose pseudo-inverse [35]. This constrained optimization approach using the L_2-norm is similar to what is done in the additive algebraic reconstruction technique (AART) and Grochenig's irregular sampling theorem [40] [25]. Another common constraint used for non-negative signals is to maximize the signal entropy, $-\sum_i s_i \log(s_i)$, subject to $\vec{g} = \mathbf{A}\vec{s}$. This is the basis for the multiplicative algebraic reconstruction technique (MART) and the scatterometer image reconstruction (SIR) algorithm [25]. Although the L_2-norm constraint results in a linear pseudo-inverse, a different constraint may produce a nonlinear pseudo-inverse for a linear sampling operator. Formulating the pseudo-inverse as a constrained optimization problem is powerful because it can be extended to general linear and nonlinear operators.

It is interesting to consider what happens to signals that are not in the range space of the pseudo-inverse when the sampling and reconstruction processes are applied. The reconstructed signal is guaranteed to be in the range space of the pseudo-inverse; however, if the original $\vec{s}$ is not in the range space of the pseudo-inverse, the reconstructed signal may not be the closest signal to $\vec{s}$ in the range space of the pseudo-inverse. This is a generalized form of aliasing. For a linear pseudo-inverse, if some portions of the original signal that are orthogonal to the range space of the pseudo-inverse are not mapped to zero in the sampling operation, the energy in those components is preserved in the aperture-filtered samples. The pseudo-inverse then erroneously maps this energy into its range space. Unless everything orthogonal to the range space of the pseudo-inverse is in the null space of the sampling operator, the pseudo-inverse introduces aliasing. The Moore-Penrose pseudo-inverse forces signal components orthogonal to its range space to be in the null space of the sampling operator and is therefore an anti-aliasing pseudo-inverse, whereas reconstruction using the MART or SIR algorithms may introduce aliasing and may even result in multiple solutions. This is illustrated in the numerical example in Section 3.3.4.

If nothing is known about the signal, we suggest that the structure to impose on the signal be a function of $\mathbf{A}$ so as to force the pseudo-inverse to be linear, information preserving, and anti-aliasing. Where no a priori knowledge of the signal structure is available and noise is negligible, we propose reconstruction be done using the Moore-Penrose pseudo-inverse.

Using the Moore-Penrose pseudo-inverse implies that for each point in the range space of $\mathbf{A}$, the simplest or lowest energy signal that could have produced the aperture-filtered samples is chosen as the inverse because the Moore-Penrose pseudo-inverse can be obtained by minimizing the L_2-norm as described above. This is consistent with the notion that signals with low energy are easier to produce and more likely to occur in nature than signals with high energy. The Moore-Penrose pseudo-inverse can also be calculated conveniently.

Reconstructing the conventional samples from the aperture-filtered samples using the Moore-Penrose pseudo-inverse is expressed as

$$\hat{\vec{s}} = \mathbf{A}^{\dagger}\vec{g} \tag{3.7}$$

where $\hat{\vec{s}}$ represents the reconstructed conventional samples and $\mathbf{A}^{\dagger}$ is the Moore-Penrose pseudo-inverse of $\mathbf{A}$ defined by

$$\mathbf{A}^{\dagger} = \mathbf{V}_A(\mathbf{\Sigma}_A)^{-T}\mathbf{U}_A^T \tag{3.8}$$

where $\mathbf{U}_A\mathbf{\Sigma}_A\mathbf{V}_A^T$ is the singular value decomposition of $\mathbf{A}$ and $(\mathbf{\Sigma}_A)^{-T}$ is defined as the transpose of $\mathbf{\Sigma}_A$ with the non-zero elements replaced by their reciprocals [35]. The reconstruction of the continuous-index signal is performed using Dirichlet-kernel interpolation with the reconstructed conventional samples as described in Eq. 3.4.

3.3.4 Numerical Example

An illustrative numerical example is now explored where the aperture functions associated with each aperture-filtered sample are bandlimited and all have the same shape but are placed (shifted) irregularly. Suppose that each aperture function is a bandlimited periodic version of a Hann window with period 2π that is bandlimited such that it can be represented with 11 conventional (uniformly placed) samples (see Fig. 3.2). Different sampling schemes are considered to explore the overdetermined, fully-determined and underdetermined cases.

First consider the overdetermined case. Suppose that a signal with period 2π is sampled with 13 aperture functions placed randomly between $-\pi$ and π. Note that the two left most samples are almost on top of each other. Figure 3.3 shows a signal that can be represented by 11 conventional samples along with the 13 randomly placed aperture-filtered samples and the 11 uniformly spaced conventional samples. Note that the aperture-

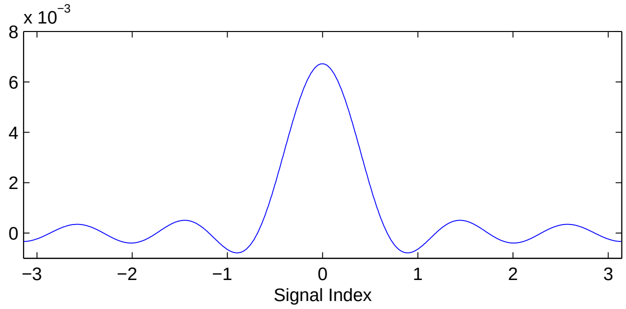

Figure 3.2: Bandlimited Hann window aperture function centered at zero.

filtered samples are placed at the location of the maximum of the irregularly-shifted aperture functions and that the aperture-filtered sample values are not the values of the signal at the sample locations.

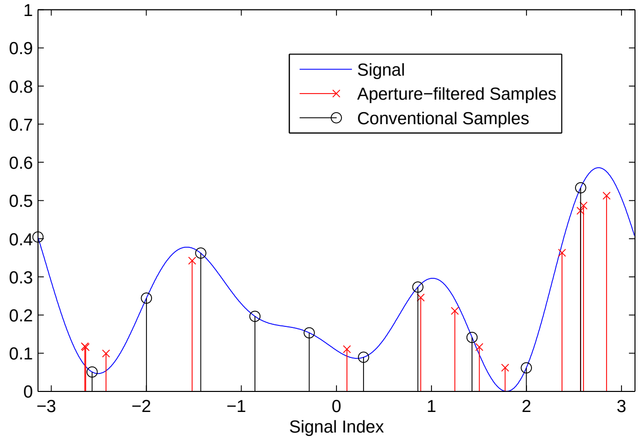

Figure 3.3: Signal, aperture-filtered samples, and conventional samples.

The sampling operator results from stacking the aperture functions into a vector which for this case produces the sampling operator illustrated in Fig. 3.4 (a). Since each aperture function can be represented by 11 conventional samples, the sampling operator can be converted into a discrete sampling matrix using 11 conventional samples of each row. This results in the sampling matrix shown in Fig. 3.4 (b). The sampling matrix is over-determined, meaning that there are more aperture-filtered samples than needed to exactly reconstruct the signal. For this case the least-squares pseudo-inverse exactly recovers the 11 conventional samples that describe the original signal from which Dirichlet-kernel interpolation recovers the original signal. If the signal is not bandlimited so that it can be exactly represented by 11 conventional samples, the bandlimited version of the signal is reconstructed.

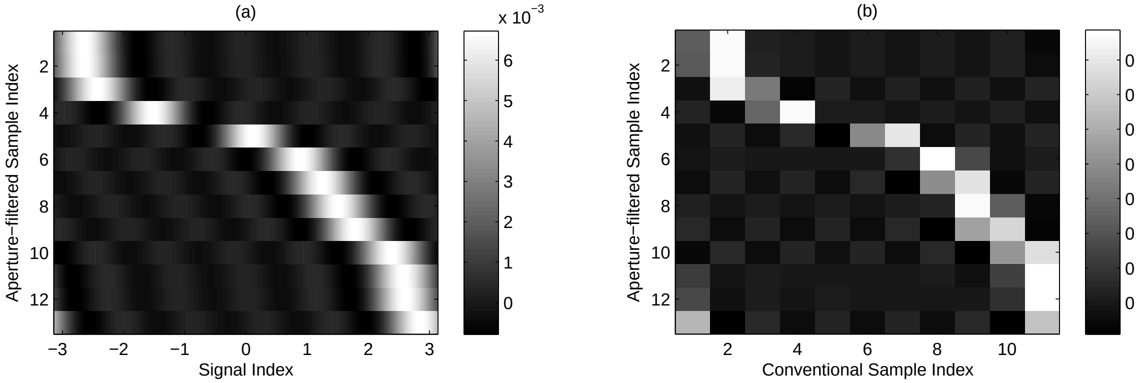

Figure 3.4: (a) Sampling operator for the overdetermined case. (b) Discrete sampling matrix for the overdetermined case. The rows are normalized to sum to unity.

Now consider the fully-determined case. Suppose the same signal as in Fig. 3.3 is sampled, but only with 11 of the aperture-filtered samples. This results in a similar sampling operator and sampling matrix as before but with two fewer rows. As long as the sampling operator is invertible the 11 conventional samples are exactly recovered by applying the inverse to the aperture-filtered samples. In this case the original signal is exactly recovered by Dirichlet-kernel interpolation using the reconstructed conventional samples. As with the overdetermined case if the signal cannot be exactly represented by 11 conventional samples only the bandlimited version of the signal is recovered.

The underdetermined case is much more interesting. Suppose that there are only nine of the aperture-filtered samples (i.e., two more are missing). The resulting sampling matrix is underdetermined. Reconstruction is examined using two different pseudo-inverse operations: the Moore-Penrose pseudo-inverse, and the pseudo-inverse obtained by assuming a bandlimit such that the resulting sampling matrix is full-row rank.

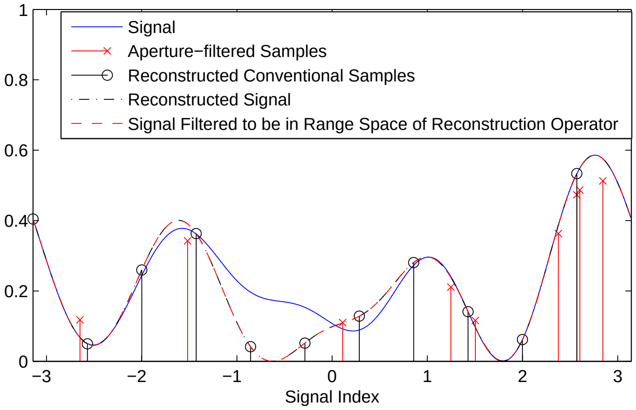

Figure 3.5: Signal, aperture-filtered samples, and reconstructed conventional samples using the Moore-Penrose pseudo-inverse. The reconstructed signal and the signal component in the range space of the adjoint of the sampling operator are also plotted. In this case the sampling matrix is underdetermined.

Applying the Moore-Penrose pseudo-inverse to the aperture-filtered samples and performing Dirichlet-kernel interpolation recovers the portion of the signal in the range space of the adjoint of the sampling operator. Figure 3.5 shows the original signal, the aperture-filtered samples, the reconstructed conventional samples using the Moore-Penrose pseudo-inverse, the reconstructed signal, and the component of the signal in the range space of the adjoint of the sampling operator. Although the original signal is not exactly recovered in this case, the error is relatively small and the component of the signal in the range space of the reconstruction operator is exactly recovered.

Now consider what happens when the conventional thinking is used to reconstruct the signal for the underdetermined case. With the conventional approach it is assumed that the signal is bandlimited and that the bandlimit results in an invertible sampling matrix. For the underdetermined example, this corresponds to assuming that the signal can be represented with 9 conventional samples. If the signal cannot be exactly represented by 9 conventional samples, the original signal is not recovered. In fact, not even the bandlimited version of the signal with the assumed bandlimit is reconstructed. Some portions of the signal with higher frequency content than the assumed bandlimit are not mapped to zero in the sampling operation. This causes aliasing, i.e., the energy from higher frequency components of

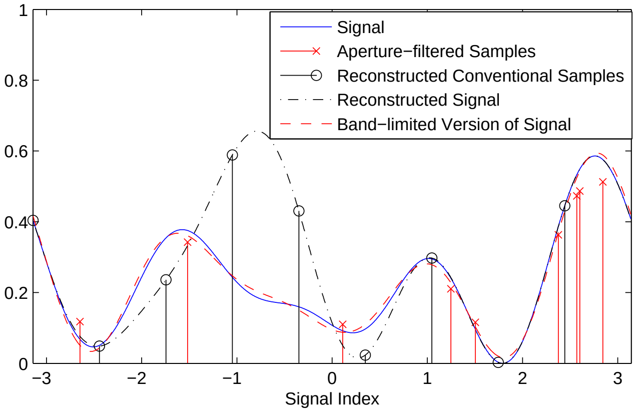

Figure 3.6: Signal, aperture-filtered samples, and reconstructed conventional samples and signal assuming that the signal is bandlimited so that **A** is square. In this case the sampling operator is square and invertible, but aliasing is significant.

the signal is mapped to lower frequency components through the aperture-filtered sampling and reconstruction process. Figure 3.6 shows the signal, the aperture-filtered samples, the reconstructed samples and signal, and the bandlimited version of the signal for the sampling scheme described above assuming that the signal can be represented by 9 conventional samples. Although the reconstructed signal is bandlimited with the assumed bandlimit, it is quite different from the bandlimited version of the original signal. Therefore, assuming an inappropriate bandlimit may result in unexpected errors and artifacts.

3.3.5 Resolution

Given a particular sampling scheme it is of interest to know the resolution of the signals that can be reconstructed. If the sampling matrix is fully determined or overdetermined then the resolution of the reconstructed signal is the spacing between the conventional samples (i.e., the pixel resolution). However, if the sampling matrix is underdetermined, the effective resolution may be lower and may even vary in location (see Appendix E). For a linear sampling operator and linear reconstruction operation, the effective resolution can be determined by how close the round-trip operator $\mathbf{A}^p\mathbf{A}$ is to an identity. Each row i of $\mathbf{A}^p\mathbf{A}$ represents how the energy in any signal at the location x_i gets spread into neighboring locations (i.e., the rows are the point spread functions). Typically, the point spread functions are approximations to the identity, meaning their energy is concentrated near the location of interest (i.e., they look like a bump centered at the location x_i). A measure of the effective resolution can be obtained by evaluating the width of the point spread function. When processing multidimensional data such as images or vector fields, the measure of effective resolution may be a vector or tensor that varies in x.

3.4 Noise

This section considers how noise added to the samples affects the signal recovery. First, a noise model is introduced and optimality criteria are presented. Reconstruction from noisy aperture-filtered samples is explored. Methods of reducing the noise or variability of the estimates are then discussed.

3.4.1 Noise Model and Optimality Criteria

For the noise model, it is assumed that a zero-mean random variable $\vec{\nu}$ is added to the aperture-filtered samples $\vec{g}$. The noisy sampling operation may be written as

$$\vec{g}_\nu = \vec{g} + \vec{\nu} = \mathbf{A}\vec{s} + \vec{\nu} \tag{3.9}$$

where $\vec{\nu}$ is the noise random vector, and $\vec{g}_\nu$ represents the noisy aperture-filtered samples. With noise, a reconstruction estimator of $\vec{s}$ from the noisy $\vec{g}_\nu$ is defined to reconstruct the signal.

We seek an optimal estimator in the sense that the estimates are unbiased and have the minimum covariance of all possible estimators. Depending on the structure of the noise process, the estimator may be linear or nonlinear. A lower bound on the covariance of any unbiased estimator is the Cramer-Rao bound. The unbiased estimator that achieves the Cramer-Rao bound is the optimal estimator.

The Cramer-Rao lower bound on the covariance, $\mathbf{R}(\hat{\vec{s}})$, of any unbiased estimator is the inverse of the Fisher information matrix $\mathbf{J}(\vec{s})$

$$\mathbf{R}(\hat{\vec{s}}) \geq \mathbf{J}(\vec{s})^{-1} \tag{3.10}$$

in the sense that $\mathbf{R}(\hat{\vec{s}}) - \mathbf{J}(\vec{s})^{-1}$ is positive semidefinite where the components of $\mathbf{J}(\vec{s})$ are defined as [35]

$$J_{i,j}(\vec{s}) = E\left(\frac{\partial}{\partial s_i}\log\{f(\vec{g}_\nu|\vec{g})\}\right)\left(\frac{\partial}{\partial s_j}\log\{f(\vec{g}_\nu|\vec{g})\}\right) \tag{3.11}$$

where $f(\vec{g}_\nu|\vec{g})$ is the joint probability density function (pdf) of the noisy samples given the noise-free samples, and s_i and s_j represent the i^{th} and j^{th} components of the noise-free discrete signal $\vec{s}$. This is the minimum covariance that can be obtained with any unbiased estimator, though we note that a biased estimator may produce a lower covariance.

3.4.2 Reconstruction Estimators

In this subsection, reconstruction approaches from noisy data are examined for the case in which the Fisher information matrix is invertible and the case in which it is singular. For each case methods of obtaining estimates with low bias and low expected squared error are explored.

Invertible Fisher Information Matrix

Note that $\mathbf{J}(\vec{s})$ is an $N \times N$ matrix where N is the length of the vector $\vec{s}$. If $\mathbf{A}$ is fully determined or overdetermined, then generally $\mathbf{J}(\vec{s})$ is invertible. If $\mathbf{J}(\vec{s})$ is invertible, then every bandlimited, periodic signal that can be represented by N conventional samples is observable in the sense that the conventional samples may be estimated with finite precision or variance of the estimates from the aperture-filtered samples. If $\mathbf{J}(\vec{s})$ is invertible, then each conventional sample may be estimated directly; however, unless $\mathbf{J}(\vec{s})$ is diagonal, the conventional samples must be estimated simultaneously.

A minimum-variance unbiased estimator is desired; however, in most applications there is no general method to find such an estimator. Nevertheless, maximum-likelihood (ML) estimators are asymptotically unbiased and asymptotically efficient (i.e., minimum variance) [35]. For these reasons we propose that, lacking further information, a ML approach be used to estimate the conventional samples from the noisy aperture-filtered samples when the Fisher information is invertible.

A ML estimate of the conventional samples, $\hat{\vec{s}}$, can be written as

$$\hat{\vec{s}} = \underset{\vec{s}}{\operatorname{argmax}} \{ f(\vec{g}_\nu | \vec{g}) \} \tag{3.12}$$

which is the argument that maximizes the likelihood (i.e., $f(\vec{g}_\nu|\vec{g})$) of obtaining the noisy aperture-filtered samples given the noise-free aperture-filtered samples, where the noise-free aperture-filtered samples are a function of the conventional samples $\vec{g} = \mathbf{A}\vec{s}$. Reconstruction of the continuous-index signal is accomplished via Dirichlet-kernel interpolation from the ML estimates of the conventional samples.

It is interesting to consider the ML estimator with white Gaussian noise. The multivariate Gaussian pdf is

$$f(\vec{g}_\nu|\vec{g}) = \frac{\exp\left\{-\frac{1}{2}(\vec{g_v} - \mathbf{A}\vec{s})^T \mathbf{R}^{-1} (\vec{g_v} - \mathbf{A}\vec{s})\right\}}{(2\pi)^{\frac{M}{2}} |\mathbf{R}|^{\frac{1}{2}}} \tag{3.13}$$

where M is the number of noisy aperture-filtered samples (i.e., the length of $\vec{g_v}$), which may be greater than N (i.e., the length of $\vec{s}$) for an overdetermined system. If the noise is white then $\mathbf{R} = \sigma^2\mathbf{I}$, where σ^2 is the noise power. It can be shown that with white Gaussian noise the ML estimates are the minimum-variance unbiased estimators of the conventional samples and that they are the same estimators as the linear estimators obtained in Section 3.3 for the overdetermined and fully-determined cases (see Appendix B.2.1).

Singular Fisher Information Matrix

If $\mathbf{A}$ represents an underdetermined system then $\mathbf{J}(\vec{s})$ is not invertible. This suggests that the parameters (i.e., the conventional samples) are not observable from the data alone; that is, the conventional samples cannot be estimated with any degree of precision using only the noisy aperture-filtered samples. However, if additional constraints are imposed, such as a signal model or a prior distribution on the signal, estimates of the conventional samples may be obtained.

There are three philosophically different approaches for dealing with unobservable parameters: model-based estimation, variational analysis, and Bayes estimation theory. Each of these methods effectively injects prior information about the signal so that the parameters that are unobservable from the aperture-filtered samples alone become observable using the aperture-filtered samples and the prior information.

For model-based estimation, a signal model is imposed such that the parameters of the model are observable so that the corresponding Fisher information matrix for estimating the model parameters is invertible. The signal is then reconstructed from the model parameter estimates. This method requires imposing a signal model. If some knowledge of the structure of the signal is available, a model that describes the signal structure may be chosen. We may desire, as in Section 3.3, to impose a model that preserves all the information in the aperture-filtered samples and minimizes aliasing.

Variational analysis imposes additional constraints on the ML objective function and simultaneously optimizes some linear combination (usually a convex combination) of the ML objective function with the constraints. This is similar to how the information preserving pseudo-inverse is obtained in Section 3.3. For this method, the constraints can be chosen somewhat arbitrarily. Furthermore, the relative weights assigned to each constraint can also be chosen arbitrarily. Although this is a powerful tool, unless there is good reason to choose particular constraints and relative weights, variational analysis is ad hoc.

Bayes estimation imposes prior information about the signal via a prior distribution of the signal. The general form of a Bayesian estimator modified for our application is [35]

$$\hat{\vec{s}} = \operatorname*{argmin}_{\vec{s}} \left\{ \int L(\vec{s}, \vec{g}_\nu) f(\vec{s}|\vec{g}_\nu) d\vec{s} \right\} \tag{3.14}$$

where $L(\vec{s}, \vec{g}_\nu)$ is a loss function and $f(\vec{s}|\vec{g}_\nu)$ is the conditional posterior distribution. The most common loss functions are the squared error loss function and the uniform loss function. Using a uniform loss function produces a maximum a posteriori probability (MAP) estimator which has as its objective function the ML pdf scaled by the prior distribution. Bayes estimation is extremely powerful, but it implicitly assumes the signal is a random process and it requires knowledge of the signal distribution. Prior distributions can be obtained for particular applications either empirically from a collection of data, theoretically from knowledge of the physical process that produces the signal, or by assuming a maximum-entropy distribution given knowledge of a few qualities of the signal (such as the signal mean, power, spectrum, or region of support).

We take a Bayesian MAP estimation approach to solve the noisy inverse problem when the sampling operator is underdetermined. The MAP estimator can be expressed as

$$\hat{\vec{s}} = \underset{\vec{s}}{\operatorname{argmax}}\{f(\vec{g}_\nu|\vec{g})f(\vec{s})\} = \underset{\vec{s}}{\operatorname{argmax}}\{\log f(\vec{g}_\nu|\vec{g})f(\vec{s})\} = \underset{\vec{s}}{\operatorname{argmax}}\{L_{MAP}\} \tag{3.15}$$

where $f(\vec{s})$ is the prior distribution of $\vec{s}$ and L_{MAP} is the MAP objective function. Using a prior is mathematically equivalent to (although philosophically different from) assuming additional statistically independent data representing noisy conventional samples. That is, performing ML estimation with the aperture-filtered samples and the additional data, whose noise distribution is the prior, results in the exact same expression as the MAP estimator.

The form of the prior depends on the application and what is reasonable to assume about the signal. We leave the discussion on the choice of priors until the particular applications in the sequel.

If the noise process is white and Gaussian and the prior is a zero-mean Gaussian distribution with arbitrarily large variance, the MAP estimator is the Moore-Penrose pseudo-inverse (see Appendix B.2.2). Furthermore, the Moore-Penrose pseudo-inverse produces a minimum-variance unbiased estimate over the range space of $\mathbf{A}^\dagger$.

With a different noise distribution it is generally difficult to verify if the MAP estimator is a minimum-variance unbiased estimator. Nevertheless, since the MAP estimator can be expressed as a ML estimator with additional data (as described above), it can exhibit similar asymptotic qualities. The MAP estimator is a good candidate for many noise distributions, often resulting in low-bias and low-variance estimates.

Resolution Revisited

When the Fisher information matrix is singular, the effective resolution may differ from the pixel resolution. Furthermore, with noise another resolution comes into play–the measurement or radiometric resolution. The measurement resolution is an indicator of the precision or variance of the estimates. The covariance of the estimates provides an indication of both the effective resolution and the measurement resolution. Each row i of the covariance matrix is a function that indicates how much each pixel j is statistically correlated with the pixel at index x_i. The width of these correlation functions indicates the effective resolution of the noise of the estimates for a given location (i.e., how the noise gets filtered or spread out by the estimator). By noise of the estimates we mean the zero-mean random component. That is, the estimate can be expressed as an output signal (i.e., the mean) plus noise (i.e., a zero-mean random variable). The values on the diagonal of the covariance indicate the measurement resolution or how much the estimate at a particular location is correlated with itself. The covariance of the estimates is generally a function of the true signal, the noise, the sampling operation, and the estimator or reconstruction operation.

Note that depending on the noise, both MAP and ML reconstruction estimators may be nonlinear. In this case, the noise may be filtered differently than the signal and so the signal may have a different effective resolution imposed on it than does the noise. The notion of resolution is greatly complicated when considering nonlinear operations. Appendix E considers resolution as applied to nonlinear operators in more detail.

3.4.3 Noise Reduction

The covariance of the estimates may be too large to be useful for some applications. Potential noise-reduction operations include filtering or averaging of the aperture-filtered samples (prefiltering), low-order model-based estimation, Bayes estimation with a more informative prior (i.e., a prior with lower entropy), and filtering of the reconstructed signal (postfiltering). Prefiltering the aperture-filtered samples reduces both the signal power and the noise power, but it is difficult to track which components of the signal and noise are being attenuated. Low-order model-based methods may introduce aliasing. Bayes estimation reduces noise but relies on knowledge of the signal. Postfiltering of the estimates, however, reduces the total noise power and the total signal power in a way that can be tracked and that does not introduce aliasing. Thus, postfiltering may be suitable for reducing the variability of the estimates if the application requires.

3.5 Conclusion

This chapter generalizes sampling and reconstruction theory to deal with irregularly spaced samples made with irregularly shaped aperture functions. It is shown that the aperture functions determine the bandlimit and the resolution of signals that can be recovered. If the sampling operator is underdetermined, then only a subspace of signals is reconstructible. Assuming that the signal has a low bandlimit so that the sampling operation becomes fully determined or overdetermined, which is what is done in irregular sampling theory, results in unexpected artifacts (i.e., a generalized form of aliasing) if the true signal has a higher bandlimit.

The chapter also generalizes reconstruction theory to appropriately deal with noise. Estimators for the special case of white Gaussian noise are derived resulting in the simple linear estimators obtained for noise-free reconstruction. This method also applies for various noise distributions such as the scatterometer noise model. The notions of effective resolution and pixel resolution are also defined and explained.

The linear sampling model and inverse theory in this chapter form the foundation for many results in the remainder of the dissertation. In chapter 7 the linear forward and inverse models are extended to deal with the nonlinearities involved in wind retrieval.

Chapter 4

σ^0 Imaging

This section explores reconstruction from irregular aperture-filtered samples as applied to scatterometer image reconstruction. The material in this chapter is part of a journal article submitted for publication [2]. Previous scatterometer image reconstruction techniques are reviewed, and the scatterometer noise model is stated. The scatterometer MAP reconstruction estimator is obtained and examples from the SeaWinds and ASCAT scatterometers are presented.

4.1 Scatterometer Image Reconstruction

As mentioned in Chapter 2, scatterometers make multiple overlapping measurements of the Earth's surface, and these measurements may be combined to produce σ^0 images. Several imaging methods have been proposed for scatterometer image reconstruction. Perhaps the most simple is to create a gridded product by averaging all measurements whose centers fall into a particular grid element. Gridding produces relatively low resolution images. Another imaging technique employs a weighted average on a higher resolution grid. This is the basis of the averaging (AVE) algorithm [24], which sets each pixel to the average of all the σ^0 measurements, weighted by the value of the respective aperture functions at each pixel. Some common methods that further enhance the resolution are based on the additive algebraic reconstruction technique (AART) or the multiplicative algebraic reconstruction technique (MART) [24] [25]. The AART algorithm is an iterative method which finds the signal that is consistent with the measurements that minimizes the L_2-norm, and it converges to same result as the Moore-Penrose pseudo-inverse method described above. The MART algorithm is also an iterative method, but searches for the signal that is consistent with the measurements that maximizes the signal entropy. The MART algorithm assumes the signal has a single sign (i.e., positive or negative). For the noisy scatterometer σ^0 imaging problem, the MART algorithm tends to produce a less noisy estimate. This led to the scatterometer image reconstruction (SIR) algorithm, which is a normalized version of MART that tends to converge faster with less noise [24] [25].

The optimum sample spacing and optimum bandlimit to use when reconstructing the signal have not been extensively explored in the literature. Nevertheless, a bound on the frequency recoverability is given in [25]. The bound is determined by the sampling density, suggesting that the reconstruction grid resolution be a function of the density of the aperture-filtered samples. However, in order to avoid aliasing, the sample spacing must be determined by the bandlimit, or approximate bandlimit, of the aperture functions rather than by the density of the aperture-filtered samples. The density of the samples is related to the condition of the sampling matrix (whether it is overdetermined, fully determined, or underdetermined) and does not directly impose a bandlimit on the signal.

Scatterometer σ^0 imaging algorithms proposed in the literature [24] [25] are based on noise-free reconstruction operators and do not use knowledge of the noise distribution. Furthermore, the commonly used SIR algorithm is tuned using ad hoc methods in order to reduce the effects of noise and the filtering artifacts imposed by the aperture functions. These ad hoc methods make it difficult to analytically evaluate the quality of the estimates. An estimator that uses the noise distribution can be expected to perform better, is theoretically more appropriate, and allows the quality of the estimates to be analyzed using standard estimation theory tools.

4.2 Scatterometer Noise Model

As scatterometer noise model is presented in Chapter 2. With this model the noisy scatterometer σ^0 measurements are represented as Gaussian random variables where the variances are quadratic functions of the means [27]. This noise distribution embodies the receiver noise as well as fading. Measurements are assumed to be statistically independent.

The noise distribution has the form in Eq. 3.13 where $\mathbf{R}$ is a diagonal matrix and each diagonal element $R_{i,i}$ can be expressed as

$$R_{i,i} = \alpha_i(\vec{g}_i)^2 + \beta_i\vec{g}_i + \gamma_i = \alpha_i(\vec{A}_i^T\vec{s})^2 + \beta_i\vec{A}_i^T\vec{s} + \gamma_i \tag{4.1}$$

where $g_i = \vec{A}_i^T\vec{s}$ is the i^{th} noise-free σ^0 measurement, $\vec{s}$ represents the conventional samples of the continuous-index σ^0 field, and α_i, β_i, and γ_i are the noise parameters for the i^{th} measurement that are a function of the scatterometer design and the measured receiver noise power [27].

4.3 Scatterometer MAP Reconstruction Estimator

Scatterometers are designed for large scale ocean wind vector measurements rather than σ^0 imaging. As a result, scatterometer sampling operators may be underdetermined in imaging applications. Therefore, some signal structure must be imposed in order to estimate the uniform samples of the σ^0 image. Here, we take a Bayesian approach and apply a prior using a maximum a posteriori probability (MAP) estimator. The ML estimator is derived in Appendix B.3.

Reconstruction is accomplished by estimating the conventional (uniformly spaced) samples $\vec{s}$ of the σ^0 field using a MAP estimator. The MAP estimator searches for the conventional samples $\vec{s}$ that maximize the maximum-likelihood function scaled by the prior. This process is equivalent to maximizing the linear combination of the log-likelihood function and the log of the prior. The maximum-likelihood function is the probability density function (pdf) of the noisy σ^0 measurements and the prior is a pdf of the σ^0 image. The MAP log-likelihood objective function is

$$L_{MAP} = -\sum_i \left[\frac{(g_{\nu,i} - \vec{A}_i^T\vec{s})^2}{2R_{i,i}} + 1/2\log\{2\pi R_{i,i}\} \right] + \log f(\vec{s}) \tag{4.2}$$

where $f(\vec{s})$ is the prior pdf.

The local maxima of the MAP objective function can be found by setting the gradient equal to zero and solving the corresponding system of equations. However, the resulting system of equations is somewhat complicated so we use a gradient search method to find a local maximum of Eq. 4.2 near an initial guess. The gradient search method begins with an initial value computed using the AVE algorithm and moves incrementally in the direction of the gradient until convergence to the maxima. The partial derivative of L_{MAP} with respect to the i^{th} component of $\vec{s}$ is

$$\begin{aligned}\frac{\partial L_{MAP}}{\partial s_i} &= \frac{\partial \log f(\vec{g}|\vec{s})}{\partial s_i} + \frac{\partial \log f(\vec{s})}{\partial s_i} \\ &= -\sum_n \frac{\partial}{\partial s_i}\left[\frac{(g_{\nu,n} - \vec{A}_n^T \vec{s}))^2}{2R_{n,n}} + \frac{1}{2}(\log\{2\pi\} + \log\{R_{n,n}\})\right] + \frac{\partial \log f(\vec{s})}{\partial s_i} \\ &= \sum_n -K_n A_n \frac{\partial s_n}{\partial s_i} = -K_i A_i \end{aligned} \tag{4.3}$$

where

$$K_n = \left[\frac{(g_{\nu,n} - \vec{A}_n^T \vec{s}) - (\alpha_n \vec{A}_n^T \vec{s} + \beta_n/2)}{R_{n,n}} + \frac{(g_{\nu,n} - \vec{A}_n^T \vec{s})^2(\alpha_n \vec{A}_n^T \vec{s} + \beta_n/2)}{R_{n,n}^2}\right]. \tag{4.4}$$

4.4 Priors

The form of the prior depends on the application and what is reasonable to assume about the signal. The standard approach is to obtain a prior is using an empirical distribution from a large collection of data. However, because different surfaces (i.e., land, ice, ocean, or vegetation) have such different responses, empirical priors for scatterometer imaging applications are multi-modal and difficult to express as a functional form that can be differentiated.

Another approach to obtain a prior is to employ a maximum-entropy distribution. For scatterometer imaging a one-sided distribution is appropriate since the noise-free σ^0 measurements represent a magnitude. The maximum-entropy one-sided distribution with one parameter is the exponential distribution. The larger the mean of the exponential distribution, the larger the entropy. Thus, we may use an exponential distribution with an arbitrarily large mean to regularize the problem. However, because of the structure of the scatterometer noise, using an exponential prior requires too many iterations for the gradient search algorithm to converge to be practical.

For convenience, we use a log-normal prior with a mean as the AVE image and a tunable variance. The smaller the variance, the closer the estimate is to the smooth AVE image. The larger the variance, the less the result is influenced by the prior. A tunable variance allows a trade-off between resolution enhancement and noise amplification. The prior distribution can be expressed as

$$f(\vec{s}) = \prod_i f(s_i) = \prod_i \frac{1}{2\pi p} \exp\left\{ \frac{-(10\log_{10}(s_{AVE,i}) - 10\log_{10}(s_i))^2}{2p} \right\} \tag{4.5}$$

where i indexes the image pixels, p is the variance tuning parameter, and $s_{AVE,i}$ is the AVE estimate of pixel i in linear space.

4.5 SeaWinds and ASCAT Examples

In this subsection, two-dimensional reconstruction of the σ^0 field from the SeaWinds scatterometer and the Advanced Wind Scatterometer (ASCAT) is explored. Basic information about SeaWinds and ASCAT is presented, the optimal regular sample spacing (i.e., pixel resolution) is derived from the aperture functions, and examples are provided.

SeaWinds is a Ku-band scatterometer that orbits the Earth in a sun-synchronous near-polar orbit. The instrument has a scanning pencil-beam antenna with two beams at different incidence angles and polarizations. The v-pol beam is at a nominal incidence angle of 54 degrees with the h-pol beam at an incidence angle of 46 degrees. This produces a swath with four ‘flavors’ (v-pol fore- and aft-looking and h-pol fore- and aft-looking) in the inner portion of the swath and two flavors in the outer portion of the swath where there is only one beam. The backscatter return from each pulse from each beam is partitioned into several ‘slices’ using range-Doppler processing. Each slice is considered to be statistically independent and each has its own aperture function or slice spatial response function [8].

The ASCAT scatterometer is a C-band v-pol instrument in near polar orbit that has two sets of three stationary fan-beam antennas pointed at different azimuth angles. The system applies a type of pulse compression to obtain range resolution, producing slice σ^0 measurements with a relatively wide range of incidence angles. This sampling results in a swath in which each point is sampled by multiple beams with differing azimuth angles [9].

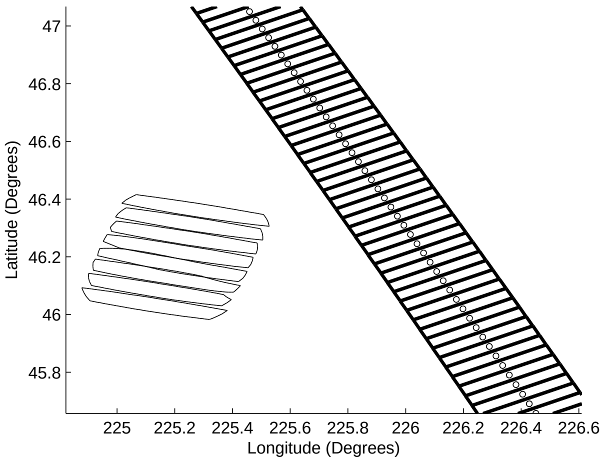

Figure 4.1: Typical slice spatial response functions from SeaWinds and ASCAT for one pulse. The 6dB contours are shown. The boxes with the circles in them are ASCAT slices; the contours on the left are SeaWinds slices.

The σ^0 measurements represent noisy aperture-filtered samples of the two-dimensional σ^0 field. The σ^0 field may be reconstructed using the various slice measurements of a similar flavor (i.e., having the same geometry, frequency, and polarization). Measurements of a given flavor sample the same σ^0 field and can be combined. Furthermore, for land and ice imaging purposes, all slices of a given polarization and frequency may be combined by assuming negligible azimuthal variation and by adjusting the σ^0 values to a common incidence angle [24]. For SeaWinds, the incidence angle adjustment is not necessary since the slices of a given polarization have a similar incidence angle. For ASCAT, incidence angle normalization to 40° is used.

Although SeaWinds and ASCAT cover a large percentage of the Earth's surface daily, the σ^0 fields are generally reconstructed only over particular regions of interest. That is, we are only interested in a region of finite extent which means that the signal and the slice response functions can be assumed to repeat periodically outside the region of interest.

The image grid pixel size is determined by the bandlimit of the slice spatial response functions. Figure 4.1 illustrates typical 6dB contours of the slice spatial response functions for a given pulse from SeaWinds and from ASCAT [43] [44]. For SeaWinds, the 6dB slice contours are approximately 6km in the narrow direction and 25km wide in the long direction. For ASCAT, the contours are about 4.2km in the narrow direction and 20-35km in the long direction. In the following, each of the slice response functions is approximated by a sinc-squared function that has the same 6dB width as the slices in the narrow and long directions. The sinc-squared functions can be represented by regular samples with spacing corresponding to about half the narrow 6dB beam-width. This sample spacing is scaled by a factor of $1/\sqrt{2}$ to allow for the worst-case slice orientation with respect to the gridding axes (i.e., 45°). For SeaWinds, this results in a conventional sample spacing of about $6\text{km}/2\sqrt{2} \approx 2.12\text{km}$ [7]. This verifies that the 2.225km pixel spacing found empirically to be the resolution enhancement limit for SeaWinds slices is appropriate. For ASCAT, the conventional sample spacing is about $4.2\text{km}/2\sqrt{2} \approx 1.5\text{km}$. Note that the range filtering of the σ^0 values performed onboard the ASCAT spacecraft degrades the effective reconstruction resolution. Thus for ASCAT, a coarser conventional sample spacing may be appropriate. From empirical observations it seems that the resolution enhancement limit is about 4 to 6km for ASCAT. To be consistent between the data sets we process both the SeaWinds and ASCAT data on the standard 2.225km grid.

Figure 4.2 shows multi-orbit gridded, SIR, and MAP images of the Amazon made from SeaWinds and ASCAT data. For ASCAT, the incidence-angle-normalized images are plotted. As expected, the ASCAT effective resolution is lower due to the onboard spatial filtering. The results of the reconstruction algorithms, represented by the bottom two rows of images in Fig. 4.2, enhance the resolution compared to the gridded product (top row). The MAP images (bottom row) contain more detail than the SIR images (middle row), although the MAP images seem to be noisier. The noise in the MAP images can be attenuated by filtering the images or by tuning the variance of the log-normal prior (as described below), which can produce images of comparable quality to the SIR images.

Recall that the sampling matrix is typically underdetermined, even when using multiple passes. This may introduce artifacts that are difficult to remove by filtering the estimates. To illustrate this, Fig. 4.5 shows multi-orbit gridded, SIR, and MAP images of the Weddell Sea in Antarctica made from SeaWinds and ASCAT data, where the MAP images are made using an exponential prior with a large mean (i.e., a maximum entropy one-sided distribution). The dark regions of the image are newly formed sea ice, whereas the slightly brighter

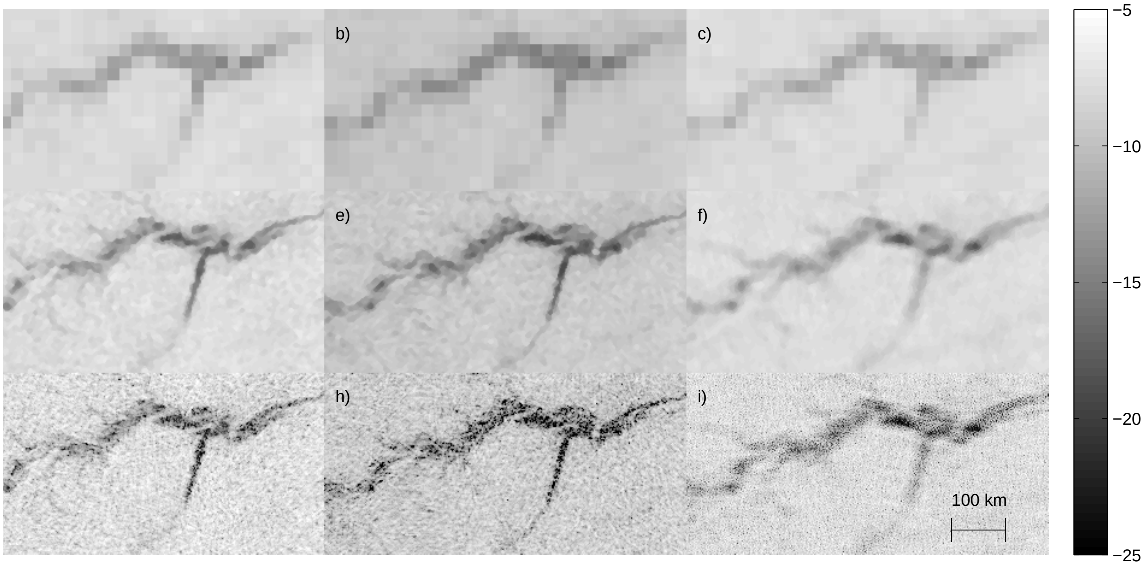

Figure 4.2: Reconstructed σ^0 images (in dB) from SeaWinds and ASCAT over the Amazon using four days worth of data (JD 201-204) in 2008. Images a), b), and c) are gridded images of SeaWinds h-pol, SeaWinds v-pol, and ASCAT, respectively. Images d), e), and f) are SIR images of SeaWinds h-pol, SeaWinds v-pol, and ASCAT, respectively. Images g), h), and i) are MAP images of SeaWinds h-pol, SeaWinds v-pol, and ASCAT, respectively. The diagonal streaks in the river are actual features.

regions are older, thicker sea ice. The brightest regions are glacial ice on the Antarctic peninsula, the Ronne ice shelf, and the large icebergs embedded in the sea ice. Although the MAP images are more sharp than the gridded and SIR images, dark bands appear around large icebergs and the sharp transition between the the glacial continent and the sea ice in the lower left of the MAP images. Furthermore, the MAP images appear to have a higher noise level than the SIR image.

Low-pass filtering reduces the effect of noise but accentuates the ringing around bright targets in the ASCAT image in Fig. 4.5 (f). The ringing or darkening around bright targets in the ASCAT MAP image is an artifact of the low-pass filtering effect imposed by the spatial response functions, exacerbated by the underdetermined system. This ringing structure is similar to Gibbs phenomenon, which occurs when representing a square wave (which has infinite frequency content) with a finite Fourier Series. The ringing is not as apparent in the SeaWinds MAP image because the effective resolution is greater. Although this artifact may be beneficial in some applications such as iceberg detection, the ringing may be ameliorated by imposing a more informative prior that favors desirable signal qualities (see Fig. 4.4). Figure 4.4 shows the MAP results using log-normal priors with means corresponding to the AVE images and relatively low variances. Using the more informative log-normal prior both reduces the noise level and the ameliorates the artifacts, producing results similar to the SIR approach.

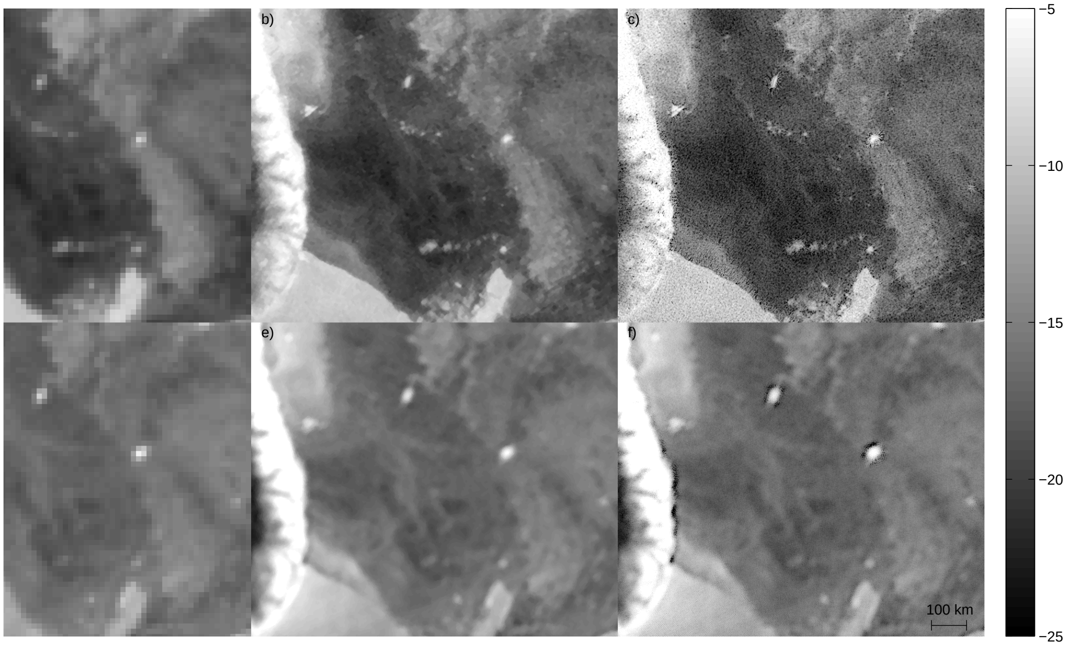

Figure 4.3: Reconstructed σ^0 images (in dB) from SeaWinds and ASCAT over the Weddell Sea in Antarctica using four days worth of data (JD 215-217) in 2008. a) SeaWinds v-pol gridded image. b) SeaWinds v-pol SIR image. c) SeaWinds v-pol MAP image. d) ASCAT gridded image. e) ASCAT SIR image. f) ASCAT MAP image.

The differences in polarization and frequencies between the different data sets (ASCAT and SeaWinds h-pol and v-pol images) allow discrimination between different types of surfaces. Figure 4.5 shows a false color MAP image of a larger region of the Weddell Sea using the same four days worth of data from SeaWinds and ASCAT. The blue region in

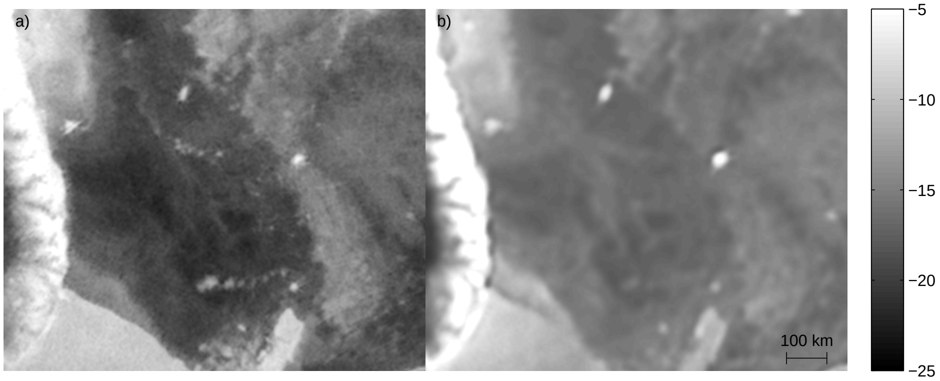

Figure 4.4: Reconstructed σ^0 MAP images (in dB) using an informative prior (log-normal) from (a) SeaWinds and (b) ASCAT over the Weddell Sea in Antarctica using four days worth of data (JD 215-217) in 2008.

the top left corner is open ocean, the purple regions of the image are newly formed sea ice, whereas the tinted yellow regions are older, thicker sea ice. The brighter yellow region in the lower left is the Ronne ice shelf. The bright white regions are glacial ice on the Antarctic peninsula and large icebergs embedded in the sea ice. Combined, the two scatterometers offer more discrimination capability than either alone.

4.6 Conclusion

This chapter approaches scatterometer image reconstruction as the inversion of a noisy aperture-filtered sampling operation, focusing on bandlimited, periodic signals. A theoretically more appropriate reconstruction algorithm is proposed based on MAP estimation, which can reconstruct more detail than the SIR algorithm, but with a higher noise level. The noise in the MAP estimates can be reduced without introducing the ad-hoc methods used in SIR processing but rather by either filtering or using more informative priors. Examples from SeaWinds and ASCAT are presented.

Many measurement applications can be expressed as an aperture-filtered sampling problem where the fields that are sampled by the aperture functions are related by a pointwise nonlinearity. For example, scatterometers sample σ^0 fields with different shaped aperture functions, but over the ocean each measurement with a different look geometry samples

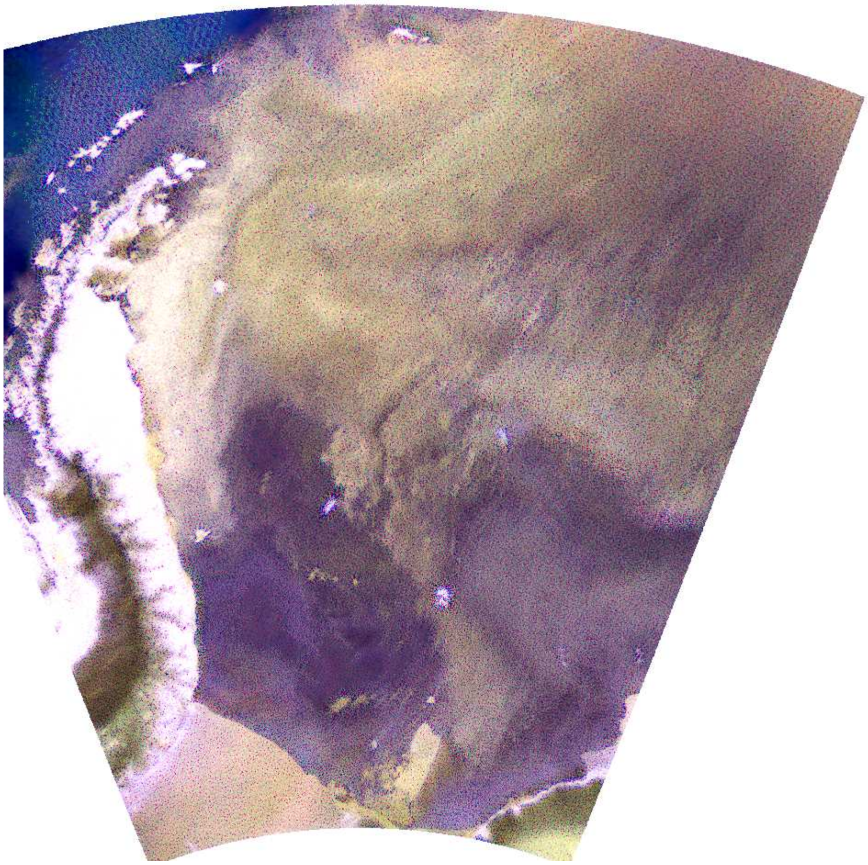

Figure 4.5: False color MAP reconstructed σ^0 image from SeaWinds and ASCAT over the Weddell Sea in Antarctica using four days worth of data (JD 201-214) in 2008. Red corresponds to the SeaWinds h-pol image, green corresponds to the SeaWinds v-pol image, and blue corresponds to the ASCAT image.

a different σ^0 field, and these σ^0 fields are nonlinearly related to an underlying wind vector field. It is often of interest to estimate the underlying field from the aperture-filtered samples. Chapter 7 extends the scatterometer reconstruction approach applied here for image reconstruction to handle the nonlinearity of the geophysical model function. Such an approach allows reconstruction of the underlying wind field. A similar approach may be used to address the incidence angle normalization model for fan-beam scatterometers, which is also nonlinear (i.e., linear in dB). This would allow for the simultaneous estimation of the $\mathcal{A}$ and $\mathcal{B}$ images using the new MAP reconstruction approach.

Chapter 5

UHR Wind Processing

Ultra high resolution (UHR) wind vector field estimates can be inferred from reconstructed σ^0 images over the ocean as long as temporal resolution and azimuth diversity are preserved. This chapter considers point-wise wind vector estimation from reconstructed σ^0 images over the ocean. Although this approach has been implemented for several years for the SeaWinds scatterometer [45] [46] [47], many theoretical issues have not been addressed.

This chapter formalizes the UHR wind estimation theory. The implicit assumptions applied in UHR retrieval are precisely stated. The UHR sampling and noise models are presented. Modifications of the UHR procedure that help ameliorate noise and ambiguity selection issues are also introduced.

5.1 σ^0 Reconstruction for Wind Retrieval

The UHR approach to wind estimation attempts to account for the irregular overlap and the irregular shape of the aperture functions by first reconstructing the σ^0 fields for different ‘flavors’ of measurements from a single scatterometer pass. The different flavors are then combined to estimate the wind point-wise.

In order to preserve azimuth diversity and temporal resolution, only σ^0 measurements from a given look and pass are combined in reconstruction intended for wind retrieval. This produces multiple reconstructed σ^0 images for a given pass, having different look geometries. Currently, UHR wind processing is only implemented for SeaWinds, but it could be extended to other scatterometers. The SeaWinds UHR wind product is reported on a 2.5km grid so that it can be easily compared to the standard 25km product. For SeaWinds, four flavors or looks are reconstructed (i.e., fore and aft, v-pol and h-pol).

In reconstruction for wind retrieval, the σ^0 fields are much more under-sampled than for other imaging applications because fewer slice measurements go into reconstructing the σ^0 images of a given flavor. Although SIR processing or MAP reconstruction may be applied to reconstruct the σ^0 fields for wind retrieval, the single-pass resolution is not enhanced much more than using the AVE algorithm and the noise is greatly amplified. The AVE algorithm is also more computationally efficient than other reconstruction methods. Furthermore, AVE is a linear reconstruction approach. Thus, AVE reconstruction has been adopted for SeaWinds UHR processing.

5.2 UHR Sampling Model

The UHR method assumes that the different measurements of a given flavor (i.e., the same polarization and frequency, and similar observation geometry) sample the same σ^0 field. This assumption results in a sampling operation similar to Eq. 3.2 for each flavor f

$$\vec{\sigma_f^0} = \begin{bmatrix} \int A_1(x)\sigma_f^0(x)dx \\ \vdots \\ \int A_{N_f}(x)\sigma_f^0(x)dx \end{bmatrix} = \mathcal{A}_f \sigma_f^0(x) \tag{5.1}$$

where x is a two-dimensional spatial variable, N_f is the number of measurements of flavor f, the $A_{n_f}(x)$'s are the aperture functions of the different σ^0 measurements, $\sigma_f^0(x)$ is the σ^0 field that is sampled by the different measurements, and $\mathcal{A}_f$ is a linear operator. The measurements of different flavors can be stacked into a vector producing

$$\vec{\sigma^0} = \begin{bmatrix} \mathcal{A}_{f_1}\sigma_{f_1}^0(x) \\ \vdots \\ \mathcal{A}_{f_M}\sigma_{f_M}^0(x) \end{bmatrix} = \mathcal{A}\vec{\sigma}^0(x). \tag{5.2}$$

In practice, the sampling operator is made discrete, the σ^0 images for each flavor are reconstructed separately, and the wind is estimated point-wise over each UHR wind vector cell (WVC). Solving the discrete problem in this manner is equivalent to assuming that the wind is piece-wise constant over each UHR WVC. The discrete version of the sampling operation can be expressed as

$$\vec{\sigma^0} = \begin{bmatrix} \vec{\sigma}^0_{f_1} \\ \vdots \\ \vec{\sigma}^0_{f_M} \end{bmatrix} = \begin{bmatrix} \mathbf{A}_{f_1}\sigma^0_{f_1}[x] \\ \vdots \\ \mathbf{A}_{f_M}\sigma^0_{f_M}[x] \end{bmatrix} = \mathbf{A}\vec{\sigma}^0[x] \tag{5.3}$$

where $\vec{\sigma}^0_{f_i} = \mathbf{A}_{f_i}\sigma^0_{f_i}[x]$ is a vector of slice measurements of a flavor f_i. The j^{th} component of $\vec{\sigma}^0_{f_i}$ is $\sum_x A_j[x]\sigma^0_j[x]$. The AVE reconstructed σ^0 field for flavor f_i can be expressed as

$$\sigma^0_{AVE,f_i}[x] = \tilde{\mathbf{A}}^T_{f_i}\sigma^0_{f_i} = \sum_{j\epsilon f_i}\tilde{A}_j[x]\sigma^0_j \tag{5.4}$$

where $\tilde{A}_j[x]$ is the slice response function of a particular slice j of flavor f_i normalized so that it sums to unity (i.e., $\sum_x \tilde{A}_j[x] = 1$ for all $j\epsilon f_i$). The collection (i.e., vector) of reconstructed σ^0 fields can be written as $\vec{\sigma}^0_{AVE}[x] = \tilde{\mathbf{A}}^T\vec{\sigma}^0$. Since each σ^0 field is reconstructed separately, we express $\sigma^0_{AVE,f_i}[x]$ simply as $\sigma^0_{AVE}[x]$ to simplify the notation in the rest of the chapter.

5.3 Noise Model

The noise model used in the UHR processing is simplistic. Each pixel of the reconstructed σ^0 fields is considered to be an independent realization of a random variable. The mean of the distribution at each point is assumed to be the true σ^0 value (i.e., the wind field projected trough the GMF). The variance of the distribution of each pixel is obtained using the standard method for composite measurements [47]. The standard approach for composite measurements is appropriate for drop-in-the-bucket methods, where each measurement is dropped into only one bin. However, when using a reconstruction approach, information from the same measurement modifies the reconstructed σ^0 value for many UHR WVCs. The noise model for the variance is more complicated than previously assumed. This subsection explores the relationship of between the noise model assumed for UHR wind retrieval and the standard noise model (i.e., where the slice σ^0 measurements represent independent realizations of random variables).

The noise model for the AVE images can be derived from the standard noise model as a linear combination of the slice measurement random variables. The slice measurements are represented as Gaussian random variables where the variance is a quadratic function of the mean as described in Chapter 2.

Since the slice measurements are Gaussian random variables, the AVE images are Gaussian random vectors. Also, because each slice measurement is assumed to be statistically independent and each slice contributes to only one of the AVE images, each AVE image is independent from each other. The mean and covariance of the AVE images completely characterize the UHR noise distribution. The mean of the pixel x_j of an AVE image of a given flavor can be calculated as

$$E\sigma^0_{AVE}[x_j] = \sum_i \tilde{A}_i[x_j] E\sigma^0_i = \sum_i \tilde{A}_i[x_j]\sigma^0_{i,t} \tag{5.5}$$

where the sum over i is a sum over the slices of a given flavor. $\sigma^0_{i,t}$ is the true slice σ^0 value and is related to the wind field $\vec{U}[x]$ by

$$\sigma^0_{i,t} = \sum_x A_i[x]\mathrm{gmf}(\vec{U}[x], \theta_i[x], \psi_i[x], pol_i, f_i) \tag{5.6}$$

where $\theta_i[x]$, $\psi_i[x]$, pol_i, and f_i represent the incidence angle, azimuth angle, polarization, and frequency of a of the i^{th} slice measurement, respectively.

The covariance of pixel x with pixel y of a particular AVE image is

$$\begin{aligned}
C_{AVE}[x,y] &= E(\sigma^0_{AVE}[x] - E\sigma^0_{AVE}[x])(\sigma^0_{AVE}[y] - E\sigma^0_{AVE}[y]) \\
&= E\left(\sum_i \tilde{A}_i[x](\sigma^0_i - \sigma^0_{i,t})\right)\left(\sum_j \tilde{A}_j[y](\sigma^0_j - \sigma^0_{j,t})\right) \\
&= \sum_{i,j} \tilde{A}_i[x]\tilde{A}_j[y]E(\sigma^0_i - \sigma^0_{i,t})(\sigma^0_j - \sigma^0_{j,t}) \\
&= \sum_i \tilde{A}_i[x]\tilde{A}_i[y]E(\sigma^0_i - \sigma^0_{i,t})^2 = \sum_i \tilde{A}_i[x]\tilde{A}_i[y]\xi^2_i
\end{aligned} \tag{5.7}$$

where $\xi_i^2 = \alpha(\sigma^0_{i,t})^2 + \beta\sigma^0_{i,t} + \gamma$ is the variance of the i^{th} slice measurement. This expression describes the correlation among pixels in a single AVE image. As noted before, the different AVE images are statistically independent and thus uncorrelated.

Note that if the AVE operation is underdetermined (which is generally true if the sampling matrix is underdetermined), the covariance matrix is singular. Thus, there is a lower dimensional manifold over which the Gaussian probability density function (pdf) is defined and it's density function is zero over the rest of the subspace. That is, we can take the singular value decomposition (or eigen decomposition) of the covariance matrix $\mathbf{C}_{AVE} = [\mathbf{V}_1, \mathbf{V}_0]\text{diag}([\vec{\lambda}_1; \vec{0},])[\mathbf{V}_1, \mathbf{V}_0]^T$ and the singular vectors $\mathbf{V}_1$ corresponding to non-zero singular values $\vec{\lambda}_1$ span the linear subspace (i.e., manifold) over which the Gaussian pdf is defined. Note, that the parameters of the pdf are functions of the wind field $\vec{U}[\vec{x}]$. The pdf of the reconstructed σ^0 fields for a given wind field can be expressed as

$$f(\vec{\sigma}^0_{AVE}[x]|\vec{U}[\vec{x}]) = \begin{cases} \frac{\exp\{\frac{-1}{2}(\vec{\sigma}^0_{AVE} - E\vec{\sigma}^0_{AVE})^T \mathbf{C}^{\dagger}_{AVE}(\vec{\sigma}^0_{AVE} - E\vec{\sigma}^0_{AVE})\}}{(2\pi)^{N/2}\prod_{n=1}^{N}\lambda_n} & \text{if } \vec{\sigma}^0_{AVE} = \mathbf{V}_1\vec{p} \\ 0 & \text{otherwise} \end{cases} \tag{5.8}$$

for some $\vec{p}$, where N is the dimension of the manifold, and the components of $E\vec{\sigma}^0_{AVE}$ and $\vec{\lambda}_1$ are functions of the wind field $\vec{U}[x]$.

$f(\vec{\sigma}^0_{AVE}[x]|\vec{U}[\vec{x}])$ is the maximum likelihood function and can be used to estimate the wind field from the AVE images. Since each pixel is potentially correlated with other pixels in the AVE images, the Fisher information matrix is generally not diagonal, suggesting that the wind at every pixel must be estimated simultaneously. Furthermore, the Fisher information matrix may be singular meaning that the wind field at the higher resolution cannot be estimated from the data alone. For these reasons, it may be more straight-forward to estimate the wind field directly from the slice measurements, applying a prior to regularize the problem, instead of first reconstructing the σ^0 measurements. This is investigated in more detail in Chapter 7.

5.3.1 UHR Point-wise Noise Model

Historically, the UHR wind estimation problem has been simplified by modifying the maximum-likelihood function and assuming that the covariance is diagonal.This regularizes the problem and makes it possible to estimate the wind vector at each pixel independently (i.e., point-wise estimation).

The forward projection is also modified so that each pixel of the AVE image is assumed to represent the projection of the wind field directly through the GMF

$$E\sigma^0_{AVE}[x] \approx \mathrm{gmf}(\vec{U}[x], \theta[x], \psi[x], pol, f) \tag{5.9}$$

instead of mapping through the sampling operator and the AVE reconstruction operator

$$E\sigma^0_{AVE}[x] = \sum_i \tilde{A}_i[x]\sigma^0_{i,t} = \sum_i \tilde{A}_i[x] \sum_y A_i[y]\mathrm{gmf}(\vec{U}[y], \theta_i[y], \psi_i[y], pol_i, f_i). \tag{5.10}$$

That is, AVE reconstruction is assumed to be an exact inverse of the sampling operation. Note that, pol and f are the polarization and frequency of the slices that are used to produce a particular AVE image. The azimuth and incidence angles for pixel x of a particular AVE image are approximated as

$$\psi[x] = \textstyle\sum_i A_i[x]\psi_i[x] \tag{5.11}$$

$$\text{and } \theta[x] = \textstyle\sum_i A_i[x]\theta_i[x] \tag{5.12}$$

respectively. For SeaWinds the look geometry approximation is appropriate because the change in the GMF with respect to the change in geometry over the slices that significantly contribute to a given pixel is relatively small.

The ML objective function for the modified UHR noise and measurement model is

$$\begin{aligned} f(\vec{\sigma}^0_{AVE}[x]|\vec{U}[x]) &= \frac{1}{(2\pi)^{M/2}|\tilde{\mathbf{C}}_{AVE}|^M} \exp\left\{\frac{-1}{2}(\vec{\sigma}^0_{AVE} - E\vec{\sigma}^0_{AVE})^T \tilde{\mathbf{C}}^{\dagger}_{AVE}(\vec{\sigma}^0_{AVE} - E\vec{\sigma}^0_{AVE})\right\} \\ &= \prod_x \frac{1}{(2\pi)^2 \prod_l \xi_l^2[x]} \exp\left\{\sum_l \frac{-(\sigma^0_{AVE,l}[x] - E\sigma^0_{AVE,l}[x])^2}{2\xi_l^2[x]}\right\} \end{aligned} \tag{5.13}$$

where l indexes the different AVE images, and $\tilde{\mathbf{C}}_{AVE,l}$ is a diagonal matrix with $\xi_l^2[x]$ as the x^{th} diagonal element. Since the covariance of the Gaussian distribution is diagonal (by the UHR assumption), each pixel of each AVE image can be expressed as an independent random variable. This causes the Fisher information matrix to also be diagonal and so the wind vector at each pixel may be estimated separately. The UHR point-wise likelihood function is

$$f(\vec{\sigma}^0_{AVE}[x]|\vec{U}[x]) = \frac{1}{(2\pi)^2 \prod_l \xi_l^2[x]} \exp\left\{ \sum_l \frac{-(\sigma^0_{AVE,l}[x] - E\sigma^0_{AVE,l}[x])^2}{2\xi_l^2[x]} \right\}. \tag{5.14}$$

5.4 Wind Vector Field Estimation

The modifications to the noise and measurement model made in the previous section greatly simplify the problem and make point-wise wind estimation possible. Although the UHR modifications effectively change the problem, in practice UHR point-wise estimation has been proven to produce useful results. Here, we investigate the point-wise estimation problem assuming the simplified UHR noise and measurement models. The conventional point-wise ML estimation approach is presented and some other approaches that ameliorate noise issues and improve ambiguity selection are introduced.

5.4.1 Point-wise ML Estimation

The standard approach to UHR retrieval is to separately estimate a wind vector for each pixel of the AVE images with a maximum-likelihood (ML) estimator. This is similar to the approach taken in conventional processing. However, UHR wind retrievals are much noisier and may be more biased than standard resolution products because there are fewer different AVE images (four for SeaWinds) than egg measurements (i.e., composite slice measurements) that fall into a standard resolution WVC and because the variance values are typically higher for the reconstructed σ^0's than for egg σ^0 measurements. Also, with the higher noise level, the skill (or percentage of highest ranked ambiguities that are the closest ambiguity to the true wind vector) is significantly degraded compared to the standard resolution product. The current UHR implementation selects the closest ambiguity to the standard resolution product then median filters the result [48]. The next two subsections discuss methods to ameliorate noise and ambiguity selection issues involved with UHR wind estimation.

5.4.2 Prefiltering σ^0

One method to reduce the effect of noise is to filter the AVE images before retrieving the wind. This is useful for reducing the noise level and improving the skill. However, this also reduces the spatial resolution and can introduce undesirable artifacts. Since the azimuth angle varies throughout the AVE images, low-pass filtering the AVE images may confound the look geometry for each pixel, especially in the swath edges and nadir regions for SeaWinds. Appendix D explores σ^0 filtering in more detail as well as presents a method to improve ambiguity selection without using external sources for UHR wind data.

5.4.3 MAP Estimation

Another method that reduces the variability of the estimates and that improves ambiguity selection is to impose a prior distribution using a MAP estimator. The MAP estimator for point-wise wind estimation of the vector at pixel x_i is

$$\hat{\vec{U}}_{MAP}[x_i] \quad = \quad \underset{\vec{U}[x_i]}{\operatorname{argmax}}\{f(\vec{\sigma}^0_{AVE}[x_i]|\vec{U}[x_i])f(\vec{U}[x_i])\} \tag{5.15}$$

where $\vec{\sigma}^0_{AVE}[x_i]$ is the vector of AVE σ^0 values at pixel x_i from all the different flavors, and $f(\vec{U}[x_i])$ is a prior of the wind vector. Note that the log of the objective function, $\log f(\vec{\sigma}^0_{AVE}[x_i]|\vec{U}[x_i]) + \log f(\vec{U}[x_i])$, is used in practice.

Figure 5.1 shows a ML log-likelihood function for wind retrieval as a function of wind speed and direction, the log of a Gaussian prior in speed and direction, and the corresponding MAP log-likelihood function. The ML log-likelihood function has several local maxima with similar values. These different modes correspond to wind vector ambiguities. The prior causes one of the modes to become the dominant mode in the MAP log-likelihood function. In this case, ambiguity selection becomes trivial and consists of choosing the ambiguity with the highest MAP log-likelihood value. It is apparent that an appropriate prior be used for each pixel (i.e., a prior whose mean changes smoothly over the pixels) otherwise an inconsistent wind field may result.

The MAP method is most useful for ameliorating ambiguity selection if the prior exhibits some spatial structure. For example, suppose that we have a prior distribution for

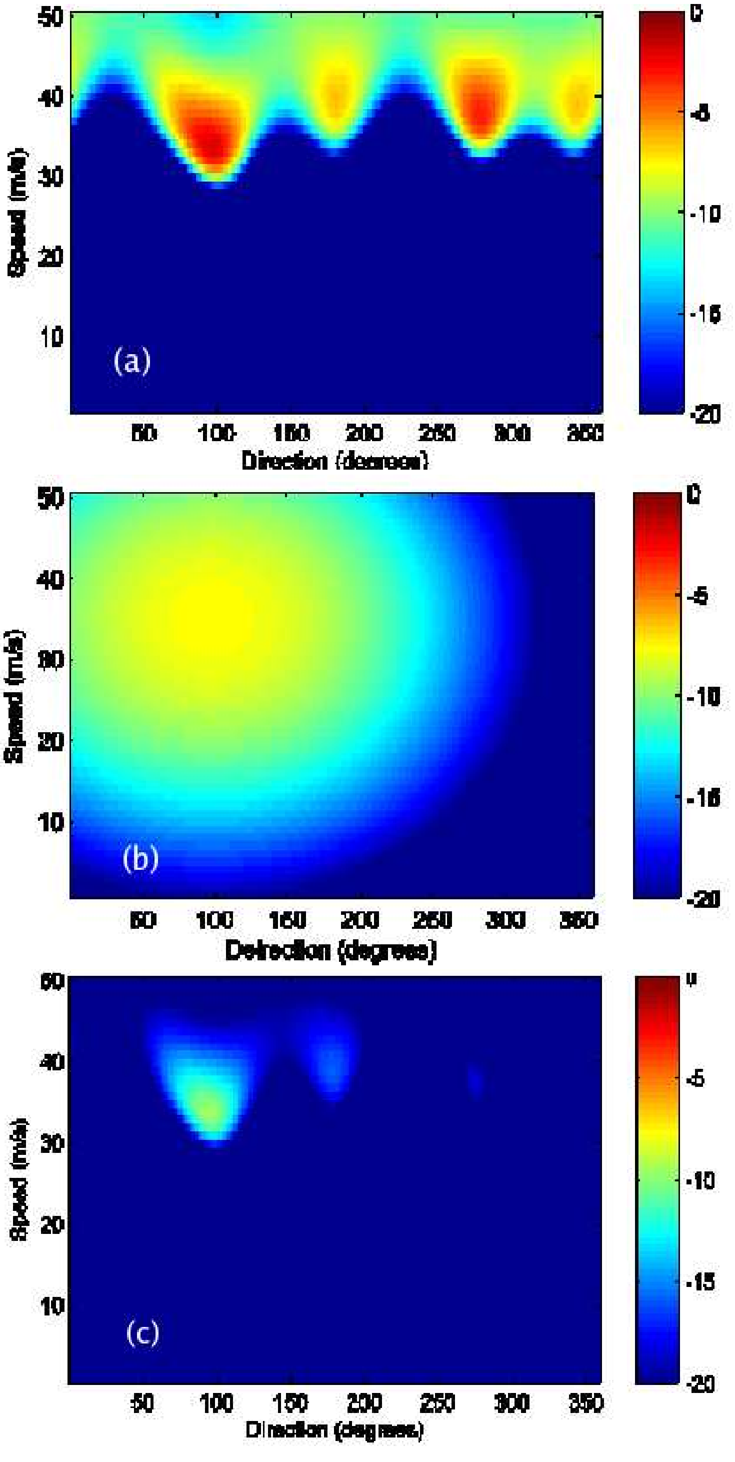

Figure 5.1: Images of the log of the point-wise (a) maximum-likelihood objective function, (b) prior distribution, and (c) MAP objective function, as a function of wind speed and direction for a particular observation geometry and synthetic wind vector.

each pixel x where the means among adjacent pixels are related by a wind field model. We could estimate the model parameters from the data and then impose the model fit as the mean of the prior. This helps create a smooth wind field while allowing the estimates to diverge from being forced to be in the space spanned by the wind field model. Alternatively, we may estimate the wind field and the model parameters simultaneously using a field-wise MAP estimator. The UHR field-wise MAP estimator can be expressed as

$$\begin{aligned}\hat{\vec{U}}_{MAP}[x] &= \underset{\vec{U}[x]}{\operatorname{argmax}}\{f(\vec{\sigma}^0_{AVE}[x]|\vec{U}[x])f(\vec{U}[x])\} \\ &= \underset{\vec{U}[x]}{\operatorname{argmax}}\{f(\vec{U}[x])\prod_x f(\vec{\sigma}^0_{AVE}[x]|\vec{U}[x])\} \qquad (5.16)\end{aligned}$$

for a given field-wise prior $f(\vec{U}[x])$, and if the prior is a function of a field-wise model (i.e., $f(\vec{U}[x]|M(\vec{\alpha}))$ where $M(\vec{\alpha})$ is a wind field model with model parameters $\vec{\alpha}$), then

$$\{\hat{\vec{U}}_{MAP}[x], \hat{\vec{\alpha}}_{MAP}\} = \underset{\vec{U}[x],\vec{\alpha}}{\operatorname{argmax}}\{f(\vec{U}[x]|M(\vec{\alpha}))\prod_x f(\vec{\sigma}^0_{AVE}[x]|\vec{U}[x])\}. \qquad (5.17)$$

UHR field-wise MAP estimation using a model-based prior is investigated for hurricane wind and rain estimation from SeaWinds in Chapter 6.

5.5 Conclusion

This chapter formalizes the UHR wind estimation theory. The sampling model is presented and the implicit assumptions are explicitly stated. The noise model for the reconstructed σ^0 fields is derived from the standard scatterometer noise model. The simplified UHR noise model is stated along with the implicit assumptions. Alternate wind estimation approaches that deal with noise and ambiguity selection issues are also introduced, although more detailed explanations of the σ^0 filtering and UHR MAP estimation methods are provided in Appendix D and Chapter 6.

Chapter 6

Hurricane Wind and Rain Estimation from SeaWinds at Ultra High Resolution

This chapter considers the UHR MAP estimation approach introduced in chapter 5 as applied to hurricane wind and rain field estimation. The material in this chapter is the subject of a published journal article [1] and two conference papers [5] and [6].

6.1 Introduction

Direct measurements of wind and rain are difficult to obtain in the extreme conditions of hurricanes. Buoys are often damaged in these intense storms and ships avoid them. Aircraft radar and dropsonde measurements in hurricanes provide important information, but this data is limited in spatial coverage.

Space-borne scatterometers have swaths that cover large regions over short time durations and provides invaluable data of large scale global weather. However, the relatively coarse resolution (typically 50km or 25km) of standard scatterometer wind products limits their use in resolving small scale features. While tropical cyclones are apparent in standard resolution products, important storm parameters such as the eye center location are not well resolved.

In ultra high resolution (UHR) surface wind data, much of the storm structure of hurricanes is obvious. However, there remain several issues that limit the use of scatterometers in observing tropical cyclones. Due to the resolution enhancement procedure, the UHR products are inherently noisier than their lower resolution counterparts [45]. Tropical cyclones are also associated with heavy rain which contaminates the wind estimates at both C-band and Ku-band (the conventional frequencies of space-borne systems) [49] [50] [51] [52]. Furthermore, the relationship between hurricane force winds and radar backscatter may not be modeled well by current geophysical model functions (GMF), though research is being done to improve the model function for extreme winds [53]. Moreover, the GMFs used for the UHR retrievals (QSCAT-1/F13 sometimes termed QMOD3 used by JPL in standard products for SeaWinds and CMOD5 for C-band instruments) are derived for the lower resolution products [8] [26]. In principle, the GMF should be independent of the resolution. However, since the GMFs are derived from low resolution data, using them for UHR winds may produce somewhat biased results–especially at very low wind speeds [54] [55].

This chapter applies the MAP estimation approach for ultra high resolution wind field estimation described in Section 5.4.3 to tropical cyclones using data from the SeaWinds scatterometer. The focus is primarily to present a new method to improve direction estimates and to reduce the variability of the vector estimates (speed and direction) while preserving mesoscale detail. A simple low-order hurricane wind field model is developed to provide prior information for maximum aposteriori (MAP) estimation of the wind. Using the hurricane model ameliorates the effects of rain and noise. The new method provides improved ambiguity selection, alternate wind estimates (MAP ambiguities), and estimates of important hurricane parameters. Simulation is employed to explore the effects of rain on the new method. The accuracy of the hurricane model parameter estimates is analyzed using the best track hurricane eye locations provided by the National Hurricane Center (NHC) and interpolated numerical weather prediction winds provided by the National Centers for Environmental Prediction (NCEP). The quality of the wind field estimates are analyzed using H*Winds made available by NOAA's hurricane research division [56]. Since σ^0 measurements are influenced by rain rate, the approach is extended to simultaneously estimate the wind and rain fields in hurricanes.

The chapter is organized as follows: Section 6.2 reviews pertinent principles of scatterometry and the high resolution wind products derived form SeaWinds. Section 6.3 outlines the new MAP wind estimation procedure for hurricanes. Section 6.4 develops the hurricane wind field model appropriate for scatterometry. Section 6.5 describes a simplification of the new method that allows for near real time implementation. Section 6.6 analyzes the quality of the results. Section 6.7 extends the method to simultaneous wind and rain estimation in hurricanes. Section 6.8 concludes.

6.2 Background

In tropical cyclones, the ultra high resolution product can resolve structure that is not apparent in the 25 km product. The eye center location, rain bands, and mesoscale convective events are resolved in the high resolution wind speed field. The resolution of the direction field, however, is limited by the nudging field in conventional ambiguity selection. High resolution ambiguity selection is problematic because the numerical weather prediction (NWP) winds used in ambiguity selection poorly represent small scale features. Ambiguity selection is further complicated by rain contamination and increased noise level. Low resolution nudging fields tend to produce UHR estimates with the hurricane eye center mislocated.

6.3 MAP Estimation for Tropical Cyclones

The wind estimation method presented here takes a novel approach. A low-order hurricane model is developed and is used as the mean of a field-wise prior distribution of the wind. This prior is used to augment the maximum likelihood objective function–producing MAP ambiguities and a field-wise MAP estimate of the wind. In the sequel we also develop a method based on MAP estimation to improve ambiguity selection of the point-wise ML ambiguities.

This section explains the theory behind the MAP estimation method. First, an overview of point-wise ML estimation and MAP estimation is provided. Then, field-wise MAP estimation using the hurricane model is developed. Next, the new method is contrasted with the conventional model-based approach and the conventional point-wise approach. Finally, a discussion of how to obtain prior distributions is presented.

6.3.1 Point-wise ML Estimation

For conventional UHR processing, ML estimation is employed to retrieve a wind vector for each pixel of the reconstructed σ^0 fields. This approach finds the wind vector $\vec{U}[x_j]$ at each pixel x_j that maximizes the probability density function (pdf) of obtaining the reconstructed σ^0 $\vec{\sigma}^0_{AVE}[x_j]$ at pixel x_j given the wind vector. This pdf or likelihood function for pixel x_j can be expressed as $f(\vec{\sigma}^0_{AVE}[x_j]|\vec{U}[x_j])$. Note that when estimating the wind and rain simultaneously from the σ^0 data, $\vec{U}[x_j]$ is a wind/rain vector. To be explicit and to simplify the notation, we express the wind vector speed and direction components explicitly as S and D when considering wind-only estimation in this chapter. We also simplify $\vec{\sigma}^0_{AVE}[x_j]$ as $\vec{\sigma}^0$, dropping the pixel index x_j because it can be implied by context. The likelihood function is then expressed as$f(\vec{\sigma}^0|S, D)$.

6.3.2 Point-wise MAP Estimation

In contrast to conventional point-wise ML wind estimation which finds the wind vector that maximizes the probability of σ^0 given the wind speed and direction, $f(\vec{\sigma}^0|S, D)$, point-wise MAP estimation maximizes the probability of the vector wind given the reconstructed σ^0 measurements, $f(S, D|\vec{\sigma}^0)$. This probability distribution can be found using Bayes' rule

$$f(S, D|\vec{\sigma}^0) = \frac{f(\vec{\sigma}^0, S, D)}{f(\vec{\sigma}^0)} = \frac{f(\vec{\sigma}^0|S, D)f(S, D)}{f(\vec{\sigma}^0)} \tag{6.1}$$

where the probability distribution $f(S, D)$ is the prior distribution of the wind. The MAP objective function, $f(S, D|\vec{\sigma}^0)$, is essentially a weighted version of the ML objective function, $f(\vec{\sigma}^0|S, D)$. Given the multiple σ^0 measurements, the wind speed and direction that maximize $f(S, D|\vec{\sigma}^0)$ can be found.

The point-wise ML objective function represents a joint distribution of independent Gaussian random variables and has the form [57]

$$f(\vec{\sigma}^0|S, D) = \prod_i \frac{1}{\sqrt{2\pi}\xi_i} e^{-\frac{(\sigma_i^0 - \mathrm{gmf}_i(S,D))^2}{2\xi_i^2}} \tag{6.2}$$

where σ_i^0 represents the i^{th} reconstructed σ^0 measurement, $\mathrm{gmf}_i(S, D)$ represents the σ^0 value resulting from projecting the given wind vector through the GMF with the same measurement geometry as the i^{th} measurement, and ξ_i^2 is the variance that is a function of the measurement noise and the modeling uncertainty of the GMF. Therefore, if the point-wise prior distribution is known the point-wise MAP estimate can be found by scaling the ML objective function by $f(S, D)$ and searching for the maxima. Note that $f(\sigma^0)$ represents the probability distribution of σ^0 and is not a function of the S and D which are to be estimated. Thus, it can be factored out of the maximization. This produces the point-wise wind vector estimate:

$$\{\hat{S}, \hat{D}\} = \underset{S,D}{\operatorname{argmax}}\{f(\vec{\sigma}^0|S,D)f(S,D)/f(\vec{\sigma}^0)\} = \underset{S,D}{\operatorname{argmax}}\{f(\vec{\sigma}^0|S,D)f(S,D)\} \tag{6.3}$$

which is the same expression as Eq. 5.15 in Section 5.4.3, but with the more explicit notation.

6.3.3 Field-wise MAP Estimation

For field-wise estimation the entire wind speed field, $\vec{S}$ (i.e., $S[x]$), and direction field, $\vec{D}$ (i.e., $D[x]$) are estimated. The field-wise prior distribution $f(\vec{S}, \vec{D})$ is given by the hurricane model. For each resolution cell, the speed and direction are assumed to be independent Gaussian random variables with means given by the model and some variance. Using this construction the prior distribution for one cell has the form

$$f(S,D) = f(S)f(D) = \frac{1}{\sqrt{2\pi}\xi_S} e^{-\frac{(S-\mathcal{S})^2}{2\xi_S^2}} \frac{1}{\sqrt{2\pi}\xi_D} e^{-\frac{(D-\mathcal{D})^2}{2\xi_D^2}} \tag{6.4}$$

where $\mathcal{S}$ and $\mathcal{D}$ are the speed and direction of the hurricane model wind for the resolution cell of interest. This construction provides prior distributions for each resolution cell.

The notion of correlation between adjacent cells is captured by the similarity of the means of the prior distributions rather than imposing correlation between the distributions (i.e. the distributions are statistically independent although the means of the distributions are linked by the field-wise model). This allows for small scale variability and preservation of high frequency information, although this may preserve high frequency noise as well. Assuming correlation between adjacent cells imposes additional structure on the estimated wind field. Since we desire estimates that are based primarily on the measurements and only moderately impacted by the model (since the model is simplistic), assuming independence between adjacent cells is appropriate for this application. Nevertheless, a more sophisticated model allowing correlation between adjacent cells may produce a more accurate result.

Independence between the distributions of adjacent resolution cells causes the field-wise prior to be equal to the product of the point-wise priors, $f(\vec{S}, \vec{D}) = \prod_{m,n} f(S,D)$. Note that we use the notation m, n instead of x to emphasize that the spatial index is two-dimensional (i.e., m and n index the rows and columns respectively of the wind field and σ^0 images). Assuming that each resolution cell is independent from each other also enables the field-wise ML objective function to be written as the product of the point-wise objective functions. Thus, the field-wise MAP objective function has the form

$$\begin{aligned} f(\vec{S},\vec{D}|\vec{\sigma}^0) &= \frac{1}{f(\vec{\sigma}^0)} f(\vec{\sigma}^0|\vec{S},\vec{D}) f(\vec{S},\vec{D}) = \frac{1}{f(\vec{\sigma}^0)} \prod_{m,n} \left\{ f(S) f(D) \prod_i f(\sigma_i^0|S,D) \right\} \\ &= \frac{1}{f(\vec{\sigma}^0)} \prod_{m,n} \left\{ \frac{1}{2\pi\xi_S\xi_D} e^{\frac{-(S-\mathcal{S}(\vec{\alpha}))^2}{2\xi_S^2}} e^{\frac{-(D-\mathcal{D}(\vec{\alpha}))^2}{2\xi_D^2}} \prod_i \frac{1}{\sqrt{2\pi}\xi_i} e^{-\frac{(\sigma_i^0-\text{gmf}_i)^2}{2\xi_i^2}} \right\} \end{aligned} \tag{6.5}$$

where $\vec{\sigma}^0$, $\vec{S}$, and $\vec{D}$ represent the σ^0 fields, the wind speed field, and the wind direction field of the study region, respectively. σ_i^0, S, and D represent the i^{th} σ^0 measurement, the wind speed, and the wind direction all for a particular resolution cell at index (m,n) of the fields. Also, $\mathcal{S}(\vec{\alpha})$ and $\mathcal{D}(\vec{\alpha})$ represent the hurricane model speed and direction for a cell at index (m,n) where $\vec{\alpha}$ represents a vector of hurricane model parameters.

Note that Equation 6.5 states that the field-wise MAP objective function is a scaled product of the point-wise objective functions of each cell in the field-wise grid. Likewise, it can be shown that with this construction the field-wise MAP value is a scaled product of the point-wise MAP values for a particular model instance,

$$\begin{aligned} MAP_{fw} &= \max_{\vec{S},\vec{D}} f(\vec{S},\vec{D}|\vec{\sigma}^0) = \max_{\vec{S},\vec{D}} \frac{1}{f(\vec{\sigma}^0)} \prod_{m,n} \left\{ f(S) f(D) \prod_i f(\sigma_i^0|S,D) \right\} \\ &= \frac{1}{f(\vec{\sigma}^0)} \prod_{m,n} \max_{S,D} \left\{ f(S) f(D) \prod_i f(\sigma_i^0|S,D) \right\} = \frac{1}{f(\vec{\sigma}^0)} \prod_{m,n} MAP_{pw}. \end{aligned} \tag{6.6}$$

The best model instance is the one that maximizes the field-wise MAP value. Thus, the field-wise MAP value becomes the hurricane model objective function l,

$$l = \max_{\vec{\alpha}} \left\{ MAP_{fw}(\vec{\alpha}) \right\}. \tag{6.7}$$

For practical implementation, the log of the field-wise objective function is maximized. Taking the log of Equation 6.5, leaving out constant terms, and then maximizing over wind fields and hurricane model parameters produces

$$L = \max_{\vec{\alpha}} \left\{ \sum_{m,n} \max_{S,D} \left\{ \frac{-(S - \mathcal{S}(\vec{\alpha}))^2}{\xi_S^2} - \frac{(D - \mathcal{D}(\vec{\alpha}))^2}{\xi_D^2} - \sum_i \frac{(\sigma_i^0 - \mathrm{gmf}_i(S, D))^2}{\xi_i^2} \right\} \right\}. \quad (6.8)$$

The arguments S, D, and $\vec{\alpha}$ that maximize the log likelihood value L are the estimates of the wind speed and direction for each resolution cell and the hurricane model parameters. This method simultaneously estimates the hurricane model parameters and the wind field. Note that if we factor out a negative sign from the right side of Equation 6.8, the objective function must be searched for minima rather than maxima and we obtain an expression similar to the standard ML objective function. The expression in Equation 6.8 is similar to procedures frequently used in NWP data assimilation [58] [59]. However, the measurement term (the last term on the right) remains Gaussian in the σ_0 domain, which is consistent with standard ML wind retrieval schemes. We note that certain wind directions may be favored for certain measurement geometries by the ML objective function [60]. This may also be inherited by the MAP estimator described here.

6.3.4 Implications

The new approach diverges from conventional model-based methods. Here model-based implies using a field-wise model to describe the two-dimensional structure of the surface vector wind. Conventional model-based methods estimate only the parameters of the wind field model. These methods force the wind estimate to be in the space spanned by the model. Thus, the resulting wind fields contain only information captured by the model. For a practical low-order model, forcing the wind field estimate to be in the space spanned by the model restricts the wind field estimates to low resolution. The new MAP construction allows for the preservation of the information obtainable by a non-model-based approach (point-wise ML estimation), while emphasizing the structure described by the model.

The difference between point-wise ML estimation, model-based field-wise ML estimation, and the field-wise MAP estimation is illustrated by the following. All three of these methods can be formulated as a constrained optimization problem. For point-wise ML estimation the problem statement is:

for each cell at index (m, n),

maximize $\sum_i \frac{-(\sigma_i^0 - \mathrm{gmf}_i(S,D))^2}{\xi_i^2}$, or equivalently $f(\sigma^0|S, D)$,

subject to $S \geq 0$ and $0 < D \leq 360$.

This produces up to four possible wind ambiguities for each resolution cell due to local maxima in the objective function. Ignoring ambiguities (only considering the absolute maxima which corresponds to the first ambiguity) the point-wise objective functions can be summed up to form a field-wise objective function. The point-wise ML estimation problem statement for the entire field (field-wise ML estimation) can thus be written as

maximize $\sum_{m,n,i} \frac{-(\sigma_i^0 - \mathrm{gmf}_i(S(m,n),D(m,n)))^2}{\xi_i^2}$, or equivalently $f(\vec{\sigma}^0|\vec{S}, \vec{D})$,

subject to $S \geq 0$ and $0 < D \leq 360$

since both problem statements result in the same wind field. This can be interpreted as a field-wise objective function which is maximized when the point-wise objective function of each resolution element is maximized. Such a result allows comparisons of point-wise with field-wise techniques. For model-based ML estimation with the assumption that each resolution element is independent, the problem statement can be expressed as

maximize $\sum_{m,n,i} \frac{-(\sigma_i^0 - \mathrm{gmf}_i(S(m,n),D(m,n)))^2}{\xi_i^2}$, or equivalently $f(\vec{\sigma}^0|\vec{S}, \vec{D})$,

subject to $\vec{S} = \mathcal{S}(\vec{\alpha}), \vec{D} = \mathcal{D}(\vec{\alpha})$, where $S \epsilon \vec{S}$ and $D \epsilon \vec{D}$.

This is equivalent to estimating the model parameters $\vec{\alpha}$ and then generating the estimate of the wind field using the model. The field-wise ML estimation method and the model-based ML estimation method optimize the same metric but the model-based ML estimation method restricts the solution space more than the point-wise ML estimation method. The field-wise MAP estimation method searches the same solution space as the field-wise ML estimation method but optimizes an augmented metric. For field-wise MAP estimation the problem statement is:

maximize $\sum_{m,n,i} \left\{ \frac{-(S-\mathcal{S}(\vec{\alpha}))^2}{\xi_S^2} - \frac{(D-\mathcal{D}(\vec{\alpha}))^2}{\xi_D^2} - \frac{(\sigma_i^0 - \mathrm{gmf}_i(S(m,n),D(m,n)))^2}{\xi_i^2} \right\}$,

or equivalently $f(\vec{S}, \vec{D}|\vec{\sigma}^0)$,

subject to $S \geq 0$ and $0 < D \leq 360$.

The field-wise MAP estimation approach can be viewed as point-wise MAP estimation with priors given by a field-wise model. Remember that ξ_i characterizes the uncertainty of the i^{th} observation to the true σ^0. If the variance terms ξ_S and ξ_D are very large compared to the ξ_i's, the field-wise MAP objective function effectively becomes the field-wise ML objective function. Furthermore, if ξ_S and ξ_D are small compared to the ξ_i's, any solution that is not in the space spanned by the hurricane model produces a large and negative MAP value (in log space) and the field-wise MAP problem statement essentially becomes equivalent to the model-based ML estimation problem statement. Thus, the variance terms control how much the hurricane model is imposed. The relative values between ξ_S, ξ_D and ξ_i are a measure of the importance of the model speed error, the model direction error, and the actual measured σ^0 error respectively. ξ_i is a function of the measurement and the true wind, while ξ_S and ξ_D are linked to the hurricane model. Furthermore, ξ_S and ξ_D can be scaled relative to the ξ_i's in order to minimize the influence of the hurricane model while maintaining an acceptable noise level (variability of the estimates). Nominal values of ξ_S and ξ_D are found empirically in the sequel.

Imposing a prior on the wind has positive consequences as well as limitations. The new method ameliorates the cross-track pinning of the winds caused by rain and simplifies, or even eliminates, the issue of ambiguity removal. However, the priors modify the ML objective function so that the resulting estimates are no longer ‘pure’ measurements (they are combinations of measurements and a model). Nevertheless, the MAP estimation method imposes the hurricane model less severely than true model-based estimation.

6.3.5 Prior Distributions

It is important that the prior be appropriate for the situation. There are many schemes for obtaining appropriate prior distributions. For example, one may choose a non-informative prior (constant or uniform distribution), which causes the MAP estimation problem to reduce to maximum likelihood estimation. Alternatively, one may apply a maximum entropy prior subject to some constraint. Both the uniform prior and the maximum entropy prior are useful when it is desirable to minimize the amount of information that the prior imposes on the estimates. A more conventional approach is to apply an empirical prior. Empirical priors can be derived from wind/rain data from any source or sensor. Such priors may be global or specific to certain types of storms. In Section 6.4 a prior for winds in hurricanes is derived from several observations of tropical cyclones.

The question to be addressed is which prior is the best. According to convex Bayes theory, the set of prior distributions is a convex set. That is, if we have multiple viable priors, any convex combination of the priors is also a reasonable prior [61]. Thus, we may combine any two priors that are optimum according to two different criteria to obtain a new prior that represents a trade-off between the criteria. For example, we may combine an empirical prior with a uniform prior in order to reduce the influence that the prior has on the estimate. This approach is taken in Section 6.7 for the rain prior in hurricanes.

6.4 Empirical Hurricane Model

This section develops the empirical hurricane model that provides the prior distributions for the MAP estimation wind retrieval procedure. The model is not dynamic but is rather a simple ‘snapshot’ model of the horizontal structure of the near surface winds of hurricanes. First, the statistics of real storms are analyzed and empirical distributions are developed from high resolution SeaWinds wind data. Although these winds are rain contaminated and may contain ambiguity selection errors, we assume that these effects average out. Nevertheless, we recognize that there may still remain a bias in the estimates due to rain effects [62] [49]. We neglect this issue here so that the model is consistent with the standard GMF used in wind retrieval. Using scatterometer data to derive the model produces a model that is consistent with and appropriate for the scatterometer data.

Although the model developed is simplistic, the MAP estimation and MAP ambiguity selection procedures can be scaled to impose the model as weakly (or strongly) as desired. Thus, the benefits of imposing the large scale structure described by the model are obtained, while the small scale structure that is not described by the model is preserved.

We hypothesize that much of the asymmetrical structure of the storms can be described by a superposition of a mean wind flow (mean flow) through the region containing the storm [53]. This hypothesis is tested and verified by orienting the storms according to this mean flow and then generating new empirical distributions for the wind speed and direction. This asymmetry is then investigated further by binning the storms by size and by magnitude of the mean flow and generating empirical distributions for each type of storm. Finally, a model is developed based on the relationship between the size of the storm and the mean flow.

6.4.1 Empirical Distribution of Hurricane Winds

Empirical probability density functions (pdfs) for the priors are obtained using QuikSCAT-derived conventional UHR data of a large number (100) of observations of named storms in the North Atlantic Basin from 1999 to 2005. Normalized histograms (empirical pdfs) are generated by binning the wind speeds and directions as a function of distance from the eye (1 km per bin). The direction relative to the eye center (relative direction) is defined as the angle between the eye vector (the vector drawn from the eye center to the resolution cell of interest) and the wind vector in a clock-wise manner from the eye vector.

Note that in generating the empirical priors we include all UHR retrieved wind estimates with only minimal use of quality control. Quality control methods are important to ensure reliability of the hurricane model as well as the resulting estimates. As a quality control metric, high resolution simultaneous wind and rain retrieval may be used to throw out rain contaminated winds. Several low resolution quality control methods have proven effective for use in 25 km products [63] [64]. However, the effectiveness of using low resolution quality control for use with the UHR products as well as within hurricanes has yet to be explored. Furthermore, low resolution quality control methods tend to flag large portions of hurricanes as poor due to rain and uncertainty in the GMF. Discarding this data limits the amount of data needed to derive the prior distributions as well as fit the hurricane model in the wind retrieval step. Other limitations include the fact that the QMOD3 GMF tends to underestimate very high wind speeds. This produces a hurricane wind field model whose high wind speeds may also be underestimated. This issue may be corrected using bias correction techniques post wind retrieval or by improving the GMF. However, due to lack of truth data and since we are primarily concerned with improving direction estimates, neither bias correction nor GMF adjustment is employed.

Figure 6.1 illustrates the mean of the wind speed and direction relative to the eye center as a function of distance from the eye center. The mean of the direction distribution is about 250 degrees rather than 270, which produces vectors orthogonal to the vector drawn from the eye center to the resolution cell of interest. This is consistent with the known fact that there is a significant degree of convergence (negative divergence) in the near surface wind fields of hurricanes.

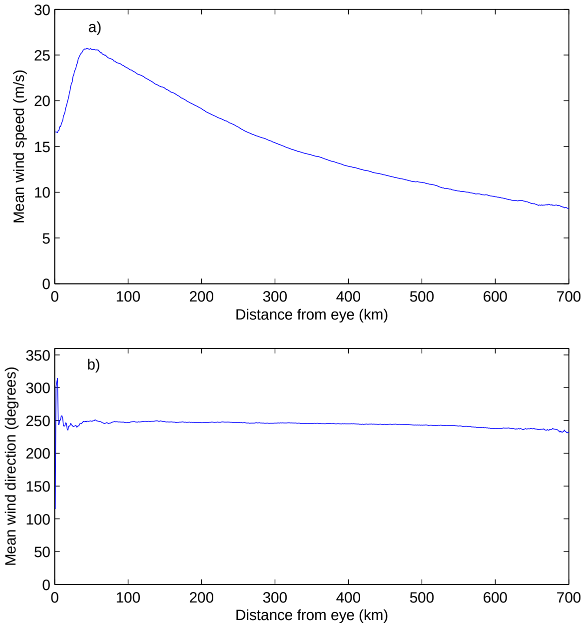

Figure 6.1: Means of the empirical speed and relative direction distributions as a function of distance from the hurricane eye. a) The mean of the wind speed distribution. b) The mean of the relative direction distribution.

Figure 6.2 depicts the standard deviations of the scatterometer wind speed and direction as a function of distance from the eye. The peak near the eye center of the standard deviation of the direction distribution is caused by several factors including rain contamination, ambiguity selection errors, artifacts of small scale features, and insufficient data for the statistics to converge. The higher standard deviation far from the eye can be attributed to lack of data and to other convective events outside the immediate vicinity of the hurricane center.

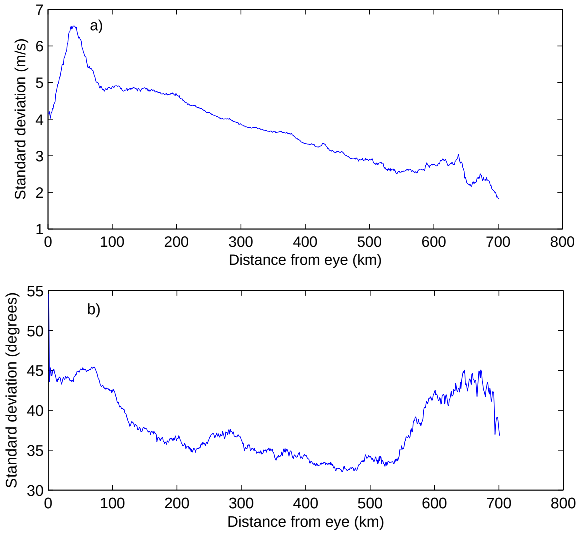

Figure 6.2: Standard deviations of the empirical speed and relative direction distributions as a function of distance from the hurricane eye. a) The standard deviation of the wind speed distribution. b) The standard deviation of the relative direction distribution.

Figure 6.3 illustrates a plot of the empirical distributions for the wind speed and direction for a particular distance from the eye (140 km) with a Gaussian fit superimposed. Although the direction distribution may have some significant higher order moments, both the wind speed and direction distributions are similar to the Gaussian distributions. This justifies the Gaussian approximation used in the development of the MAP estimation procedure in Section 6.3.

6.4.2 Investigating Asymmetry

The empirical distributions developed above describe the bulk structure of the storms as a function of distance from the eye. The asymmetrical structure of the storms is now investigated using an empirical approach.

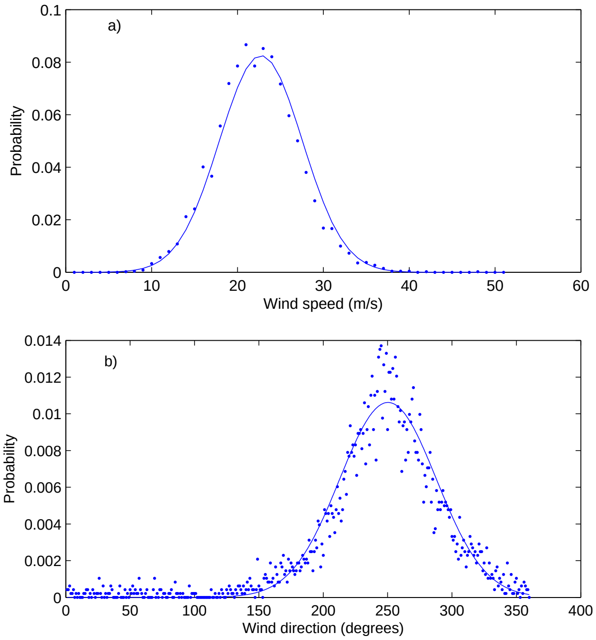

Figure 6.3: Wind speed and relative direction distributions for a particular distance from the eye center (140 km) with a Gaussian fit superimposed. a) The wind speed distribution. b) The relative wind direction distribution. Both distributions are similar to the Gaussian suggesting that a Gaussian approximation can be used.

The same 100 named storms are oriented so that the mean flow is pointed in the same direction. Then a histogram is generated where the wind is binned with respect to the angle from mean flow as well as the distance from the eye center. The mean flow is determined by the vector mean of the wind field (care is taken to include the same number of vectors on each side of the eye to suppress a bias in the mean).

Figure 6.4 shows the mean of the wind speed as a function of angle from the mean flow for several distances from the eye center. The curve shows the asymmetry due to the mean flow. The peak near the 90 degree bin shows that the right side of the storm, with respect to the direction of the mean flow, tends to have the highest wind speed. Figure 6.5 illustrates the standard deviation of the wind speed as a function of distance from the eye averaged over several angles from the mean flow. The solid line is the standard deviation in Figure 6.2 and the dashed line is the standard deviation averaged over the angles from the mean flow. The standard deviation is generally reduced when taking the mean flow into account. This implies that superposition of a mean wind flow can be used to describe general flow in a hurricane better than a pure axially symmetric field.

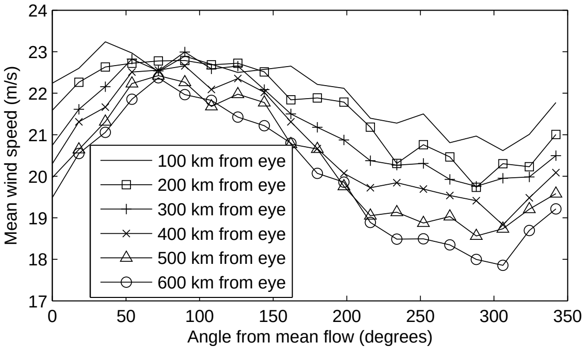

Figure 6.4: Mean of the wind speed distribution as a function of angle from mean flow for various distances from the hurricane eye. This pattern affirms that the right side of the storm (with respect to the mean flow) generally has a higher wind speed than the left side.

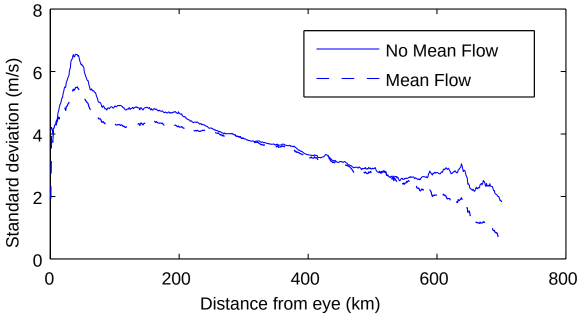

Figure 6.5: Standard deviation of the empirical wind speed distribution versus distance from the eye averaged over several angles from mean flow. The upper line is the standard deviation without taking the mean flow into account.

Further analysis is employed in order to investigate the relationship between the magnitude of the mean flow, the size, and the asymmetrical structure of a storm. Each storm is binned according to its size and the magnitude of the mean flow. Then the storms are oriented so that the direction of the mean flow is the same and speed and direction histograms are generated for each resolution cell on the new grid (oriented according to the eye center and mean flow). The size of the storm is determined by the root mean squared (RMS) value of the speed in a region including all cells within 150 km from the eye. The means and standard deviations of the wind speed and direction distributions are also calculated. The plots in Figure 6.6 illustrate slices of the mean wind speeds for large and small storms with various magnitudes of the mean flow. A storm is considered small (or large) if the RMS speed near the eye is less than or equal to 22 m/s (or greater than 22 m/s). Mean flow is categorized as low, medium, or high if the magnitude of the vector mean is less than or equal to 2.5 m/s, greater than 2.5 m/s and less than or equal to 5 m/s, or greater than 5 m/s respectively. The slices orthogonal to the mean flow are reported because they represent the most extreme asymmetry due to the mean flow. The large and small storms have similar speed profiles but the large storm speeds are scaled higher. Also, the left side of the storm (with respect to the mean flow) is generally less intense than the right side and the asymmetry is increased with higher magnitude of the mean flow.

6.4.3 Hurricane Model

Any of the empirical distributions described above can be used directly in the MAP wind retrieval process; however, this subsection develops a simple model that approximates the empirical distribution where the mean flow and storm size are taken into account. This allows interpolation between the coarsely binned sizes of storms and mean flows of the empirical distributions. A simplistic model with few parameters is developed to describe the large scale horizontal structure of the near surface winds of a hurricane as a function of the hurricane size and the mean flow (and eye center location). The model assumes that the hurricane wind field is composed of a symmetric cyclonic wind field with a superimposed mean wind flow.

To obtain the structure of the wind field a simple curve is fit to the speed profile in Figure 6.1. This simple curve ramps up linearly from about half of the maximum speed to the maximum speed, and then falls off exponentially to a mean offset. For simplicity, we assume a mean offset which is constant over all types of hurricanes. Using the curve in Figure 6.1 we choose a mean offset of 7 m/s (which is also approximately the mean wind speed over the ocean). Fitting this curve to the speed profile in Figure 6.1 provides nominal values for the radius of maximum wind speed of the eye and the decay rate of the exponential portion. The fit produces a radius of maximum wind speed of about 50 km and a spatial decay rate of about 475 km. A model realization is generated by producing a symmetric cyclonic wind field with the appropriate speed profile and direction field (250 degrees from eye vector) and superimposing a mean wind flow.

The plots in Figure 6.6 show slices of the speed fields of the hurricane model fits as well as the mean wind speeds for large and small storms with various magnitudes of the mean flow. The model fits the data well for low and medium wind flow, but for the high mean flow the model fit shows slightly more asymmetry than the data suggests. This is due to lack of high mean flow cases, which are more rare. For these cases, the rain contamination and ambiguity selection errors may not have been averaged out.

Table 6.1 shows the vector RMS differences between the means of the empirical speed and direction distributions and the model fit for large and small storms with various magnitudes of the mean flow for the same North Atlantic storms. As expected, the high mean flow case has larger RMS differences than the other two cases; however, all the cases have a relatively low RMS difference (less than 7.1 m/s) suggesting that the model fits the mean of the empirical distributions well. Thus, the model may be used to describe the storm structure with respect to its size and mean flow.

Table 6.1: Vector RMS differences between the mean of the empirical distributions and the model fit for large and small storms with various magnitudes of mean flow.

	Mean Flow		
	Low	Medium	High
Small Storms	3.05 m/s	2.97 m/s	5.31 m/s
Large Storms	4.39 m/s	5.00 m/s	7.07 m/s

With these results in mind, the means for the prior distributions for MAP estimation are derived from the simplified hurricane model fit to the data (in the sense of optimizing the

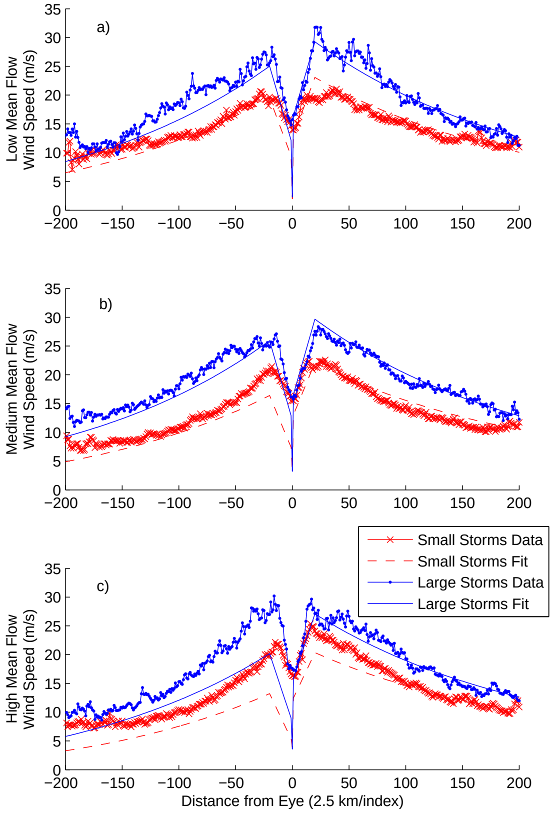

Figure 6.6: Slices of the mean of the empirical wind speed distributions orthogonal to the mean flow vector for large and small storms with various magnitudes of the mean flow. a) Low mean flow. b) Medium mean flow. c) High mean flow. The corresponding speed profiles from the simplified hurricane model are superimposed.

MAP objective function). This provides estimates of the eye center location (latitude and longitude), the magnitude and direction of the mean flow vector, and the maximum speed scale factor, which are parameters of the hurricane model. The variances of the priors are obtained from the general empirical distributions in Figure 6.2. We conservatively assume that the standard deviation of the speed and direction are constant at 7 (m/s) and 45 degrees respectively.

6.5 Implementation

Incorporating the prior described in Section 6.4 into the MAP estimation procedure requires searching a nonlinear objective function of several variables (the hurricane parameters as well as the wind speed and direction at each resolution cell). This is computationally taxing and can be a deterrent for using such a method in near real time processing. This section considers a simplification by constraining the solution space to that spanned by the point-wise ambiguities (MAP ambiguity selection). This reduces the search space considerably, as well as produces an estimate of the wind that is not biased by the model. This section also considers estimating the eye center from the speed field before performing MAP ambiguity selection, which reduces the search space even further.

MAP ambiguity selection is performed to reduce computation and to provide an improved ML estimate of the wind. MAP ambiguity selection is a form of weak nudging. Instead of forcing the ML ambiguity choice to be closest to the nudging field, MAP ambiguity selection allows for the likelihood value to dominate the speed and direction error–thus the ambiguity with the higher probability will be chosen more often than with conventional nudging. This new field-wise MAP ambiguity selection procedure begins with conventional high resolution point-wise estimation. The ambiguities are then chosen to maximize the log of the field-wise MAP objective function. Thus, Equation 6.8 becomes

$$L^* = \max_{\vec{\alpha}} \left\{ \sum_{m,n} \max_k \left\{ \frac{-(S_k - \mathcal{S}(\vec{\alpha}))^2}{\xi_S^2} - \frac{(D_k - \mathcal{D}(\vec{\alpha}))^2}{\xi_D^2} - \sum_i \frac{(\sigma_i^0 - \mathrm{gmf}_i(S_k, D_k))^2}{\xi_i^2} \right\} \right\} \quad (6.9)$$

where S_k and D_k are the speed and directions of the k^{th} point-wise ambiguity. This field-wise MAP ambiguity selection procedure produces estimates of the hurricane model parameters as well as choosing appropriate ambiguities. Field-wise MAP ambiguity removal is not MAP wind retrieval. Ambiguity selection cannot provide the same immunity to rain and noise that is possible with MAP wind retrieval. Nevertheless, MAP ambiguity selection is useful in two ways. First, it can provide an estimate of the wind that is not biased by the model. Second, performing field-wise MAP ambiguity selection provides estimates of the hurricane model parameters which can be used in MAP wind retrieval. Performing MAP estimation with these hurricane model parameters is more computationally efficient than simultaneously estimating the wind and the hurricane model parameters. Thus, field-wise MAP estimation (or wind retrieval) can also be done in near real time and the field-wise MAP ambiguity selection (of the ML ambiguities) is also provided.

Although MAP ambiguity selection reduces the search space significantly, the method remains computationally taxing. To simplify the problem further, a method for finding the eye center from the first ambiguity speed field before applying MAP ambiguity selection is developed. This method is based on the circular Hough transform (CHT). The CHT is used to find circles in a binary image (an image consisting of ones and zeros). If the radius R of the circle is known, the CHT is calculated simply by drawing a circle of radius R from each pixel that has a value of 1 in the binary image and accumulating the number of these circles that hit each pixel. Thus, the maximum value of the CHT is at the same index as the center point of the circle. For finding the hurricane eye, the speed field is converted to a binary image and then searched for a circle with a 50 km radius. Then, the CHT is weighted by the inverse of the speed field. This weighting is done to suppress circle centers in high wind speed regions and emphasize those in low wind speed regions (like the eye center). Finally, the index of the maximum of the weighted CHT is reported as the hurricane eye center. We note that when the eye is over land or outside the swath, the CHT method produces erroneous eye center estimates. We also note that there may be several local maxima in the weighted CHT. The other local maxima typically occur in heavy rain bands (since rain attenuation may cause the rain bands to appear as lower wind speeds), but since these are not typically circular the CHT value of the true eye tends to dominate.

6.6 Analysis

It is difficult to validate the MAP estimation method for hurricanes because truth data is limited–especially in spatial coverage. One indicator of the quality of the result is the accuracy of the estimates of the hurricane model parameters. Another is the accuracy of the estimated wind. In this section simulation is employed to explore the effect of rain on MAP estimation and MAP ambiguity selection. Also, the new eye center estimates are compared to the best track locations provided by the NHC. Interpolated NCEP winds are used to check the quality of the other estimated hurricane model parameters (the mean flow and maximum speed scale factor). Although, NCEP winds are limited in resolving fine scale hurricane structure, they may be used as an indicator of consistency of the estimated mean flow and maximum speed scale factor parameters. Finally, the H*Wind hurricane model winds provided by NOAA's hurricane research division [56] are used to check the quality and integrity of the estimated winds. The H*Wind products are smoothed over several hours and although they are reported with a grid spacing of about 5-6 km, the actual resolution is much more coarse than the UHR winds. Nevertheless, they portray the large scale structure of hurricanes well.

6.6.1 Simulation

Simulation is employed to analyze the effectiveness of the new approach. Synthetic σ^0 values are generated by projecting H*Wind wind fields and synthetic uniform rain rates through the simultaneous wind and rain model described by Draper [50] and adding Monte Carlo noise. The noise, ν, represents communication noise and fading, and is modeled by a zero-mean Gaussian random variable whose variance is a function of the σ^0 value as described in Chapter 2. Thus, $\nu \sim N\left(0, \sqrt{\alpha + \frac{\beta}{\sigma^0} + \frac{\gamma}{(\sigma^0)^2}}\right)$, where nominal values are used for α, β, and γ (i.e., $\alpha = 0.0025$, $\beta = 1.9 \times 10^{-4}$, and $\gamma = 1.2 \times 10^{-7}$) [8]. σ^0 fields are simulated for various rain rates and the error of the resulting wind fields is calculated. Ideal ambiguity selection (the conventional high resolution ambiguity closest to the H*Wind), MAP ambiguity selection, and MAP estimation are compared. For simulation the MAP ambiguity selection and MAP estimation eye centers are fixed to the true eye center.

Figure 6.7 shows the RMS error versus rain rate averaged over a few H*Wind fields used in simulation. On average the MAP estimation procedure reduces the RMS error lower than even ideal ambiguity selection (i.e., closest to the true), and thus does much better than the conventional ambiguity selection on real data. Also, MAP ambiguity selection approaches ideal ambiguity selection in the RMS error sense. These results suggest that for all rain rates the MAP estimation procedure is superior to the other methods and that the MAP ambiguity selection method is similar to ideal ambiguity selection and thus generally better than the conventional approach.

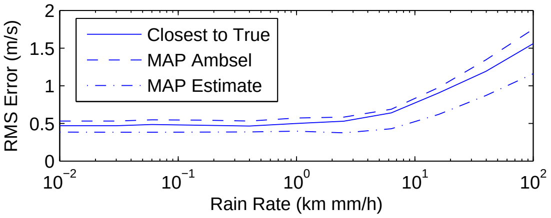

Figure 6.7: RMS error versus rain rate for ideal ambiguity selection, MAP ambiguity selection, and MAP estimation.

6.6.2 Quality of the Hurricane Model Parameters

This subsection analyzes the scatterometer derived hurricane model parameters: the eye center estimates, the maximum speed scale factor and the mean flow. The eye center results are compared with the best track locations (which are interpolated to the same time as the QuikSCAT measurements). First the MAP ambiguity selection eye center location, which is derived from the hurricane model fit, is evaluated. Next, the CHT eye finding method is analyzed. Then, the conventional high resolution method is explored with respect to the eye center parameter. Since the conventional high resolution method provides no eye location estimate, the conventional eye location is estimated from the vector field and compared with the results of the other methods (CHT and hurricane model fit). The maximum speed scale factor and the mean flow parameters are then compared to maximum wind speed and mean flow quantities derived from NCEP winds.

The best track locations are compared to the new eye location derived from the hurricane model fit. Figure 6.8a shows the histogram of the distance between the best track eye locations and the eye locations derived using only the hurricane model for a number of observations of North Atlantic storms from 1999 to 2005. The mean and standard deviation are reported as well. The distribution shows that the majority of cases are at low distance bins, but the mean and standard deviation are quite large. This can be due to several factors such as rain contamination, unmodeled parameters, swath edge effects, land contamination, and including underdeveloped storms in the analysis.

The eye center locations from the CHT method are compared to the best track locations provided by the NHC. The mean and standard deviation of the distance from the interpolated best track location are also calculated for the eye center found by the CHT method. Figure 6.8b shows the histogram of the distance from the best track eye center for the CHT method for the same hurricanes as in Figure 6.8a. The mean is improved over the method that uses only the model fit to find the eye. Note that the size of a typical eye is about 50 km, and as long as the eye center estimate is within the eye wall, the resulting MAP wind fields are good. This suggests that for the majority of cases, both the model based method and the CHT method result in good MAP estimates of the wind field.

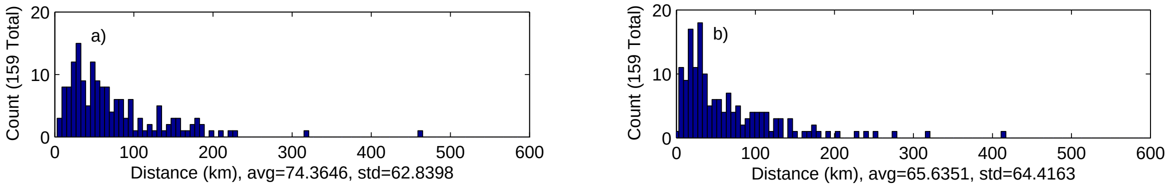

Figure 6.8: Histogram of distance of eye center from best track location for a) the model fit method and b) the circular Hough transform method. Results are derived from 159 North Atlantic named storms from 1999 to 2005.

In order to compare the methods with the conventional approach, the eye centers are estimated using the curl of the vector fields. Figure 6.9 shows the distributions for distance from best track for the conventional high resolution eye, the field-wise MAP eye, and the CHT eye based on the curl of the vector fields. The mean and standard deviation of the field-wise MAP eye and CHT eye are lower than the those corresponding to the conventional eye suggesting that both new methods generally perform better than the conventional method.

The new eye finding method based on the CHT generally improves the eye estimates over the conventional method; however, a human can improve the results even further. Since hurricanes are relatively rare, using human analysts for eye finding is a feasible alternative to purely automated data processing. According to [65], a human in the loop can improve the average error from best track to 21.1 km. However, some storm observations must be discarded in the analysis because the eye center is not obvious to a human. Furthermore, human-based analysis is somewhat subjective. A fully automated method, such as the CHT method, provides objective and timely results.

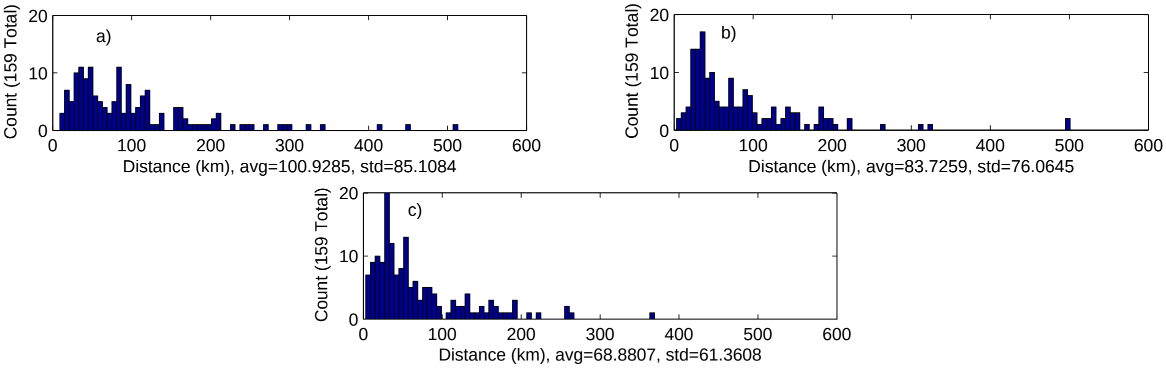

Figure 6.9: Histogram of distance of eye center from best track location for a) the conventional high resolution method, b) the field-wise MAP wind method, and c) the CHT method all based on the curl of the vector fields. The same storms as in Figure 6.8 are used.

We analyze the quality of the other estimated hurricane model parameters (the maximum speed scale factor and the mean flow) using NCEP winds as reference. For both the maximum speed scale factor and the mean flow analysis we manually fix the eye center estimates. First, we compare the estimated maximum speed scale factor to the maximum wind speed reported by the spatially interpolated NCEP wind field. Figure 6.10a illustrates the scatter plot of the maximum speed scale factor versus the maximum NCEP wind speed of several different QuikSCAT observations of hurricanes. The general correlation between the two quantities suggests that the maximum speed scale factor estimates are consistent with the NCEP maximum speed.

We compare the estimates of the mean flow derived from the QuikSCAT data to a mean flow quantity derived from the NCEP winds. The NCEP mean flow is found by taking the vector average of the wind field in the vicinity of the hurricane. Figure 6.10b shows the scatter plot of the magnitude of the mean flow estimate derived from QuikSCAT versus the magnitude of the NCEP mean flow. While the correlation is somewhat weak, the quality of the wind estimates is not particularly sensitive to errors in the magnitude of the mean flow. Figure 6.10c depicts the scatter plot of the direction of mean flow derived from QuikSCAT versus the NCEP direction of mean flow. The mean flow direction derived from QuikSCAT data correlates well with NCEP mean flow, suggesting that the MAP ambiguity selection algorithm estimates the direction of the mean flow relatively well.

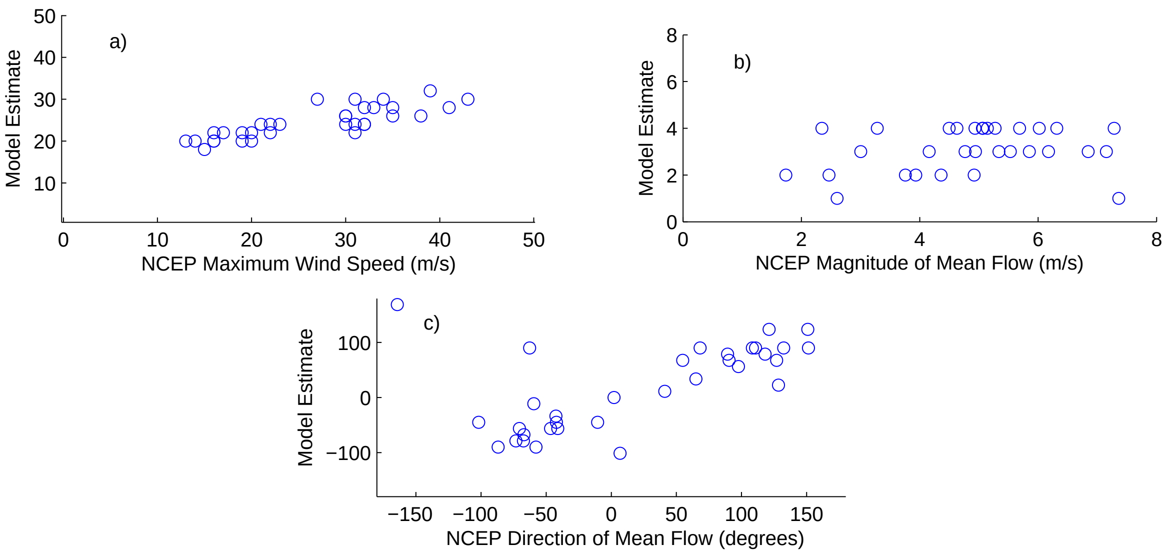

Figure 6.10: Scatter plot of the hurricane model estimates versus corresponding NCEP-derived quantities. a) Maximum speed scale factor. b) Magnitude of mean flow. c) Direction of mean flow.

6.6.3 Accuracy of the Estimated Winds

In order to test the quality of the estimated winds we use the standard H*Wind products. The H*Wind fields are smoothed over several hours and do not exhibit much of the small scale information that exists in the QuikSCAT UHR fields. Nevertheless, we use H*Winds to compare to the new wind estimates because the H*Winds are readily available, are commonly used in hurricane analysis, and are useful for studying the larger scale storm structure [56].

The scatterometer-derived winds are compared to the closest (in time and space) H*Winds for a typical storm observation (Hurricane Isabel 2003). We compare the conventional high resolution winds, the MAP ambiguity selection, and the MAP estimates to the H*Winds and calculate several metrics: the vector RMS difference, the speed difference, and the direction difference. Table 6.2 reports the vector RMS difference, the mean and standard deviation of the speed difference, and the mean and standard deviation of the direction difference for the three wind estimation schemes. The differences are defined as the H*Wind minus the MAP wind quantities. The MAP ambiguity selection method improves the RMS difference and the speed and direction standard deviations over the conventional method, and the MAP estimate improves these same quantities over the MAP ambiguity selection method. This suggests that the MAP estimation procedure produces results more consistent with the standard H*Wind products.

Table 6.2: Differences from H*Winds for the conventional, MAP ambiguity selection, and MAP estimation methods for the observation of Hurricane Isabel 2003.

	Conventional UHR	MAP Ambsel	MAP Estimate
Vector RMS	17.19 m/s	14.60 m/s	10.15 m/s
Speed Mean	4.47 m/s	4.35 m/s	3.90 m/s
Speed Std	6.57 m/s	6.43 m/s	5.31 m/s
Dir Mean	-13.15 deg.	-0.28 deg.	5.65 deg.
Dir Std	42.27 deg.	33.31 deg.	20.51 deg.

Figure 6.11 shows the density plots of the H*Wind wind speed versus the scatterometer winds for the three wind retrieval schemes for the same observation of Hurricane Isabel. The correlation coefficient (ρ) is also reported on the plots. The correlation coefficients for each of the methods are very high but the MAP estimation winds are the highest. This implies that an affine transformation of the MAP estimated wind field is most consistent with the H*Wind field. Note that the general trend of the data is linear with a slope less than one and intercept greater than zero. Applying bias correction (augmenting the retrieved wind speeds so that the slope is one and the intercept is zero) may make the scatterometer data more consistent with the H*Winds. Alternatively, improving the GMF for hurricanes (especially the high wind speeds which tend to be underestimated with the current GMF) may improve the consistency with H*Winds. Nevertheless, in the upper right portion of the images (the high wind speed region) the variance of the data is significantly reduced with the MAP estimation scheme. This suggests that the MAP estimation procedure produces a less noisy (although still biased) estimate of the high wind speeds as compared with H*Winds for this storm observation.

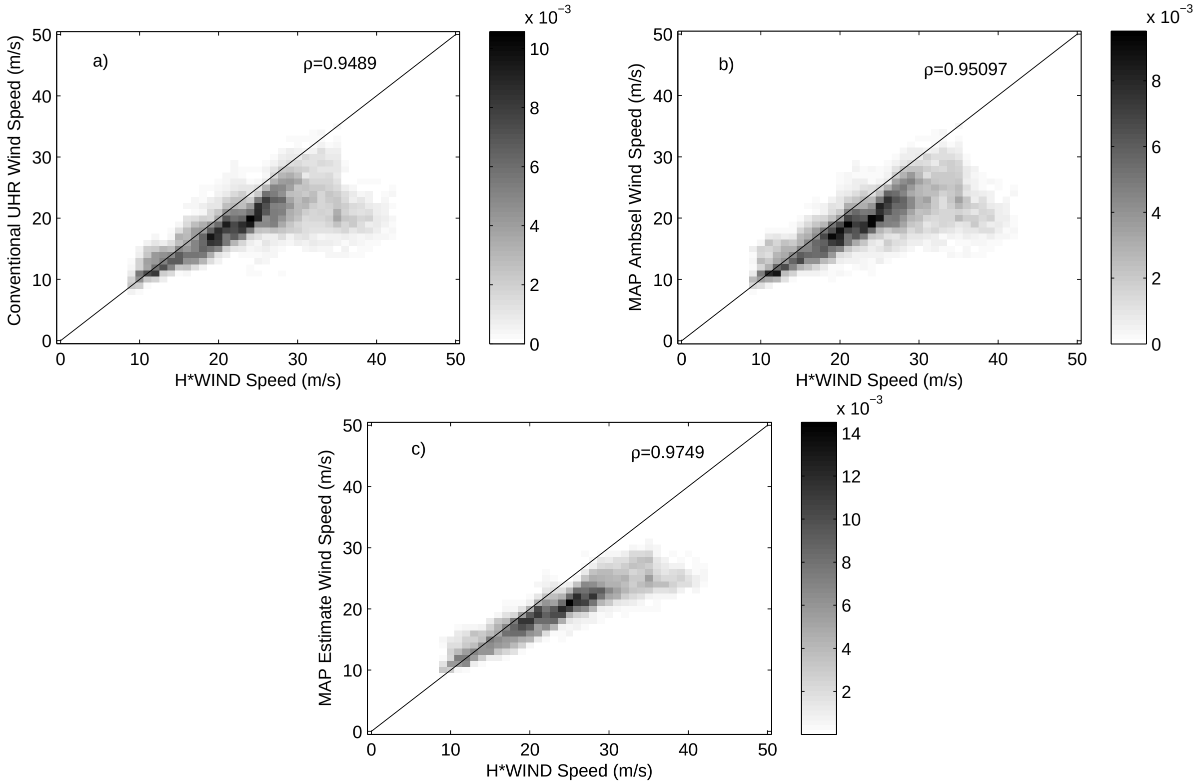

Figure 6.11: Density plots of the H*Wind wind speed versus the scatterometer wind speeds from the three wind retrieval schemes for the observation of Hurricane Isabel 2003. a) Conventional UHR. b) MAP ambiguity selection. c) MAP estimation. The correlation coefficients are also reported.

Figure 6.12 shows an example of a real storm (Floyd 1999). Conventional wind retrieval, field-wise MAP ambiguity selection, and field-wise MAP wind retrieval are all depicted. Using the MAP model reduces the variability of the speed and direction estimates, which gives the illusion of biasing low the wind speed compared to the non-model-based ML estimates. The MAP ambiguity selection routine finds the eye center better than the conventional method and improves the ambiguity selection. The lower left quadrant of the storm where the vectors are pinned in the cross track direction in the conventional high resolution product due to rain contamination are corrected in the MAP ambiguity selection and MAP estimation products. The field-wise MAP wind retrieval method produces a more smooth and less squared off storm than even the field-wise MAP ambiguity selection. This suggests that the MAP estimation procedure may mitigate the directional biases of conventional wind retrieval (which account for some of the squaring off of the storms even in non-raining portions of the storms). Although MAP estimation utilizes a model that does not describe the comma cloud and smaller convective events (speckles in the wind speed image), the MAP estimation method reports a similar speed field structure as the conventional (non-model-based) method.

6.7 Rain and Wind Estimation from SeaWinds in Hurricanes

Using a prior to estimate the wind as described above reduces the effect of rain on the wind estimates. However, where rain rates are large, this method tends to deweight the measurements and impose the model more heavily. The rain contamination issue can be explicitly handled using a simultaneous wind and rain retrieval method at ultra-high resolution (UHRSWR) [66] [50]. However, this further increases the variability of the wind estimates and does not deal with ambiguity selection issues. A potential solution is to combine a MAP estimation scheme with UHRSWR.

This section develops a method for estimating wind and rain in hurricanes at ultra-high resolution from the SeaWinds scatterometer using a MAP estimation approach. A wind and rain prior is employed which reduces the variability of the wind and rain estimates and simplifies ambiguity selection. The procedure uses a simple statistical hurricane wind and rain model to provide prior distributions that are used to modify the maximum likelihood (ML) objective function in the simultaneous wind and rain retrieval step. The low-order hurricane wind and rain prior is derived empirically from SeaWinds and TRMM-PR data.

This section develops the theory and implementation of the new method—simultaneous wind and rain retrieval using MAP estimation (SWRMAP). MAP estimation for hurricane wind and rain retrieval is derived, the wind/rain field model for hurricanes used to generate the priors is developed, and the implementation for SeaWinds is described.

6.7.1 Method

The new method employs MAP estimation to retrieve the wind/rain vector, denoted $\vec{U}[x_j]$, from the reconstructed σ^0 measurement vector, denoted $\vec{\sigma}[x_j]$, at each UHR (2.5 km) pixel, denoted x_j, within a hurricane. Note that the likelihood function $f(\vec{\sigma}[x_j]|\vec{U}[x_j])$ for

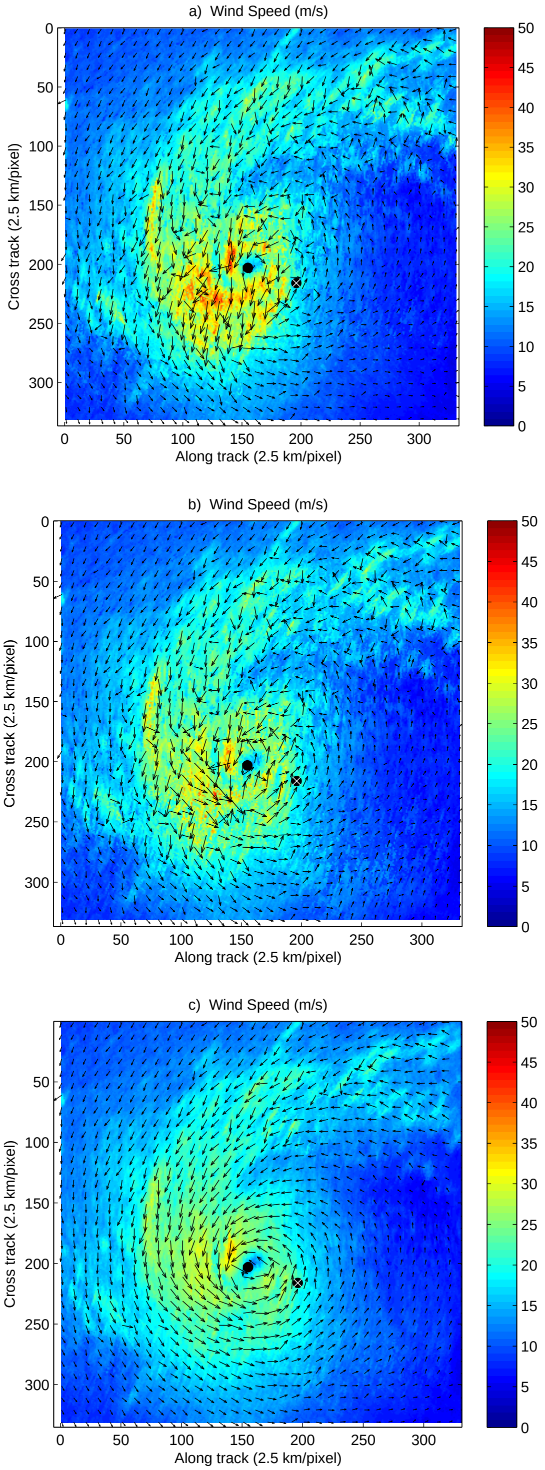

Figure 6.12: Hurricane Floyd (1999) example. a) Conventional UHR wind field. b) The result of the field-wise MAP ambiguity selection. c) The field-wise MAP estimate of the wind field. The wind vector fields are down-sampled by 10 for plotting. The black dots represent the eye center reported by the new method and the black dots with white x's represent the conventional high resolution eye center based on the curl of the vector field. The smoothness of the MAP estimate may be adjusted by scaling the variances of the priors. The MAP estimation uses the variances suggested by the empirical priors.

each pixel x_j may be a multi-modal function of the wind/rain vector, which gives rise to wind/rain ambiguities. However, if an appropriate prior is applied in MAP estimation, the prior term tends to emphasize one particular maximum and suppress the others—generally resulting in a unique wind/rain vector estimate corresponding to the dominant mode.

In this section we use a convex combination of an empirical prior with a non-informative prior for wind and rain in hurricanes. For the wind prior, we use the prior developed above. This prior varies with certain hurricane parameters: the eye center location, maximum speed, and mean flow vector. We also develop a rain prior to add to this model that is a function of the distance between the pixel and the eye center.

Since the empirical prior is a function of the hurricane model parameters, we estimate the hurricane model parameters using the spatial model that relates the parameters of the priors between pixels. We call this relationship between the parameters of the priors the field-wise wind/rain model. We estimate the parameters of the model using model-based ML estimation based on the actual slice σ^0 measurements (not the reconstructed $\vec{\sigma}$ field). Once the model parameters are estimated, the wind/rain field is produced. The wind/rain vector at each pixel is directly related to the parameters of the prior for each pixel. Thus, we can generate the priors for each pixel.

Wind/rain Model

We derive the model for the two-dimensional wind/rain field in a hurricane by using the same wind model developed above and by deriving a simple model for the rain from TRMM-PR data. We restrict the rain model prior to be only a function of the distance from the eye center. Based on several different hurricanes we generate a histogram of all TRMM-PR rain rates greater than zero as a function of distance from the eye center. This produces a general prior for the rain rate given that it is raining $f(10\log_{10}(R)|R > 0)$ as a function of the distance from the eye center.

Figure 6.13 shows the plots of the rain histogram for a particular distance from the eye, as well as the mean and standard deviation as a function of the distance from the eye. The histogram is similar to a Gaussian when the rain rate is expressed in dB. Thus, we assume that the prior is Gaussian in the log of the rain rate. We fit a line to the mean of the

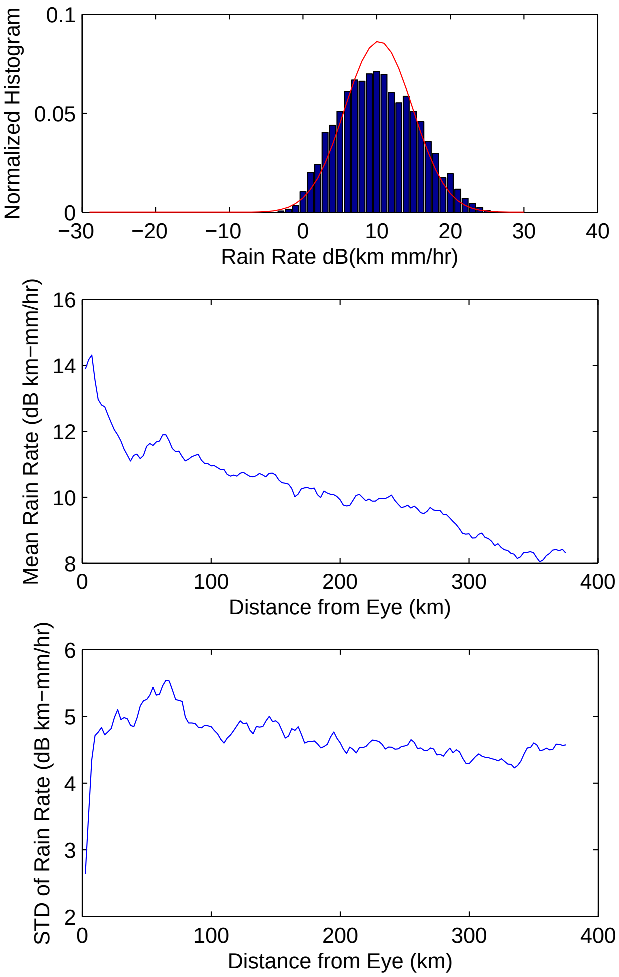

Figure 6.13: TRMM-PR rain rate histogram with Gaussian fit superimposed (top), mean rain rate as a function of distance from the eye (middle), and standard deviation of the rain rate as a function of distance from the eye (bottom).

rain rate as a function of the distance from the eye and assume that the standard deviation is constant at 6 dB km-mm/hr. The form of the rain prior (given that it is raining) is thus

$$f(R_{dB}) = \frac{1}{\xi_R\sqrt{2\pi}} \exp\left\{ -\frac{(R_{dB} - \mu_R)^2}{2\xi_R^2} \right\} \tag{6.10}$$

where μ_R and ξ_R correspond to the mean and standard deviation of the distribution of the rain rate in dB.

Convex Bayes Priors

We combine a uniform prior with the empirical priors to enable control of the impact of the priors on the estimates. We introduce convex combination parameters for the wind speed prior α_s, the wind direction prior α_d, and the rain prior α_r. The convex combination parameters determine how much we impose the empirical priors. Thus, we can increase the convex parameters (i.e., α_s, α_d, and α_r) to obtain a low variability at the expense of suppressing the small scale features or decrease the convex parameters to achieve the opposite. The convex rain prior is of the form

$$f_c(R_{dB}) = \alpha_r f_{Emp}(R_{dB}) + (1 - \alpha_r) f_U(R_{dB}) \tag{6.11}$$

where f_{Emp} is the empirical prior, f_U is the uniform prior, and f_c is the convex prior. Similarly, the wind speed and direction priors can also be combined with a uniform prior. Note that the uniform prior is only constant over the search space (wind speed between 0 m/s and 50 m/s, wind direction between 0^o and 360^o, and rain rates between -10 dB km-mm/hr and 22 dB km-mm/hr).

An information theoretic approach to choosing the convex parameters is considered. We may choose a prior that minimizes the Kullback-Leibler distance or the relative entropy between the ML and MAP probability density functions (pdfs) subject to a constraint on the variability of the estimates. The relative entropy between the MAP and ML pdfs for pixel x_j is [67]

$$D(f(\vec{\sigma}^0[x_j]|\vec{U}[x_j])||f(\vec{U}[x_j]|\vec{\sigma}^0[x_j])) = -\int f(\vec{\sigma}^0[x_j]|\vec{U}[x_j]) \log(f(\vec{U}[x_j])) d\vec{U}[x_j] \tag{6.12}$$

and represents the information added by imposing the prior. The variability of the estimate (first ambiguity) is related to the variance around the dominant peak of the MAP objective function. Thus, we may adjust the convex parameters closer to one in order to narrow the dominant peak due by adding more information from the prior. This method for determining the convex parameters is a function of the measurement geometry and the noise in the measurements, and is complicated to implement. For simplicity, we set the convex parameters to constants. We specifically set the convex parameters α_s, α_d, and α_r to 0.2, 0.3, and 0.1, respectively so that the priors weakly influence the estimates while producing a relatively smooth result. This allows the data to influence the estimates more significantly than directly applying the empirical priors.

Implementation

The first step in the new method is field-wise model-based estimation of the wind/rain field using the hurricane wind/rain field model. This produces estimates of the hurricane model parameters. Model-based maximum likelihood estimation searches for the model instance that maximizes the joint probability of observing the σ^0 slice measurements given that the model instance is the true wind/rain field. Thus, the estimate of the wind/rain field $\hat{\vec{U}}[x]$ is given by

$$\hat{\vec{U}}[x] = \underset{\vec{U}[x]=M(\vec{a})}{\operatorname{argmax}} \left\{ \prod_s f(\sigma_s^0 | \vec{U}[x]) \right\} \tag{6.13}$$

where $\vec{U}[x] = M(\vec{a})$ is the wind/rain field on an $[x]$ grid produced by the wind/rain model $M(\vec{a})$ where $\vec{a}$ represents the model parameters. $f(\sigma_s^0|\vec{U}[x])$ is the pdf of a slice measurement σ_s^0 given the wind, which has the form

$$f(\sigma_s^0|\vec{U}[x]) = \frac{1}{\sqrt{2\pi}\xi_s} \exp\left\{ \frac{-(\sigma_s^0 - \mathrm{gmf}_s(\vec{U}[x]))^2}{2\xi_s^2} \right\} \tag{6.14}$$

where ξ_s^2 is the variance and

$$\mathrm{gmf}_s(\vec{U}[x]) = \sum_x A_s[x] \mathrm{gmf}_t(\vec{U}[x], \theta_s[x], \psi_s[x], pol_s, f_s) \tag{6.15}$$

where gmf_t is the true (high resolution) geophysical model function, $A_s[x]$ is the spatial response function for the slice projected onto the Earth, θ_s is the incidence angle, ψ_s is the azimuth angle, pol_s is the polarization, and f_s is the center frequency of the slice measurement.

Once the hurricane model parameters are estimated, the priors for each pixel are computed and MAP estimation using the priors on the wind speed, wind direction, and rain rate is employed to estimate the wind/rain vector for each pixel using the UHR $\vec{\sigma}$ field. This produces multiple ambiguities similar to ML estimation. However, due to the inclusion of the prior, the first ambiguity (corresponding to the highest maximum) tends to have a likelihood value that is much higher than the others. Thus, we merely choose the first ambiguity as the final estimate and perform no further ambiguity selection. This provides an estimate of the wind/rain vector for each pixel given that it is raining.

In order to include non-raining cases, we perform wind-only retrieval using the MAP estimation scheme with priors on the speed and direction. The first ambiguity provides the best estimate (in the MAP objective function sense) of the wind given that it is not raining. To choose whether the wind-only or the SWR estimate is best, we compare the probabilities (MAP objective function values) weighted by the probability that it is raining. That is, we combine the wind-only and SWR ambiguities to a single set of ambiguities according to

$$f_{new}(\vec{U}_i) = \begin{cases} p(R=0)f_{UHR}(\vec{U}_i) & \text{if } i < 4 \\ p(R>0)f_{SWR}(\vec{U}_{i-4}) & \text{if } i > 4 \end{cases} \tag{6.16}$$

where $p(R=0)$ is the probability that it is not raining and $p(R>0) = 1 - p(R=0)$, and the subscript i indexes the ambiguity. Then, we sort the new list of ambiguities by f_{new}. The final wind/rain estimate for each pixel becomes the first ambiguity of the combined ambiguity list.

Figure 6.14 shows the plot of the probability of false alarm P_{fa} and the probability of missed detection P_{md} versus $p(R=0)$ for a particular storm using TRMM-PR as ground truth. Based on the plot, we set $p(R=0)$ to 0.43 for all cases, which produces a P_{fa} and P_{md} less than 30% for this case.

6.7.2 Analysis

We analyze the MAP estimates of the wind and rain by comparing them to co-located data from other sources. We compare the rain estimates from the new MAP method and the UHRSWR method to TRMM-PR data and the wind estimates to H*Wind fields.

To investigate the quality of the rain estimates we compare the SWR and SWRMAP rain rates to co-located TRMM-PR rain rates of several storms. Figure 6.15 shows a log-

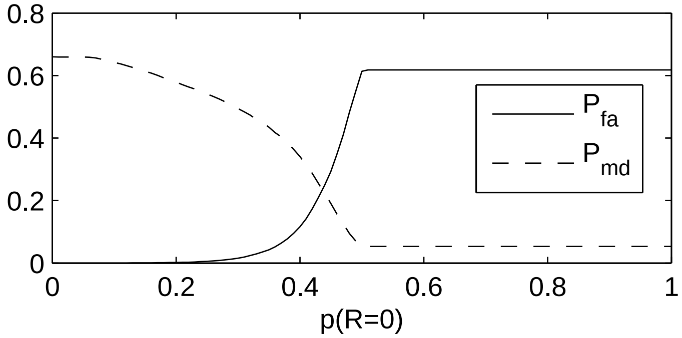

Figure 6.14: Probability of false alarm and probability of missed detection of the rain versus the probability that it is not raining.

density plot of the log of the SWR and SWRMAP rain rates versus the log of TRMM-PR rain rates. There are many low SWR rain rates where the TRMM-PR rain rates are relatively large. This underestimation is corrected in the SWRMAP estimates; however, there is a slight bias of the low rain rates of about 8 dB. This bias is because the rain prior begins to impact the rain estimates more significantly than the likelihood function for low rain rates. That is, scatterometer measurements are not very sensitive to low rain rates (below about 5 km-mm/hr), and thus the MAP estimates of low rain rates rely significantly on the prior. Although the variability of the rain estimates is improved with the SWRMAP method, both the SWRMAP and SWR rain estimates are quite noisy.

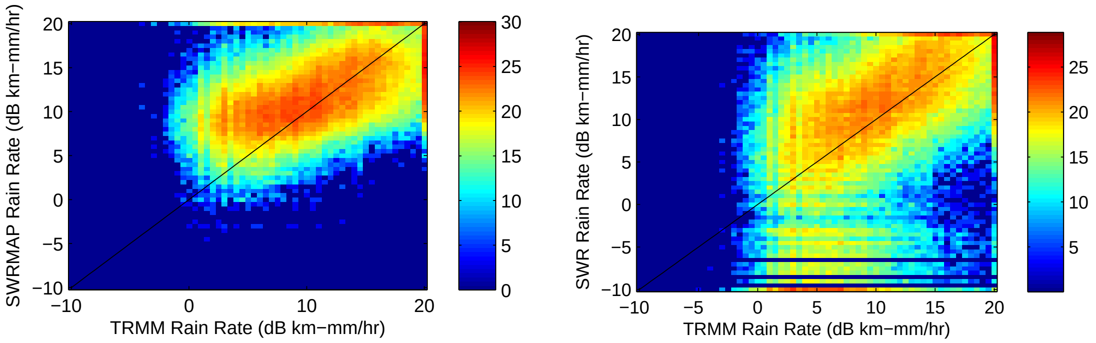

Figure 6.15: Density plots of SWRMAP rain rate versus TRMM-PR rain rate (left) and SWR rain rate versus TRMM-PR rain rate (right).

It is difficult to validate the wind estimates since truth data is limited—we lack co-located wind data of similar temporal and spatial resolution to the UHR products. Nevertheless, we compare the wind speed estimates to the H*Wind product because it is a standard hurricane product and the data is easily accessible. Figure 6.16 shows the log-density plot of the SWRMAP and SWR wind speed estimates for a particular storm (Daniel 2000) in the Eastern Pacific basin. For H*Wind speeds less than about 15 m/s both methods produce similar speed estimates. However, the SWRMAP method reduces the variance of the estimates over the SWR method for H*Wind speeds higher than 15 m/s.

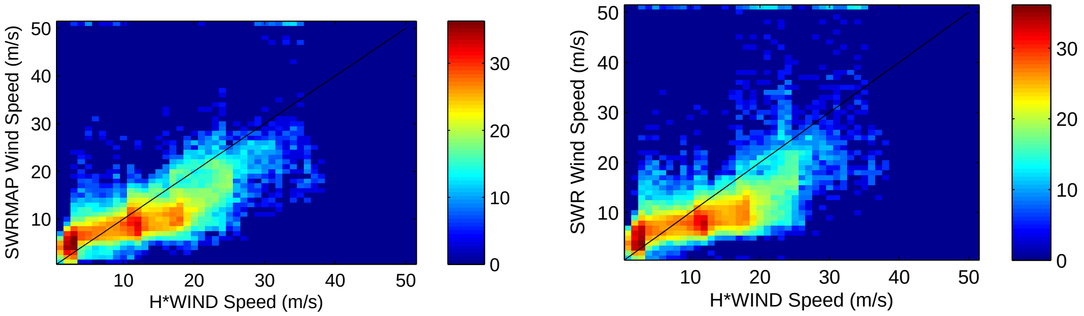

Figure 6.16: Density plots of SWRMAP wind speed versus H*Wind speed (left) and SWR wind speed versus H*Wind speed (right).

Figure 6.17 displays the SWRMAP wind field, the SWR wind field, the SWRMAP rain field and a co-located TRMM-PR rain field for Hurricane Isaac on Sept. 29, 2000. The SWRMAP wind field is much less noisy than the SWR field and the SWRMAP winds in the rain-dominated regime (lower left quadrant) are closer to what is expected in a hurricane. Though noisy, the SWRMAP rain field has a similar spatial structure to the TRMM-PR rain field.

6.8 Conclusion

The field-wise MAP wind retrieval method can be used to augment scatterometer hurricane analysis. It reduces the variability of the wind vector estimates, provides estimates of useful hurricane parameters (such as the eye center location), and improves wind direction

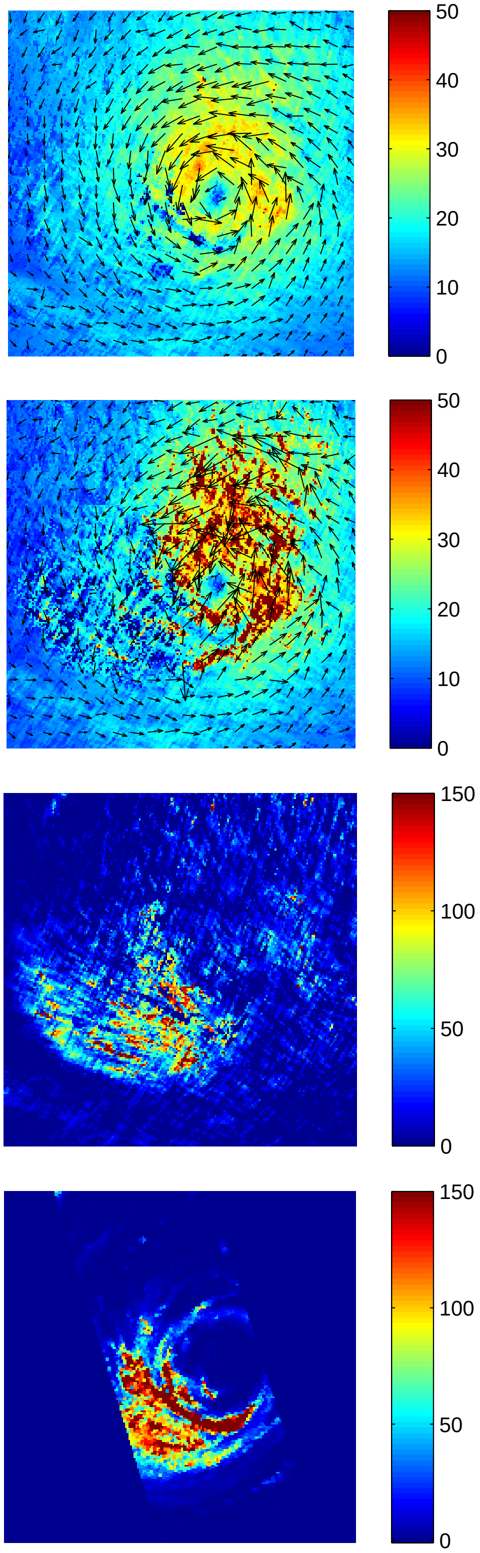

Figure 6.17: SWRMAP wind field (top), SWR wind field (second), SWRMAP rain field (third), and co-located TRMM-PR rain rate (bottom). The colorbar is in m/s for the wind fields and km-mm/hr for the rain fields.

estimates–especially in rain contaminated portions of the storm. Furthermore, the method can be applied in near real time.

The hurricane model is simplistic but appropriate for MAP techniques in well-developed tropical cyclones. Moreover, the MAP procedure allows the operator to vary how much the model is imposed.

This MAP estimation approach mitigates the effects of noise and rain, but relies on a hurricane model fit to generate appropriate prior distributions. Although the new method imposes a low-order model, the effects are less severe than pure model-based methods as the MAP estimation scheme preserves small scale information that is not represented by the model.

MAP ambiguity selection provides an improved selection of the ML ambiguities in tropical cyclones. Although rain and noise artifacts may remain in the result, MAP ambiguity selection imposes the model more weakly than MAP estimation and even standard nudging. Therefore, MAP ambiguity selection may be more appropriate than MAP estimation for certain applications (such as the study of smaller scale structures on the order of 3-10 km).

Simulation suggests that where an eye center can be found in the data, the MAP estimation and MAP ambiguity selection methods are superior to the conventional high resolution approach for all realistic rain rates. The eye center location for the new method is improved over the conventional method (using the curl of the vector fields). However, the eye center estimates may be improved further by a human analyst. Furthermore, the MAP estimation procedure produces results that are more consistent with the standard H*Wind product, although the wind speed estimates tend to remain underestimated compared to H*Winds due to the GMF and rain contamination. The method may be further improved by using quality control and an improved GMF for hurricane conditions (high wind speeds and rain rates).

MAP estimation of hurricane wind and rain fields from the SeaWinds scatterometer is developed. The rain prior is derived from TRMM-PR data as a function of distance from the eye. The SWRMAP estimation method reduces the variability of the rain estimates and corrects the underestimation of low rain rates compared to the ML-based SWR method. The variability of the wind estimates is also reduced with the SWRMAP method.

Future work should include the development of quality control algorithms. Future work could also explore MAP nudging (point-wise MAP ambiguity selection with NWP winds as the mean of the prior), which can be applied to generic wind structures beyond tropical cyclones. The MAP procedure assumes that a hurricane is present in the data. Future research will involve using the MAP model with automatic hurricane detection. UHR and UHR MAP methods can also be considered for C-band scatterometers such as the operational ASCAT scatterometer, which may be less sensitive than SeaWinds to rain.

Chapter 7

Scatterometer Wind Field Reconstruction

A scatterometer is a radar that measures the normalized radar cross section (σ^0) of the Earth's surface. Over the ocean, the backscattered signal is related to the wind through a geophysical model function (GMF). Each σ^0 measurement contains information about the wind averaged over an area. Scatterometers make several measurements over the same spatial region with different geometries, polarizations, and possibly frequencies. These different 'flavors' of measurements can be combined to estimate the wind vector field over the ocean. Several methods of estimating the wind field from the σ^0 measurements have been proposed each having their limitations and imposing different assumptions.

Conventionally the wind field is estimated on a point-wise basis. That is, the scatterometer swath is partitioned into discrete wind vector cells (WVCs) and a single wind vector is separately estimated for each WVC. Standard scatterometer processing employs a drop-in-the-bucket gridding technique using only measurements whose centers fall into a particular WVC to estimate the wind for that WVC, essentially assuming a uniform wind vector field over the WVC. Ultra high resolution (UHR) products have been obtained by reconstructing the σ^0 fields of each flavor separately and then performing point-wise wind retrieval on a high resolution grid [7]. Both of these point-wise methods impose implicit assumptions and neglect spatial correlation between WVCs. A more appropriate way which incorporates the spatial relationship between the measurements is to reconstruct the entire wind field directly from the σ^0 measurements, i.e., field-wise wind estimation.

Field-wise wind estimation has been explored in the past with model based methods [32] [33] [34]. In this approach, the wind field model parameters are estimated from the σ^0 measurements, and the wind field estimate is then computed from the model parameter estimates. However, if the wind field is not in the span of the model, the estimated wind may not be the closest wind field in the space to the true wind field. Furthermore, model-based methods require imposing structure (i.e., the model) on the wind fields, which may be inappropriate for a particular application.

This chapter considers an alternate field-wise approach to reconstruct the wind field directly from the σ^0 measurements. This chapter approaches the scatterometer wind estimation problem as the inversion of a noisy, nonlinear sampling operation, i.e., as a noisy inverse problem. A more general scatterometer sampling model is presented. A Bayesian maximum a posteriori (MAP) estimation method is proposed to reconstruct the wind vector field from the noisy σ^0 measurements. The new approach generalizes and unifies the other wind estimation approaches. The conventional drop-in-the-bucket, UHR, and model-based approaches can be expressed as simplified special cases of the new method. The reconstruction approach is applied to retrieve high resolution wind fields from the SeaWinds scatterometer. The new results are compared to conventional and UHR SeaWinds products.

The chapter is organized as follows. Section 7.1 presents the forward scatterometer sampling operation and shows that it can be made discrete under reasonable assumptions. Section 7.2 presents a method for wind field estimation from noisy scatterometer measurements. Section 7.3 considers the relationship between conventional approaches and the new method. Section 7.4 applies the new approach to the SeaWinds scatterometer. Finally, Section 7.5 summarizes the results and concludes.

7.1 Forward Model

The forward model or sampling operation describes the relationship between the wind field and the scatterometer measurements. This relationship is required to estimate the wind field from scatterometer measurements. This section presents the scatterometer sampling model. Background on sampling and aperture-filtered sampling is presented, the scatterometer sampling operation is stated, the forward operator is made discrete, and the sample spacing or pixel resolution is considered.

7.1.1 Sampling

Sampling is the process of converting a continuous signal into a sequence. Sampling in a Hilbert space can be represented as a sequence of inner products of a signal with sampling functions (i.e., aperture functions). Conventional sampling can be represented as a vector of inner products with Dirac delta functions. In a bandlimited space, this is equivalent to sampling with sinc function apertures [37]. More generally, sampling can be done with irregularly spaced aperture functions with different shapes; such samples are called aperture-filtered samples [2] [38]. In scatterometry, the aperture function is the measurement spatial response function due to the antenna pattern and processing, and sampling is the process of making σ^0 measurements.

Wind scatterometry is an application of aperture-filtered sampling in the sense that each σ^0 measurement represents an aperture-filtered sample of a continuous σ^0 field; however, each measurement samples a different σ^0 field (i.e., measurements are made with different geometries). Over the ocean, the σ^0 fields sampled by a scatterometer are related nonlinearly to the underlying wind field through the geophysical model function (GMF).

7.1.2 Scatterometer Sampling Model

Scatterometers measure the backscattered power from the Earth's surface averaged over the antenna gain pattern. This power measurement is scaled to produce the normalized radar cross section [68]. The measurement of a given scatterometer pulse is partitioned into several 'slice' measurements using range/Doppler processing or pulse compression [10] [8] [9]. The spatial response functions (i.e., aperture functions) of the slice measurements vary in shape and location. Neglecting noise, a particular σ^0 measurement $\sigma^0_{t,i}$ with aperture function $A_i(x)$ is represented by the inner product of a continuous σ^0 field $\sigma^0_{t,i}(x)$ with the aperture function

$$\sigma^0_{t,i} = \int A_i(x)\sigma^0_{t,i}(x)dx \tag{7.1}$$

where x represents a two-dimensional spatial variable. Here, the subscript t indicates that the σ^0 value is the 'true' or noise-free value and i indexes the different measurements.

Over the ocean, the $\sigma^0_{t,i}(x)$ fields are related to the wind vector field $\vec{U}(x)$ through the GMF

$$\sigma^0_{t,i}(x) = \mathrm{gmf}(\vec{U}(x), \theta_i(x), \psi_i(x), pol_i, f_i) = \mathrm{gmf}_i(\vec{U}(x)) \tag{7.2}$$

where $\theta_i(x)$, $\psi_i(x)$, pol_i, and f_i are the incidence angle field, azimuth angle field, polarization, and frequency corresponding to the i^{th} slice measurement respectively. For convenience, these arguments of the GMF are dropped in the rest of the chapter, resulting in the more compact notation $\mathrm{gmf}_i(\vec{U}(x))$. Scatterometers make several measurements with different look geometries over the same spatial region. Stacking the multiple measurements into a vector, the scatterometer sampling model is expressed as

$$\vec{\sigma}^0_t = \begin{bmatrix} \int A_1(x)\mathrm{gmf}_1(\vec{U}(x))dx \\ \vdots \\ \int A_N(x)\mathrm{gmf}_N(\vec{U}(x))dx \end{bmatrix} = \mathcal{T}(\vec{U}(x)) \tag{7.3}$$

where $\mathcal{T}$ is a nonlinear sampling operator that maps the wind field to the noise-free slice measurements.

Equation 7.3 states the forward model (i.e., projecting the wind to the σ^0 measurements); wind field reconstruction involves solving the inverse problem (i.e., estimating the wind from the σ^0 measurements). In theory, the sampling operation can be inverted using constrained optimization (see Appendix C.1). However, in order to simplify the problem and deal with noise appropriately, the problem is solved discretely.

7.1.3 Discrete Model

Here, the sampling operation is transformed into a discrete operation on conventional samples of the wind field (i.e., the forward operation is made discrete). The wind field can be made discrete by assuming that it is bandlimited; however, in order to make the sampling operation discrete, the integrals in Eq. 7.3 must be expressible as summations. Further, not only the wind field but the σ^0 fields $\sigma^0_{t,i}(x)$ corresponding to each measurement i must be bandlimited.

For a general nonlinear function, assuming that the wind field is bandlimited does not necessarily force the corresponding σ^0 fields to be bandlimited. Nevertheless, the GMF can be be expressed in such a way that the σ^0 fields are guaranteed to be bandlimited, but with a potentially different band limit than the wind.

The GMF is an empirical function that can be approximated by a finite power series. In Appendix C.2, it is shown that if the wind field has bandlimited components, and the nonlinear GMF can be represented by a finite power series, then the relationship between the bandlimit of the σ^0 fields ω_σ and the bandlimit of the wind field components ω_{U_1} and ω_{U_2} is (see Appendix C.2)

$$\omega_\sigma \leq P_1\omega_{U_1} + P_2\omega_{U_2} + \omega_a \tag{7.4}$$

where P_1 and P_2 correspond to the order of the power series for the wind vector components and ω_a is the bandlimit of the power series coefficients.

The inequality in Eq. 7.4 states that the bandlimit of the σ^0 fields is generally higher than the bandlimit of the wind field components. This relationship suggests that the regular sample spacing required to represent the σ^0 fields may be finer than the regular sample spacing required to represent the wind field components. Thus, an oversampled version of the wind field with the assumed bandlimit should be projected through the discrete version of $\mathcal{T}$ when calculating the forward projection numerically. However, relatively small errors may result from expressing the σ^0 fields on the same wind field grid (see Appendix C.2).

Thus, if the wind field components are bandlimited, the σ^0 fields are also bandlimited and the sampling operator can be made discrete. The discrete sampling operation can be expressed as

$$\vec{\sigma}_t^0 = \begin{bmatrix} \sum_x A_1[x]\mathrm{gmf}_1(\vec{U}[x]) \\ \vdots \\ \sum_x A_N[x]\mathrm{gmf}_N(\vec{U}[x]) \end{bmatrix} = \mathbf{T}(\vec{U}[x]) \tag{7.5}$$

where the square brackets $[x]$ represent regularly spaced samples on an up-sampled version of the wind field grid (since the σ^0 bandlimit is higher than the wind field bandlimit), and $\mathbf{T}$ is the discrete version of the nonlinear sampling operator $\mathcal{T}$. The Nyquist samples of the wind field, denoted $\vec{U}[x']$, are related to the samples on the higher resolution grid by $\vec{U}[x] = \mathbf{H}\vec{U}[x']$ where $\mathbf{H}$ is the up-sampling operator.

7.1.4 Wind Field Bandlimit and Sample Spacing

As noted, the sampling operator can be made discrete by assuming a bandlimited wind field; however, the bandlimit to assume must be considered. The assumed bandlimit determines the regular sample spacing required to represent the wind field with that bandlimit. This sample spacing provides the pixel resolution on which to reconstruct the wind fields.

Determining the wind bandlimit and the regular sample spacing is much more complicated than the case of linear aperture-filtered sampling with bandlimited aperture functions. In the linear case the sample spacing is determined directly from the highest bandlimit of the aperture functions [2]. With the point-wise nonlinear constraint introduced by the GMF, it may be possible to recover higher frequency content than the bandlimit of the aperture functions (see Appendix C.1). Therefore, the bandlimit or signal structure imposed is based on knowledge of the wind spectrum.

Fortunately, wind generally has a red spectrum that falls off approximately as one over the wave number squared [69]. This allows for the imposition of a relatively low bandlimit without introducing significant aliasing on average. Nevertheless, for particular wind features, such as storms or fronts, the wave number spectrum may have significant high frequency energy. In general, a better result may be obtained by assuming a high bandlimit than to potentially introduce aliasing by assuming a bandlimit that is too low. This suggests that reconstruction be done on the highest resolution grid that is practical and that lower resolution estimates be obtained by low-pass filtering the estimated wind.

7.2 Wind Field Reconstruction from Noisy σ^0 measurements

Wind retrieval from scatterometer measurements is a noisy inverse problem that can be solved using an estimation theory approach. Here, wind field reconstruction from noisy σ^0 measurements over the ocean is considered. A scatterometer noise model is reviewed. A MAP reconstruction estimator is proposed for wind field reconstruction. An appropriate prior to regularize the problem is presented. An approach for practical implementation is also described.

7.2.1 Noise Distribution

The noise distribution for a scatterometer measurement is modeled as a Gaussian random variable with a mean that is the true or noise-free value and a variance that is a quadratic function of the mean [27] [28]. This variance formulation incorporates fading and receiver noise. With this noise model, the vector of noisy σ^0 measurements $\vec{\sigma}^0_m$ can be expressed as

$$\vec{\sigma}^0_m = \vec{\sigma}^0_t + \vec{\nu} \tag{7.6}$$

where $\vec{\sigma}^0_t = \mathbf{T}(\mathbf{H}\vec{U}[x'])$, and $\vec{\nu}$ is a zero-mean Gaussian random vector with a diagonal covariance $\mathbf{R}$. The diagonal terms of the covariance $R_{i,i}$ can be written as

$$R_{i,i} = \alpha_i(\sigma^0_{t,i})^2 + \beta_i\sigma^0_{t,i} + \gamma_i \tag{7.7}$$

where $\sigma^0_{t,i}$ is the i^{th} component of $\vec{\sigma}^0_t$ and α_i, β_i, and γ_i are functions of the scatterometer design and the measured noise power. Note that the expression above assumes that the GMF is a deterministic mapping. Uncertainty in the GMF (or geophysical noise [29]) may be included by modifying the random vector $\vec{\nu}$.

For this chapter, we assume that the geophysical noise is negligible and use the Gaussian noise model described above. This results in the likelihood function

$$f(\vec{\sigma}^0_m|\vec{\sigma}^0_t) = \frac{\exp\{(\vec{\sigma}^0_m - \vec{\sigma}^0_t)^T\mathbf{R}^{-1}(\vec{\sigma}^0_m - \vec{\sigma}^0_t)\}}{(2\pi)^{N/2}|\mathbf{R}|^{1/2}}. \tag{7.8}$$

Note that $f(\vec{\sigma}^0_m|\vec{\sigma}^0_t)$ may also be expressed as $f(\vec{\sigma}^0_m|\vec{U}[x'])$ since $\vec{\sigma}^0_t = \mathbf{T}(\mathbf{H}\vec{U}[x'])$.

A common approach to estimate the parameters of a distribution is maximum-likelihood (ML) estimation. However, at ultra high resolution, the scatterometer wind field estimation problem is generally ill-posed (i.e., there are more parameters to estimate than measurements). To regularize the problem, we propose a Bayesian approach, which employs a prior distribution.

7.2.2 MAP Reconstruction Estimator

Because of the nonlinearity of the GMF, the shape of the noise distribution with respect to the wind is generally multimodal [29]. A maximum a posteriori (MAP) estimator can deal with the potential ambiguity this causes. MAP estimation is Bayesian estimation with a uniform loss function [35] and is similar to maximum-likelihood estimation but also incorporates the prior distribution. The MAP estimator can be expressed as

$$\hat{\vec{U}}_{MAP}[x'] = \underset{\vec{U}[x']}{\operatorname{argmax}} \, f(\vec{\sigma}^0_m|\vec{\sigma}^0_t) f(\vec{U}[x']) \tag{7.9}$$

where $\vec{\sigma}^0_m$ is the noisy measurement vector, $f(\vec{\sigma}^0_m|\vec{\sigma}^0_t)$ is the likelihood function defined in Eq. 7.8, and $f(\vec{U}[x'])$ is a prior distribution. Note that $f(\vec{U}[x'])$ need not be a direct prior of the wind vector field. For example, the prior may be a distribution of some function of the wind field. In practice the MAP log-likelihood function

$$\log f(\vec{\sigma}^0_m|\vec{\sigma}^0_t) + \log f(\vec{U}[x']) \tag{7.10}$$

is used as the MAP objective function.

7.2.3 Prior Distributions

Prior distributions can be obtained in various ways. They can be empirically derived from data, or can be chosen in order to apply additional constraints. For wind scatterometry, prior distributions can both regularize the inverse problem and aid in ambiguity selection. Prior distributions can also be employed to force the wind estimates to be consistent with other wind field estimates with potentially different resolutions.

For the purpose of this chapter, we desire to impose a prior that regularizes the problem without imposing much structure on the wind fields, and without relying too heavily on external data. In order to regularize the problem, we apply a prior that is independent from pixel to pixel. Although a wind field prior may be used, we apply the prior in the σ^0 field domain since it is difficult to obtain a useful direction prior without an external data source. Imposing a prior on the σ^0 fields in this manner can be viewed as estimating the

σ^0 fields via the wind. That is, we reconstruct the σ^0 fields that are consistent with an underlying wind field and simultaneously produce a wind field estimate.

We assume that each pixel of each σ^0 field has the mean of the obtained scatterometer measurement and a finite variance. The Gaussian distribution is the maximum entropy distribution for a given mean and variance, i.e., it imposes the least amount of structure of all distributions with a given mean and variance [67]. Therefore, each pixel of each σ^0 field is assumed to be an independent Gaussian random variable with a mean corresponding to the aperture-filtered σ^0 measurement and a given variance. More precisely, the prior can be expressed as

$$f(\vec{U}[x']) = \prod_{i,x'} f(\sigma^0_{t,i}[x']) = \prod_{i,x'} f(\mathrm{gmf}_i(\vec{U}[x'])) \tag{7.11}$$

where each $f(\mathrm{gmf}_i(\vec{U}[x']))$ is

$$f(\mathrm{gmf}_i(\vec{U}[x'])) = \frac{1}{\sqrt{2\pi}p} \exp\left\{ \frac{-(\sigma^0_{m,i} - \mathrm{gmf}_i(\vec{U}[x']))^2}{2p^2} \right\} \tag{7.12}$$

where p^2 is the variance. Note that for all the pixels of the σ^0 field for a given measurement i, the mean $\sigma^0_{m,i}$ of this prior is constant. Thus, this prior also acts as a smoothing filter on the σ^0 fields and the wind estimates. The variance p^2 is left as a tuning parameter to trade-off spatial resolution for reduced variability of the estimates.

7.2.4 Implementation

Because of the nonlinearity of the GMF and the structure of the noise, the MAP objective function is multimodal. The local maxima represent field-wise ambiguous winds. Although it is theoretically possible to find every local maxima and report them as wind field ambiguities, this is difficult because of the high number of parameters in the wind field reconstruction problem.

For convenience, we employ a gradient search method initializing with an up-sampled result of the standard resolution product. This results in a single wind field estimate. The initialization field effectively acts as an ambiguity selection step since the new method generally converges to a wind field ambiguity close to the initialization field. Alternative initialization fields may be obtained from ultra high resolution (UHR) processing, model-based wind field estimation from the σ^0 data, or data from external sources. Note that the wind field may be estimated in meridional and zonal components or in speed and direction components. We search along the gradient with respect to the wind speed and direction components, since it is simpler to search numerically due to the structure of the objective function. The gradient of the MAP objective function is provided in Appendix C.5.

7.3 Connections Between Approaches

The new approach solves the general inverse problem by regularizing via a prior. The conventional approaches, which apply assumptions and approximations to solve the problem, can be expressed as simplified special cases of the new method. The implicit assumptions made by the drop-in-the-bucket and UHR methods have the effect of regularizing the wind inversion problem by enabling point-wise wind field estimation. This section explores the relationship between the new approach and the standard drop-in-the-bucket, UHR, and model-based approaches.

7.3.1 Drop-in-the-bucket Approach

First, consider the drop-in-the-bucket approach. This approach uses multiple measurements whose aperture-function centers fall into a WVC to independently estimate a wind vector for that cell [31]. In relation to the sampling model in Eq. 7.3, this can be viewed as assuming that the wind field is piece-wise constant over the WVCs and that the aperture functions are delta functions. That is, under the implicit assumptions, each row of the sampling model can be expressed as

$$\sigma^0_{d,i} = \int \delta(x - x_i)\mathrm{gmf}_i(\vec{U}(x))dx = \mathrm{gmf}_i(\vec{U}(x_i)) \tag{7.13}$$

where x_i is the center of the aperture function for measurement i and $\vec{U}(x_i) = \vec{U}(x_j)$ for all x_i, x_j in the same WVC. We use the notation $\sigma^0_{d,i}$ to represent the i^{th} σ^0 measurement for the drop-in-the-bucket method. The vector of σ^0 measurements for the drop-in-the-bucket method is expressed as $\vec{\sigma}^0_d$. Note that since the true wind field is not piece-wise constant and the aperture functions are not delta functions, the drop-in-the-bucket technique, in effect, solves a different problem than the original. The errors introduced by the implicit assumptions made using drop-in-the-bucket methods can be evaluated by

$$\begin{aligned}
\left|\left|\vec{\sigma}_t^0 - \vec{\sigma}_d^0\right|\right|_{L_1} &= \sum_i \left|\sigma_{t,i}^0 - \vec{\sigma}_{d,i}^0\right| \\
&= \sum_i \left| \int A_i(x)\mathrm{gmf}_i(\vec{U}(x))dx - \mathrm{gmf}_i(\vec{U}(x_i)) \right| \\
&= \sum_i \left| \int A_i(x)[\mathrm{gmf}_i(\vec{U}(x)) - \mathrm{gmf}_i(\vec{U}(x_i))]dx \right| \\
&\leq \sum_i \int A_i(x) \left| \mathrm{gmf}_i(\vec{U}(x)) - \mathrm{gmf}_i(\vec{U}(x_i)) \right| dx. \qquad (7.14)
\end{aligned}$$

If the wind field is relatively smooth, $\left|\mathrm{gmf}_i(\vec{U}(x)) - \mathrm{gmf}_i(\vec{U}(x_i))\right|$ is generally small for each i and the L_1 normed difference between the forward projections is small. However, for wind fields with significant small scale structure, the normed difference may be large, resulting in biases in the wind estimates.

While the drop-in-the-bucket sampling operation differs from the new method, the noise model is the same. This results in a similar expression for the likelihood function $f(\vec{\sigma}_m^0|\vec{\sigma}_d^0)$ as expressed in Eq. 7.8 but with $\vec{\sigma}_t^0$ replaced by $\vec{\sigma}_d^0$.

It can be shown that the MAP reconstruction method for estimating the wind reduces to the conventional method, assuming the drop-in-the-bucket forward model and a particular prior. First, suppose we apply the new field-wise approach to estimate the wind from the σ^0 measurements assuming the drop-in-the-bucket forward operation. The assumption that the wind field is piecewise constant makes the problem discrete, albeit in a different way than assuming that the wind fields are bandlimited. To solve this discrete problem using the MAP reconstruction approach, a gradient search is used. With the drop-in-the-bucket forward model, the gradient of the likelihood function defined in Appendix C.5 Eq. C.20 reduces to

$$\frac{\partial \log f(\vec{\sigma}_m^0|\vec{U}[x'])}{\partial U_j[x]} = \begin{cases} \sum_i K_i \frac{\partial \mathrm{gmf}_i(\vec{U}[x])}{\partial U_j[x]} & \text{if } x' = x \\ 0 & \text{otherwise} \end{cases} \qquad (7.15)$$

where the square brackets $[x]$ represent regular sampling of the piece-wise constant wind field (i.e., one sample per WVC). Note that the partial derivative of the likelihood function with respect to the wind at a particular WVC is not a function of the wind in other WVCs. This implies that the wind vector at each WVC can be estimated independently (i.e., point-wise).

Note that the above expression is the gradient of the likelihood function without the prior. As long as some measurements fall into every WVC, the wind can be estimated point-wise for each WVC without a prior (i.e., the Fisher information matrix is diagonal and not singular). Thus, the implicit assumptions in the modified forward model effectively regularize the problem. If no prior is imposed (or equivalently if a non-informative prior is used), the MAP reconstruction approach reduces to conventional processing, when assuming the drop-in-the-bucket forward model. We note, however, that the new approach provides more control of how the problem is regularized and allows for higher resolution wind estimates than possible with conventional drop-in-the-bucket methods.

7.3.2 UHR Approach

The UHR approach assumes a similar forward model as in Eq. 7.3, but modifies it slightly by making an important assumption. UHR processing assumes that measurements of a similar geometry (and same polarization and frequency) sample the same wind-dependent σ^0 field.

More precisely, each row of the UHR sampling operation is expressed as

$$\sigma^0_{UHR,i} = \int A_i(x)\mathrm{gmf}_f(\vec{U}(x))dx \tag{7.16}$$

where $\mathrm{gmf}_f(\vec{U}(x))$ represents the σ^0 field of a given flavor (e.g., consecutive measurements from the same beam). Under the UHR assumption, each $\sigma^0_{UHR,i}$ of a particular flavor samples the same $\mathrm{gmf}_f(\vec{U}(x))$. The multiple measurements of a given flavor are combined to reconstruct the σ^0 field of a given flavor, and this is done for each different flavor. The wind is then estimated point-wise from the reconstructed σ^0 fields [7].

Although the assumption is that multiple measurements sample the same σ^0 field, each measurement actually samples a slightly different σ^0 field because each measurement views the surface with a slightly different geometry. The error introduced by this assumption can be evaluated as

$$\begin{aligned}
\left|\left|\vec{\sigma}^0_t - \vec{\sigma}^0_{UHR}\right|\right|_{L_1} &= \sum_i \left|\sigma^0_{t,i} - \vec{\sigma}^0_{UHR,i}\right| \\
&= \sum_i \left| \int A_i(x)\mathrm{gmf}_i(\vec{U}(x))dx - \int A_i(x)\mathrm{gmf}_f(\vec{U}(x))dx \right| \\
&= \sum_i \left| \int A_i(x)[\mathrm{gmf}_i(\vec{U}(x)) - \mathrm{gmf}_f(\vec{U}(x))]dx \right| \\
&\leq \sum_i \int A_i(x) \left|\mathrm{gmf}_i(\vec{U}(x)) - \mathrm{gmf}_f(\vec{U}(x))\right| dx
\end{aligned} \qquad (7.17)$$

where $\vec{\sigma}^0_{UHR}$ is the vector of measurements assuming the UHR forward model, and $\mathrm{gmf}_f(\vec{U}(x))$ is the σ^0 field assuming the geometry of flavor f. Note that $\mathrm{gmf}_i(\vec{U}(x))$ is the actual σ^0 field that is sampled by the i^{th} measurement and differs from $\mathrm{gmf}_f(\vec{U}(x))$ because of a slightly different viewing geometry. The normed difference between the forward projections is relatively small if the change in the GMF with respect to the differences in the geometry between the actual measurements i and the assumed look geometry are small over the main lobe of $A_i(x)$. For scatterometer designs with narrow measurement spatial response functions, this assumption is appropriate, but for scatterometer systems with broad measurement response functions, this assumption may result in significant bias errors.

The noise model assumed for UHR processing differs from the standard noise model. Although the UHR noise model is derived from the standard noise model, the UHR model assumes each pixel to be statistically independent, resulting in a diagonal covariance matrix. Also, the mean of the distributions for each pixel are assumed to be the true σ^0 value at the given pixel (i.e., $\sigma^0_{t,i}[x] = \mathrm{gmf}_i(\vec{U}[x])$ for pixel x).

Note that if the covariance is assumed to be diagonal, it is generally non-singular (except possibly if there are WVCs that happen to be in a null of every aperture function). This implicit assumption regularizes the problem making point-wise estimation possible without imposing a prior. If no prior is imposed (or equivalently if a non-informative prior is used) MAP reconstruction reduces to point-wise UHR estimation, when assuming the UHR forward operation and noise model.

The actual noise distribution of the reconstructed σ^0 fields has correlation among adjacent WVCs due to the measurement overlap, resulting in a non-diagonal covariance matrix. Although the UHR assumptions simplify the problem and result in useful estimates, assuming that the covariance is diagonal may result in artifacts when the actual correlation is significant.

The modifications to the noise model used in UHR processing regularize the inverse problem (i.e., they make the underdetermined forward model invertible) and make point-wise retrieval possible, but are somewhat ad-hoc. An alternate method may be to regularize the problem by adding a diagonal to the singular covariance matrix. In fact, this is equivalent to applying an independent Gaussian prior to each pixel of the reconstructed σ^0 fields and performing MAP estimation on a field-wise basis, similar to what is proposed above. This suggests that for systems where measurements of a similar flavor can be combined, the prior in Eq. 7.12 may be modified by replacing the mean $\sigma^0_{m,i}$ with the reconstructed σ^0 value for a given pixel.

7.3.3 Model-based Approach

Model-based estimation assumes that the true wind field is contained in the span of the wind field model. The model parameters are estimated from the measurements and then a wind field estimate is computed from the model parameter estimates. Generally, a model is chosen so that there are fewer parameters to estimate than measurements, thus regularizing the problem. The parameters are conventionally estimated using maximum likelihood estimation [32] [33] [34]. Note that assuming that the wind field is in the span of a wind field model is equivalent to imposing a uniform prior over the range space of the wind field model. Thus, model-based methods can also be expressed as a special case of the MAP reconstruction approach.

7.4 Application to SeaWinds

This section considers the application of the MAP wind reconstruction method to the SeaWinds scatterometer. Here, background on the sensor is provided, examples are presented, and the MAP reconstruction estimates are compared to conventional products. Simulation is employed to analyze the quality of the estimates.

7.4.1 SeaWinds Background

SeaWinds is a Ku-band scanning pencil-beam scatterometer. Two beams (v-pol and h-pol) at two different nominal incidence angles are employed to produce a wide swath with sufficient azimuth diversity to infer wind direction. Range/Doppler filtering is employed to obtain several σ^0 measurements ('slices') for each radar pulse [8]. The aperture function of each slice σ^0 measurement is a function of the antenna pattern and the range/Doppler processing. In practice, the aperture functions can be approximated by a binary mask (i.e., a mask with ones within the 6dB main lobe and zeros outside) [43].

For SeaWinds, the wind is conventionally estimated on a 25km grid (L2B), 12.5km grid (L2BH), and a 2.5km grid (UHR). For the L2B product, the slices of a given pulse are first averaged together into 'egg' measurements and the eggs whose centers fall into a 25km wind vector cell (WVC) are used to estimate the wind vector for that WVC [8]. A similar procedure is done for the L2BH product, only the measurements are binned on a 12.5km grid [8]. UHR processing first reconstructs four σ^0 fields, one for each flavor (v-pol and h-pol, fore- and aft- looking), onto a 2.5km grid using a weighted average of all the slice σ^0 values weighted by the respective aperture functions [24] [25]. The wind is then estimated point-wise from the reconstructed σ^0 fields [7]. We compare the results of these different methods with the new MAP reconstruction method.

7.4.2 Example

Figures 7.1 and 7.2 illustrate an example of wind field reconstruction from the SeaWinds scatterometer for a wind field with relatively small scale features. The L2B, UHR, and MAP estimated wind speed fields are shown in Fig. 7.1, while the direction fields are plotted in Fig. 7.2. The new method improves the resolution over the L2B product, producing a wind field similar to the UHR field but with less noise.

Figures 7.3 and 7.4 display the speed difference fields and direction difference fields between the various methods respectively. The difference between the MAP and L2B fields,

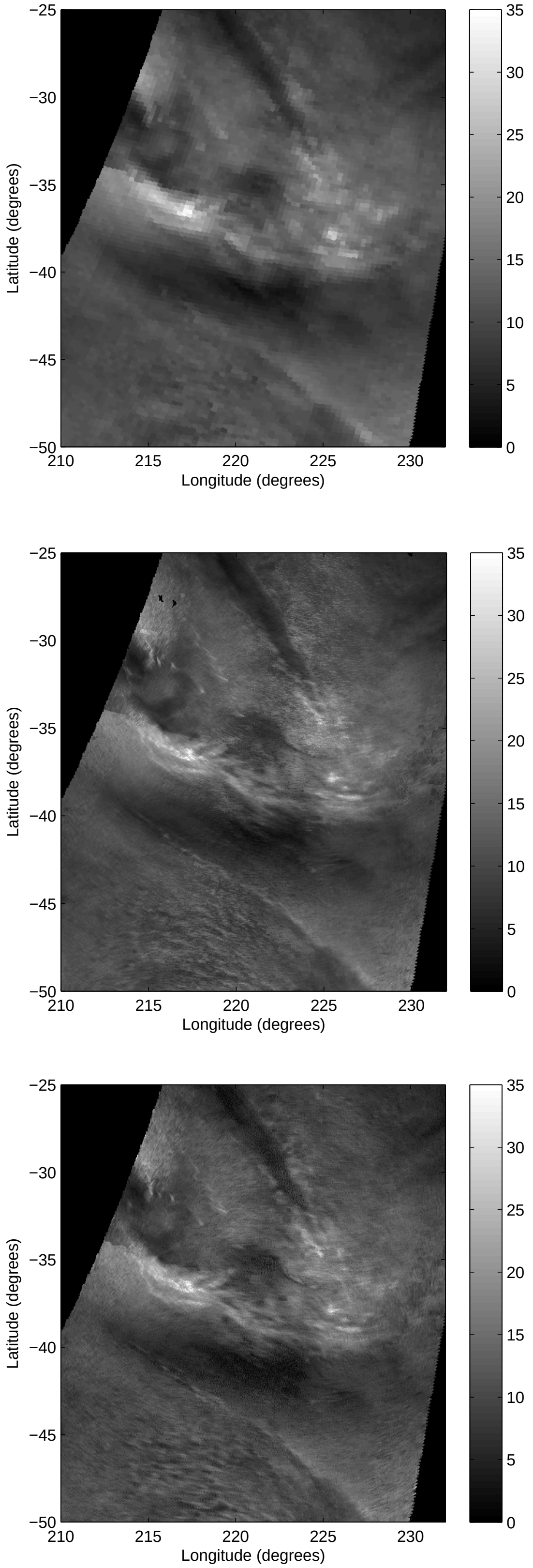

Figure 7.1: Wind speed fields in m/s from L2B (top), UHR (middle), and MAP reconstruction (bottom).

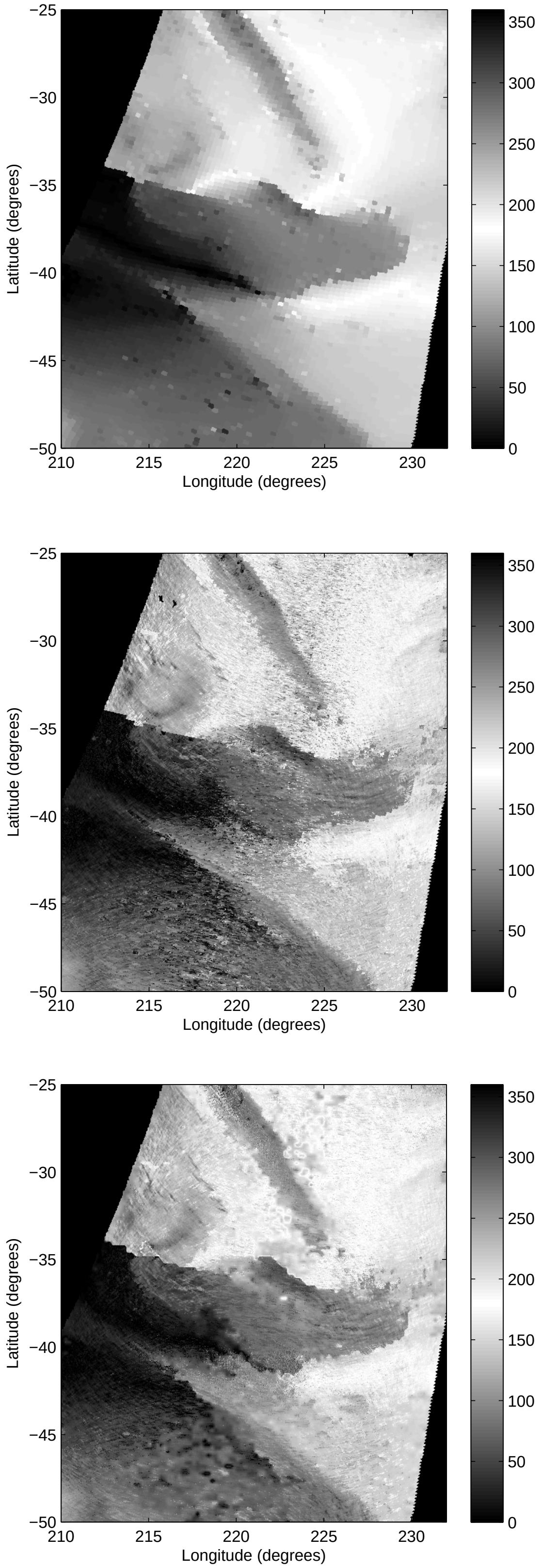

Figure 7.2: Wind direction fields in degrees relative to north from L2B (top), UHR (middle), and MAP reconstruction (bottom).

the MAP and UHR fields, and the UHR and L2B fields are all shown. These images suggest that the MAP estimates are consistent with the L2B and UHR estimates throughout the swath. The UHR speed and direction estimates are noisy in the nadir region, while the MAP direction estimates appear less noisy. Note that the differences between the UHR and L2B, and the MAP and L2B wind estimates are also due in part to the differing resolutions of the products.

7.4.3 Validation

It is difficult to evaluate the quality of the wind estimates without an independent set of collocated data of a similar resolution. Lacking such data, we compare the MAP reconstruction results to the conventional low resolution results and to the UHR product for 20 SeaWinds passes in the south Atlantic (i.e., a 6×6 degree window around latitude -30, longitude -130). The south Atlantic is chosen for convenience to avoid the tropics where rain contamination is significant. Tables 7.1 and 7.2 show the speed and direction mean difference, standard deviation (STD) of the difference, and the root mean squared (RMS) difference between the MAP reconstructed winds and the L2B winds, between the UHR winds and L2B winds, and between the MAP reconstructed winds and the UHR winds. For Table 7.1 the L2B winds are up-sampled (using nearest neighbor interpolation) to the high resolution grid, while for Table 7.2 the MAP and UHR winds are averaged down (using a vector average) to the L2B resolution. The results suggest that the MAP reconstruction method is consistent with the standard SeaWinds product and with the UHR product. The mean difference (or bias) with respect to the L2B is low for both UHR and MAP wind estimation. The standard deviation and RMS differences suggest that the MAP estimates are generally less noisy than the UHR products.

7.4.4 Simulation

To further investigate the performance of the new method, we employ Monte-Carlo simulation. Estimates of the bias and variance of the estimates of the L2B, UHR, and MAP reconstruction wind retrieval methods are also obtained using simulation.

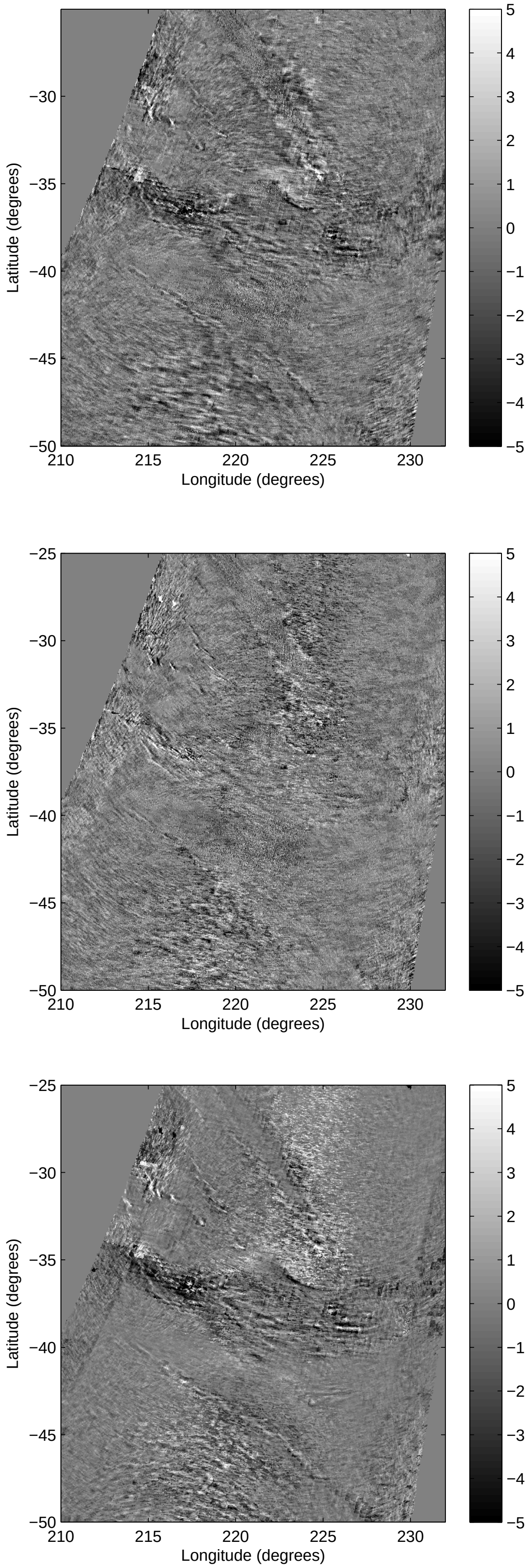

Figure 7.3: Wind speed difference fields in m/s from difference between MAP and L2B (top), difference between MAP and UHR (middle), and difference between UHR and L2B (bottom).

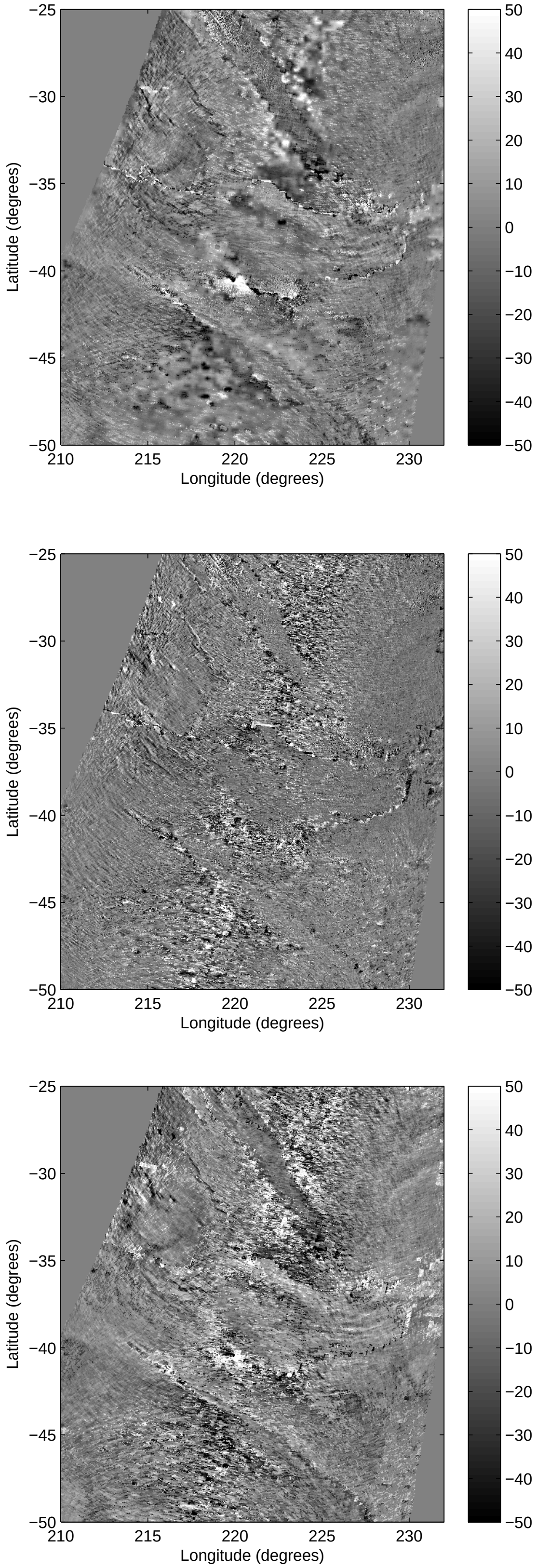

Figure 7.4: Wind direction difference fields in degrees between MAP and L2B (top), between MAP and UHR (middle), and between UHR and L2B (bottom).

Table 7.1: Mean difference, standard deviation of the difference, and RMS difference between MAP and L2B, and between MAP and UHR estimated wind speeds and directions at UHR resolution (averaged over 20 passes in the south Atlantic).

	Mean	STD	RMS
MAP − L2B speed	-0.46	1.32	1.40
UHR − L2B speed	-0.23	1.53	1.55
MAP − UHR speed	-0.24	1.40	1.42
MAP − L2B dir	-1.78	17.03	17.13
UHR − L2B dir	0.22	26.08	26.08
MAP − UHR dir	-2.01	27.09	27.16

Table 7.2: Mean difference, standard deviation of the difference, and RMS difference between MAP and L2B, and between MAP and UHR estimated wind speeds and directions at L2B resolution (averaged over 20 passes in the south Atlantic).

	Mean	STD	RMS
MAP − L2B speed	-0.98	1.14	1.50
UHR − L2B speed	-1.26	1.22	1.76
MAP − UHR speed	0.28	0.63	0.69
MAP − L2B dir	-1.98	8.38	8.60
UHR − L2B dir	-1.40	9.26	9.37
MAP − UHR dir	-0.58	5.93	5.96

A comprehensive simulation and analysis is beyond the scope of this chapter and is the subject of future research. Here, we analyze the results from a particular wind field with 100 independent noise realizations. We generate a simulated wind field that has a wave number spectrum that falls off as one over the wave number squared. Figure 7.5 plots the wind speed and direction field used in simulation. Although this wind field may not be realistic, it exhibits small scale structure necessary to test the resolution of the estimates.

Figures 7.6 and 7.7 show the scatter density plots of the MAP and UHR estimates compared to the true wind for the wind speed and direction, respectively, for a particular noise realization. The plots suggest that the MAP direction estimates are less noisy than the UHR estimates. The MAP speed estimates of high wind speeds have a slightly lower variability than the UHR estimates while the variability at low wind speeds is higher.

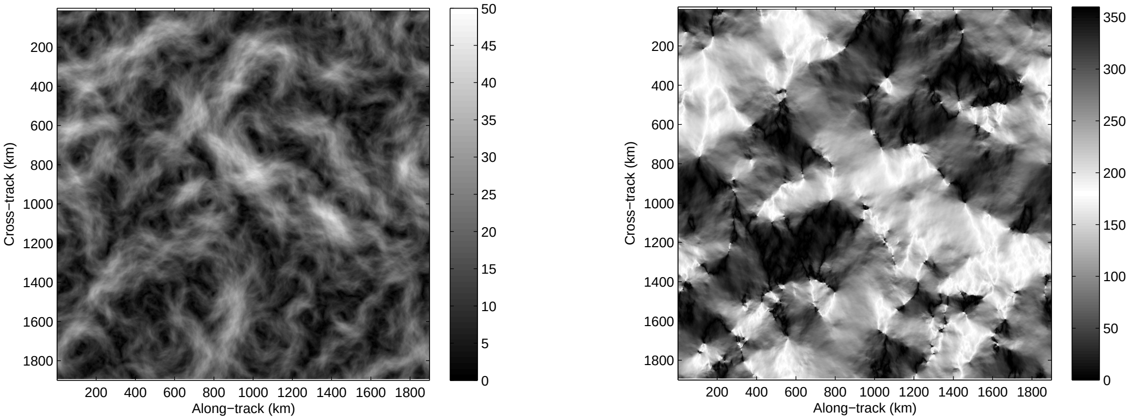

Figure 7.5: Simulation wind speed field in m/s (left) and direction field in degrees (right).

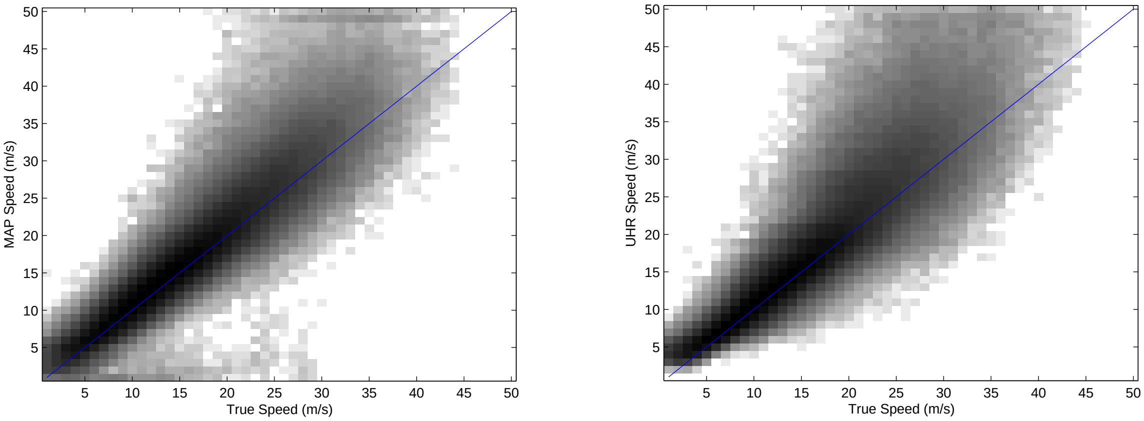

Figure 7.6: Scatter density plots of wind speed obtained in simulation for MAP (left) and UHR (right).

Figures 7.8 and 7.9 plot the bias of the wind speed and direction estimates, respectively, for the MAP and UHR methods. For both methods higher wind speeds tend to produce a larger bias, although the bias of MAP reconstruction estimates are less severe than the UHR estimates. In the swath edges the structure of the bias seems to be different from the inner swath. The direction estimates are relatively unbiased except in frontal features.

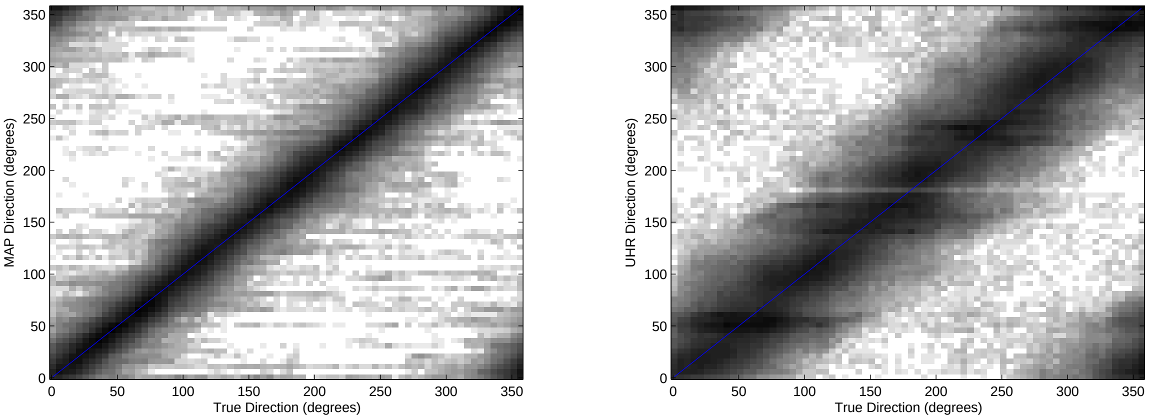

Figure 7.7: Scatter density plots of wind direction obtained in simulation for MAP (left) and UHR (right).

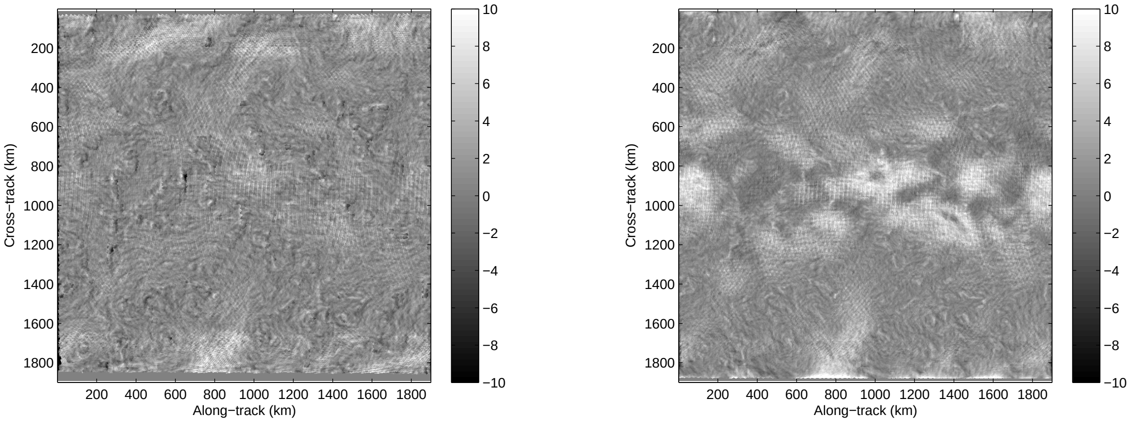

Figure 7.8: Bias of wind speed estimates in (m/s) for MAP (left) and UHR (right).

Figures 7.10 and 7.11 plot the standard deviation of the wind speed and direction estimates, respectively, for the MAP and UHR methods. As expected the MAP estimates of high wind speeds have a lower standard deviation than the UHR estimates. The standard deviation of the direction fields is much different for the UHR and MAP estimates. In the nadir region, the UHR direction estimates have a large standard deviation, whereas the MAP estimates have a relatively low standard deviation all throughout the swath.

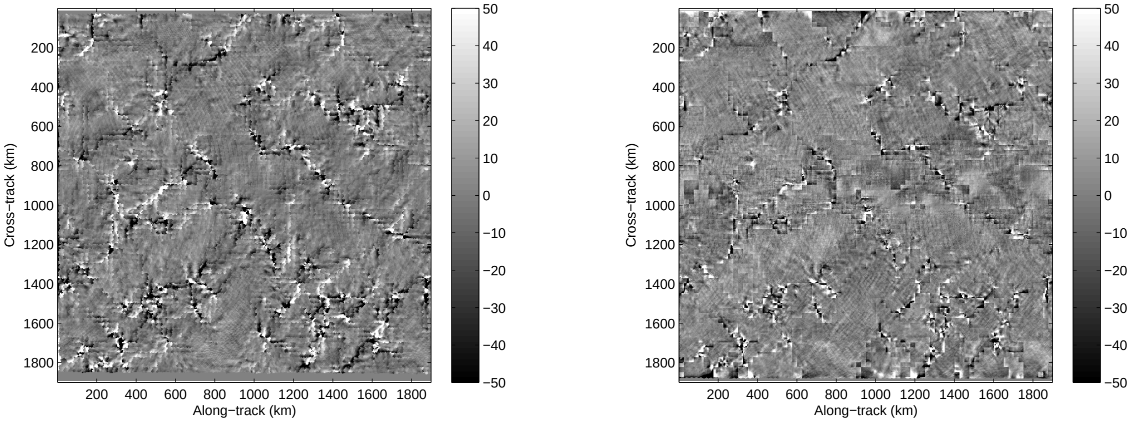

Figure 7.9: Bias of wind direction estimates in degrees for MAP (left) and UHR (right).

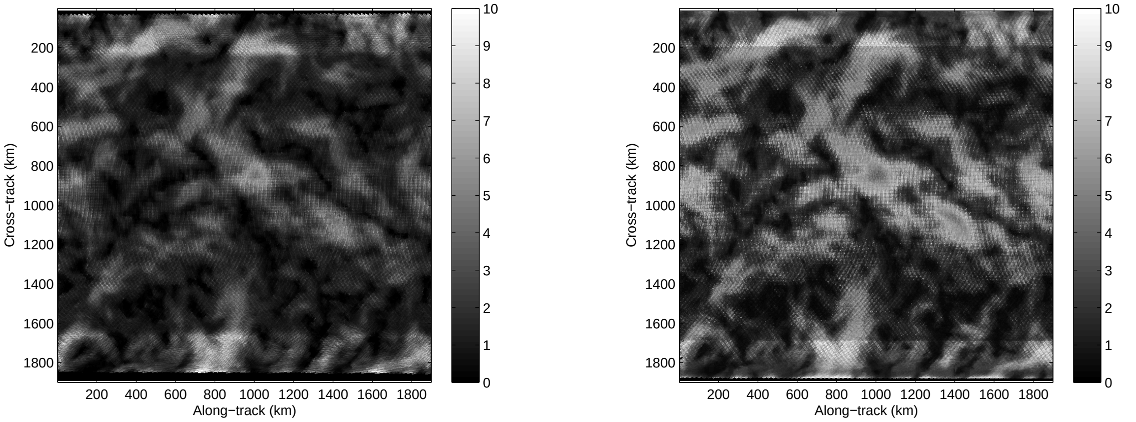

Figure 7.10: Standard deviation of wind speed estimates in (m/s) for MAP (left) and UHR (right).

7.5 Conclusion

This chapter approaches the scatterometer wind field estimation problem in a novel way. Wind field estimation is performed on a field-wise basis without imposing a low-order model. MAP estimation is employed to estimate regularly spaced samples of the wind field at ultra high resolution. The method is applied to the SeaWinds scatterometer and the results are compared to standard products. The MAP reconstruction method is consistent with low resolution standard products but provides higher resolution information. For SeaWinds,

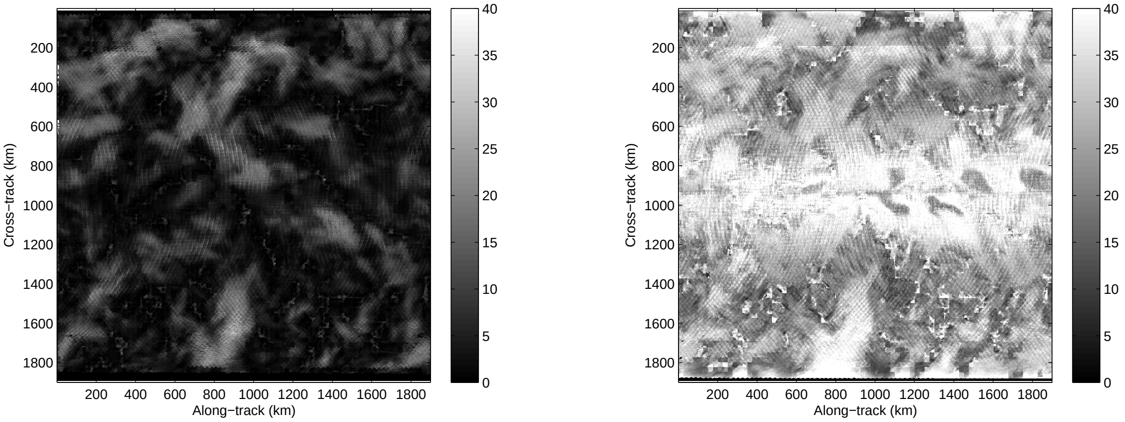

Figure 7.11: Standard deviation of wind direction estimates in degrees for MAP (left) and UHR (right).

the MAP reconstruction estimates are consistent with the UHR estimates, but produce less noisy estimates.

Future research may include a more rigorous validation of the MAP reconstruction product for the SeaWinds scatterometer. Also, the approach can be applied to operational scatterometer data, such as the advanced scatterometer (ASCAT), and adapted for a near real time ultra high resolution product. The MAP reconstruction approach can also be extended to simultaneously reconstruct wind and rain vector fields from scatterometer measurements.

Chapter 8

Conclusion

This dissertation approaches the problems of scatterometer image reconstruction and wind estimation from a new perspective. Scatterometer image reconstruction methods are extended to appropriately handle scatterometer noise. Wind estimation from the σ^0 measurements is treated as a nonlinear extension of the new scatterometer image reconstruction approach, dealing with noise and the nonlinearity introduced by the GMF. Ultra high resolution wind field estimation is revisited and formalized. Several new algorithms for scatterometry are presented and analyzed, including MAP σ^0 reconstruction, point-wise MAP UHR wind estimation, and MAP wind field reconstruction. The theory and results provide new insight into the scatterometer σ^0 imaging and wind estimation problems. Although the new methods have been implemented for the SeaWinds scatterometer, the general approach to scatterometry developed in the dissertation is applicable to any scatterometer design and may influence the design of future scatterometers.

With the new field-wise approach, issues such as observability, identifiability, and resolution of the σ^0 and wind fields can be addressed from a field-wise perspective. The new approach generalizes and unifies previous wind estimation approaches as special cases of a more general solution. The relationship between the different wind estimation approaches can now be analyzed under one unified theory.

8.1 Summary of Contributions

The major contributions of the dissertation are published or in review, comprising three journal articles [1] [2] [3] (with [2] and [3] currently in review), and several conference papers [4] [5] [6] [7]. The three journal articles consider the three major topics of the dissertation: σ^0 imaging, UHR wind estimation, and wind field reconstruction. Contributions include new theoretical perspectives, and development and analysis of improved processing algorithms. The contributions to each topic of the dissertation are summarized below.

For σ^0 imaging, the theory of aperture-filtered sampling and reconstruction is developed and reconstruction is extended to deal with noise. A MAP reconstruction method is developed. Trade-offs and issues with choosing different prior distributions are discussed. The method is implemented for the SeaWinds and ASCAT scatterometers. The MAP method results in high resolution σ^0 images, without the ad-hoc processing steps of the SIR algorithm. Appropriate priors can be chosen to reduce noise and sampling artifacts. The MAP reconstruction approach with a near non-informative prior produces higher resolution images than the SIR method and does not rely on ad-hoc tuning methods. However, the noise level is typically higher than with the SIR method. The MAP method may be tuned to trade-off noise for resolution explicitly and can produce images of a similar resolution and noise level as the SIR method.

For UHR wind estimation, several theoretical issues are dealt with, and novel approaches to reduce noise and improve ambiguity selection are developed. The UHR noise and measurement models are formally developed and the implicit assumptions involved are explicitly stated. Point-wise MAP estimation using a prior that is a function of a wind field model is developed and applied to the case of hurricane wind and rain field estimation. The UHR MAP approach improves ambiguity selection, reduces the variability of the estimates, and produces results more consistent with what is expected in hurricanes (see Chapters 5 and 6). However, the UHR MAP approach developed in Chapter 6 depends on a simplified hurricane model that is derived from standard UHR SeaWinds data.

For wind field reconstruction, wind estimation is generalized to handle spatial correlation introduced by the irregular sampling operation. A MAP wind field reconstruction estimator is developed and the method is applied to the SeaWinds scatterometer. The results are compared to the conventional L2B and UHR products. The MAP reconstruction approach produces ultra high resolution wind field estimates that are consistent with both the L2B and UHR products, but with a lower variability and bias. For SeaWinds, MAP wind field reconstruction results in a lower bias than the conventional UHR approach. The variability of the MAP speed estimates is similar to the conventional UHR estimates, but the variability of the MAP direction estimates is significantly lower–especially in the nadir region of the swath. MAP wind reconstruction using a gradient search method also resolves the issue of ambiguity selection, effectively using the initialization field as a type of nudging field. This results in a much simpler solution than the conventional point-wise approach of reporting every possibly point-wise ambiguity as a potential solution.

8.2 Logical Extensions and Future Work

Although the algorithms are implemented only for particular scatterometers, the theory developed in the dissertation applies generally to any scatterometer design. The processing methods developed here may be applied effectively to other scatterometers. The hurricane estimation approach would be particularly interesting to apply to a C-band scatterometer such as ASCAT because the rain effects are generally less severe than for Ku-band. Also, a UHR wind product can be developed for ASCAT using the concepts developed in this dissertation. A UHR ASCAT wind product could provide important information on smaller scale wind structures for operational weather now-casting, forecasting, and post-casting. Furthermore, SeaWinds MAP σ^0 imaging and wind estimation approaches may be standardized as operational products, which would require a more thorough validation and quality control analysis with in-situ data.

The approach taken to the scatterometer problem can be applied to many microwave remote sensing problems. For example, microwave imaging using synthetic aperture radar can be expressed as a special case of reconstruction from aperture-filtered samples. Also, the approach can be applied to passive microwave systems, such as radiometers, to reconstruct images of brightness temperature or other geophysical parameters from the raw measurements. Both of these applications would be particularly interesting because the noise model may be treated as additive white Gaussian noise.

Bibliography

[1] B. A. Williams and D. G. Long, “Estimation of hurricane winds from SeaWinds at ultra high resolution,” *IEEE Transactions on Geoscience and Remote Sensing*, 2008. 3, 61, 127

[2] ——, “Reconstruction from aperture-filtered samples with application to scatterometer image reconstruction,” *IEEE Transactions on Geoscience and Remote Sensing*, 2010, in review. 3, 4, 15, 39, 103, 106, 127

[3] ——, “Scatterometer wind field reconstruction,” *IEEE Transactions on Geoscience and Remote Sensing*, 2010. 3, 4, 127

[4] ——, “An improved high resolution wind ambiguity removal procedure for seawinds,” in *Proceedings of the International Geoscience and Remote Sensing Symposium*, Denver, Colorado, 2006, pp. 2643–2646. 3, 127

[5] ——, “Hurricane wind field estimation from SeaWinds at ultra high resolution,” *IGARSS*, 2007. 3, 61, 127

[6] ——, “Rain and wind estimation from SeaWinds in hurricanes at ultra high resolution,” *IGARSS*, 2008. 3, 61, 127

[7] B. A. Williams, M. P. Owen, and D. G. Long, “The ultra high resolution QuikSCAT product,” in *Procedings of the 2009 IEEE Radar Conference.* Pasadena, CA: IEEE, May 2009. 3, 6, 12, 45, 101, 112, 115, 127

[8] T. Lungu, *QuikSCAT Science Data Product Users Manual Overview and Geophysical Data Products*, September 2006. 5, 10, 43, 62, 81, 103, 115

[9] *ASCAT Wind Product User Manual*, August 2009. 5, 10, 43, 103

[10] M. W. Spencer and D. G. Long, “High resolution measurements with a spaceborne pencil-beam scatterometer using combined range/doppler discrimination techniques,” *IEEE Transactions on Geoscience and Remote Sensing*, vol. 41, no. 3, pp. 567–581, 2003. 5, 103

[11] F. T. Ulaby, R. K. Moore, and A. K. Fung, *Microwave Remote Sensing.* Artech House, 1981, vol. 2. 5

[12] D. G. Long, R. S. Collyer, R. Reed, and D. V. Arnold, “Dependence of the normalized radar cross section of water waves on bragg wavelength-wind speed sensitivity,” *IEEE Transactions on Geoscience and Remote Sensing*, vol. 34, no. 3, May 1996. 5

[13] D. G. Long and P. J. Hardin, "Vegetation studies of the amazon basin using enhanced resolution seasat scatterometer data," *IEEE Transactions on Geoscience and Remote Sensing*, vol. 32, no. 2, pp. 449–460, 1994. 6

[14] P. J. Hardin and D. G. Long, "Discriminating between tropical vegetation formations using reconstructed high-resolution Seasat-A scatterometer data,," *Photogrammetric Engineering and Remote Sensing*, vol. 60, no. 12, pp. 1453–1462, Dec 1994. 6

[15] D. Long, M. Drinkwater, B. Holt, S. Saatchi, and C. Bertoia, "Global ice and land climate studies using scatterometer image data," *EOS, Transaction of the American Geophysical Union*, vol. 82, no. 43, p. 503, 2001. 6

[16] H. Anderson and D. Long, "Sea ice mapping method for seawinds," *IEEE Transactions on Geoscience and Remote Sensing*, vol. 43, no. 2, pp. 237–246, 2005. 6

[17] Q. Remund and D. Long, "Large-scale inverse ku-band backscatter modeling of sea ice," *IEEE Transactions on Geoscience and Remote Sensing*, 2003. 6

[18] J. Haarpainter and G. Spreen, "Use of enhanced-resolution quikscat/seawinds data for operational ice services and climate research: Sea ice edge, type, concentration, and drift," *IEEE Transactions on Geoscience and Remote Sensing*, vol. 45, no. 10, pp. 3131–3137, 2007. 6

[19] I. Ashcraft and D. Long, "Observation and characterization of radar backscatter over greenland," *IEEE Transactions on Geoscience and Remote Sensing*, vol. 43, no. 2, pp. 237–246, 2005. 6

[20] ——, "Relating microwave backscatter azimuth modulation to surface properties of the greenland ice sheet," *Journal of Glaciology*, vol. 52, no. 177, pp. 257–266, 2006. 6

[21] M. S. L. Wang, B. Rivard, and K. Steffen, "Melt season duration and ice layer formation on the greenland ice sheet," *Journal of Geophysical Research*, vol. 112, 2007. 6

[22] H. Stephen and D. G. Long, "Microwave backscatter modeling of erg surfaces in the sahara desert," *IEEE Transactions on Geoscience and Remote Sensing*, vol. 43, no. 2, pp. 237–246, 2005. 6

[23] ——, "Spatial and temporal behavior of microwave backscatter directional modulation over the saharan ergs," *IEEE Transactions on Geoscience and Remote Sensing*, vol. 45, no. 5, pp. 1164–1173, 2007. 6

[24] D. G. Long, P. J. Hardin, and P. T. Whiting, "Resolution enhancement of spaceborne scatterometer data," *IEEE Transactions on Geoscience and Remote Sensing*, vol. 31, 1993. 7, 39, 40, 44, 115

[25] D. S. Early and D. G. Long, "Image reconstruction and enhanced resolution imaging from irregular samples," *IEEE Transactions on Geoscience and Remote Sensing*, vol. 39, no. 2, pp. 291–302, 2001. 9, 16, 25, 39, 40, 115

[26] H.Hersbach, “CMOD5–an improved geophysical model function for ERS C-band scatterometry,” European Centre for Medium-Range Weather Forecast, Tech. Rep., 2003. 10, 62

[27] R. E. Fischer, “Standard deviation of scatterometer measurements from space,” *IEEE Transactions on Geoscience and Remote Sensing*, vol. GE-10, no. 2, April 1972. 11, 40, 41, 107

[28] M. W. Spencer and D. G. Long, “Radar backscatter measurement accuracy for a spaceborne pencil-beam wind scatterometer with transmit modulation,” *IEEE Transactions on Geoscience and Remote Sensing*, vol. 35, no. 1, pp. 102–114, Jan 1997. 12, 107

[29] D. G. Long and J. M. Mendel, “Identifiability in wind estimation from wind scatterometer measurements,” *IEEE Transactions on Geoscience and Remote Sensing*, vol. 29, no. 2, pp. 268–276, 1991. 12, 107, 108

[30] T. E. Oliphant, “New techniques for wind scatterometry,” Master’s thesis, Brigham Young University, 1996. 12, 156

[31] C.-Y. Chi and F. K. Li, “A comparative study of several wind estimation algorithms for spaceborne scatterometers,” *IEEE Transactions on Geoscience and Remote Sensing*, vol. 26, no. 2, March 1988. 12, 110

[32] D. G. Long, “Wind field model-based estimation of SEASAT scatterometer winds,” *Journal of Geophysical Research*, vol. 98, no. C8, pp. 14,651–14,688, August 1993. 13, 101, 114

[33] D. G. Long and J. M. Mendel, “Model-based estimation of wind fields over the ocean from scatterometer measurements part i: The wind field model,” *IEEE Transactions on Geoscience and Remote Sensing*, vol. 28, no. 2, pp. 349–360, May 1990. 13, 101, 114

[34] ——, “Model-based estimation of wind fields over the ocean from scatterometer measurements part ii: Estimation of the model parameters,” *IEEE Transactions on Geoscience and Remote Sensing*, vol. 28, no. 2, pp. 361–373, May 1990. 13, 101, 114

[35] T. D. Moon and W. C. Stirling, *Mathemetical Methods and Algorithms for Signal Processing.* Prentice Hall, 2000. 15, 17, 24, 26, 32, 34, 108, 155

[36] A. Tarantola, *Inverse Problem Theory and Methods for Model Parameter Estimation.* Philadelphia: Society for Industrial and Applied Mathemetics, 2005. 15

[37] A. V. Oppenheim and R. W. Schafer, *Discrete-time Signal Processing*, 2nd ed., A. V. Oppenheim, Ed. Upper Saddle River, New Jersey: Prentice Hall, 1999. 16, 17, 18, 103

[38] H. G. Feichtinger and K. Grochenig, “Irregular sampling theorems and series expansions of band-limited functions,” *Journal of Mathematical Analysis and Applications*, 1992. 16, 103

[39] ——, “Iterative reconstruction of multivariate band-limited functions from irregular sampling values,” *SIAM J. of Math. Anal.*, vol. 23, no. 1, pp. 244–261, January 1992. 16

[40] K. Grochenig, “Iterative reconstruction of multivariate band-limited functions from irregular sampling values,” *Mathematics of Computation*, vol. 59, no. 199, pp. 181–194, July 1992. 16, 25

[41] R. Franz and D. G. Long, “Multidimensional reconstruction from irregular samples,” in *Optical Society of America Technical Digest: Signal Recovery and Synthesis*, Albuquerque, New Mexico, 5-8 Nov. 2001, pp. 135–137. 16

[42] A. V. Oppenheim and A. S. Willsky, *Signals and Systems*, 2nd ed., A. V. Oppenheim, Ed. Pearson Education. 19, 168

[43] I. S. Ashcraft and D. G. Long, “The spatial response function of SeaWinds backscatter measurements,” in *Procedings of SPIE*, W. L. Barnes, Ed., vol. 5151, SPIE, Bellingham, WA, Aug 2003. 44, 115

[44] R. Lindsley and D. G. Long, “Adapting the SIR algorithm to ASCAT,” Brigham Young University Microwave Remote Sensing Laboratory, Tech. Rep., 2009. 44

[45] D. G. Long, “High resolution wind retrieval from SeaWinds,” *IGARSS*, pp. 751–753, 2002. 51, 61

[46] D. G. Long, J. B. Luke, and W. Plant, “Ultra high resolution wind retrieval from SeaWinds,” *IGARSS*, pp. 1264–1266, 2003. 51

[47] J. B. Luke, “High resolution wind retrieval for SeaWinds on QuikSCAT,” Master’s thesis, Brigham Young University, 2003. 51, 53

[48] S. J. Shaffer, R. S. Dunbar, S. V. Hsiao, and D. G. Long, “A median-filter-based ambiguity removal algorithm for NSCAT,” *IEEE Transactions on Geoscience and Remote Sensing*, vol. 29, no. 1, January 1991. 57

[49] D. W. Draper and D. G. Long, “Evaluating the effect of rain on seawinds scatterometer measurements,” *Journal of Geophysical Research*, vol. 109, no. C02005, 2004. 61, 70

[50] ——, “Simultaneous wind and rain retrieval using SeaWinds data,” *IEEE Transactions on Geoscience and Remote Sensing*, vol. 42, no. 7, pp. 1411–1423, 2004. 61, 81, 88

[51] C. Nie and D. G. Long, “A c-band wind/rain backscatter model,,” *IEEE Transactions on Geoscience and Remote Sensing*, vol. 45, no. 3, pp. 621–631, 2007. 61

[52] ——, “A c-band scatterometer simultaneous wind/rain retrieval method,” *IEEE Transactions on Geoscience and Remote Sensing*, vol. 46, no. 11, pp. 3618–3632, 2008. 61

[53] S. H. Yueh, B. W. Stiles, W.-Y. Tsai, H. Hu, and L. W. T., "QuickSCAT geophysical model function for tropical cyclones and application to Hurricane Floyd," *IEEE Transactions on Geoscience and Remote Sensing*, vol. 39, no. 12, pp. 2601–2612, Dec 2001. 62, 71

[54] N. Suzuki, M. A. Donelan, and W. J. Plant, "On the sub-grid-scale variability of oceanic winds and the accuracy of numerical weather prediction models as deduced from QuikSCAT backscatter distributions," *Journal of Geophysical Research*, vol. 112, 2007. 62

[55] M. Portabella and A. Stoffelen, "Scatterometer basckscatter uncertainty due to wind variability," *IEEE Transactions on Geoscience and Remote Sensing*, vol. 44, no. 11, Nov 2006. 62

[56] M. D. Powell, S. H. Houston, L. R. Amat, and N. Morisseau-Leroy, "The HRD real-time hurricane wind analysis system," *Journal of Wind Engineering and Industrial Aerodynamics*, pp. 53–64, 1998. 62, 81, 85

[57] W. J. Pierson, Jr., "Probabilities and statistics for backscatter estimates obtained by a scatterometer," *Journal of Geophysical Research*, vol. 94, no. C7, pp. 9743–9759, July 1989. 64

[58] A. C. Lorenc, "Analysis methods for numerical weather preditction," *Q. J. R. Meteorol. Soc.*, 1986. 67

[59] M. Portabella and A. Stoffelen, "A probabilistic approach for Sea Winds data assimilation," *Q. J. R. Meteorol. Soc.*, 2004. 67

[60] A. Stoffelen and M. Portabella, "On Bayesian scatterometer wind inversion," *IEEE Transactions on Geoscience and Remote Sensing*, vol. 44, no. 6, 2006. 67

[61] W. C. Stirling and D. R. Morrell, "Convex bayes decision theory," *IEEE Trans. on Systems, Man, and Cybernetics*, vol. 21, no. 1, 1991. 70

[62] C. Mears, D. Smith, and F. Wentz, "Detecting rain with QuikSCAT," *IGARSS*, 2000. 70

[63] J. N. Huddleston and B. W. Stiles, "A multi-dimensional histogram technique for flagging rain contamination on QuikSCAT," *IGARSS*, 2000. 71

[64] M. Portabella and A. Stoffelen, "Characterization of residual information for SeaWinds quality control," *IEEE Transactions on Geoscience and Remote Sensing*, 2002. 71

[65] R. R. Halterman and D. G. Long, "A comparison of hurricane eye determination using standard and ultra-high resolution QuikSCAT winds," *IGARSS*, 2006. 83

[66] M. P. Owen and D. G. Long, "Progress toward validation of QuikSCAT ulrta-high-resolution rain rates using TRMM PR," *IGARSS*, 2008. 88

[67] T. M. Cover and J. A. Thomas, *Elements of Information Theory.* Wiley Interscience, 2005. 92, 109

[68] F. T. Ulaby, R. K. Moore, and A. K. Fung, *Microwave Remote Sensing.* Artech House, 1981, vol. 1. 103, 175

[69] M. H. Freilich and D. B. Chelton, "Wavenumber spectra of pacific winds measured by the Seasat scatterometer," *Journal of Physical Oceanography*, vol. 16, no. 4, April 1986. 106, 160

[70] D. W. Draper and D. G. Long, "An advanced ambiguity selection algorithm for SeaWinds," *IEEE Transactions on Geoscience and Remote Sensing*, vol. 41, no. 3, March 2003. 160

[71] D. G. Long, "Model-based estimation of wind fields over the oceans from wind scatterometer measurements," Ph.D. dissertation, University of Southern California, January 1989. 161

[72] M. H. Hayes, *Statistical Digital Signal Processing and Modeling.* Wiley, 1996. 167

[73] L. Cohen, *Time-Frequency Analysis*, A. V. Oppenheim, Ed. Prentice Hall, 1995. 170

[74] M. A. Richards, *Funamentals of Radar Signal Processing.* McGraw-Hill, 2005. 173

Appendix A

List of Acronyms

GMF	geophysical model function
UHR	ultra high resolution
SWR	simultaneous wind and rain
WVC	wind vector cell
MAP	maximum aposteriori
ML	maximum-likelihood
ASCAT	Advanced scatterometer
QuikSCAT	SeaWinds scatterometer on the QuikSCAT platform
TRMM-PR	precipitation radar on the tropical rain measurement mission
AVE	averaging reconstruction algorithm
AART	additive algebraic reconstruction technique
MART	multiplicative algebraic reconstruction technique
SIR	scatterometer image reconstruction algorithm
L2B	level 2B standard 25 km SeaWinds wind product
NWP	numerical weather prediction
NCEP	National Centers for Environmental Prediction
H*Wind	hurricane wind model from the National Hurricane Center
CHT	circular Hough transform
RMS	root mean square
pdf	probability density function
SFIC	σ^0 filtering with inconsistency correction algorithm

Appendix B

Appendix to Chapter 3

This appendix provides derivations and theoretical results connected with aperture-filtered sampling and reconstruction discussed in Chapter 3. First, the subtleties associated with processing continuous signals as discrete signals are considered. Reconstruction estimators are then derived for the additive white Gaussian noise case. Then, the scatterometer ML reconstruction estimator is derived.

B.1 Discrete Equivalence of Bandlimited Signals

Here, the conditions are considered under which the continuous-index sampling operation $\mathcal{A}$ is equivalent to a discrete linear operation on the conventional samples. First, it is shown that if each $A_n(x)$ is bandlimited, the sampling can be represented by Eq. 3.3. The same result is obtained if $s(x)$ is bandlimited, even if each $A_n(x)$ is not bandlimited. Next, it is shown that if $s(x)$ or each $A_n(x)$ is bandlimited and periodic then $\mathbf{A}$ is a finite dimensional matrix and can be analyzed with standard linear algebra.

First consider the case in which each $A_n(x)$ is bandlimited to ω_0 and both $s(x)$ and each $A_n(x)$ are in the Hilbert space of square integrable functions (L_2). From conventional reconstruction theory recall that any function $f(x)$ that is bandlimited to ω_0 can be represented by sinc-function interpolation from the conventional (uniformly spaced) samples $f[x_n]$, and $f(x)$ can thus be expressed as

$$f(x) = \sum_n f[x_n]\mathrm{sinc}(\omega_0(x - x_n)). \tag{B.1}$$

If each of the aperture functions $A_n(x)$ are bandlimited to ω_0 then each row of the sampling operation in Eq. 3.2 can be written as

$$\begin{aligned}\int A_n(x)s(x)dx &= \int \sum_i A_n[x_i]\mathrm{sinc}(\omega_0(x - x_i))s(x)dx \\ &= \sum_i A_n[x_i] \int \mathrm{sinc}(\omega_0(x - x_i))s(x)dx \\ &= \sum_i A_n[x_i]s_{BL}[x_i] \qquad \text{(B.2)}\end{aligned}$$

where $s_{BL}[x_i]$ represents the conventional samples of a bandlimited version of $s(x)$ and $A_n[x_i]$ represents the conventional samples of the aperture functions. The sampling operation can thus be written as a discrete linear operation on the samples of a bandlimited version of the signal.

By a similar argument if $s(x)$ is bandlimited, but the $A_n(x)$'s are not necessarily bandlimited, a similar result is obtained

$$\begin{aligned}\int A_n(x)s(x)dx &= \int \sum_i \mathrm{sinc}(\omega_0(x-x_i))A_n(x)s[x_i]dx \\ &= \sum_i A_{n,BL}[x_i]s[x_i] \qquad \text{(B.3)}\end{aligned}$$

where $A_{n,BL}[x_i]$ represents the bandlimited version of the n^{th} aperture function.

Therefore, if either $s(x)$ or each $A_n(x)$ is bandlimited the formulation in Eq. 3.3 is obtained. Here, $\vec{s}$ represents the sinc-function samples of $s(x)$ (i.e., conventional samples of a low-pass filtered version of $s(x)$) and the rows of $\mathbf{A}$ represent sinc-function samples of the aperture functions. In general, $\vec{s}$ and $\mathbf{A}$ are infinite-dimensional.

It can be shown that $\mathbf{A}$ and $\vec{s}$ are finite dimensional if either the aperture functions or the signal are bandlimited and periodic. Suppose each $A_n(x)$ is bandlimited and periodic. Dirichlet-kernel interpolation then reconstructs the aperture functions from conventional samples. Each row of the sampling operation becomes

$$\begin{aligned}\int_{\mathcal{P}} A_n(x)s(x)dx &= \int_{\mathcal{P}} \sum_{i=1}^{\mathcal{P}} A_n[x_i]D(\omega_0(x-x_i))s(x)dx \\ &= \sum_{i=1}^{\mathcal{P}} A_n[x_i]\int_{\mathcal{P}} D(\omega_0(x-x_i))s(x)dx \\ &= \sum_{i=1}^{\mathcal{P}} A_n[x_i]s_{BL,P}[x_i] \qquad \text{(B.4)}\end{aligned}$$

where $D(\omega_0(x-x_i))$ represents the Dirichlet kernel, $s_{BL,P}[x_i]$ represents conventional samples of the bandlimited periodic version of $s(x)$, and $\mathcal{P}$ represents the fundamental period of the aperture functions. Also, if the $A_n(x)$'s can be represented as periodic but are not necessarily bandlimited but $s(x)$ is bandlimited and periodic, by symmetry a similar result is obtained with the periodic and bandlimited versions of the aperture functions.

B.2 White Gaussian Noise

Here, reconstruction estimators are derived based on ML and MAP estimation for the case of white Gaussian noise. The Fisher information matrix is obtained and it is shown that the estimates are minimum-variance unbiased estimates. Furthermore, the minimum variance unbiased estimators are the same linear estimators used in noise-free reconstruction in Section 3.3.

B.2.1 Invertible Fisher Information

First, consider the case in which the Fisher information matrix is invertible. For ML estimation the pdf in Eq. 3.13 is maximized. Note that maximizing $f(\vec{g_\nu}|\vec{g})$ is equivalent to maximizing $\log\{f(\vec{g_\nu}|\vec{g})\}$. To find the argument that maximizes the log-likelihood, the derivative is set equal to zero and the resulting system of equations is solved. Taking the derivative with respect to the i^{th} component of $\vec{s}$ produces

$$\begin{aligned}\frac{\partial \log\{f(\vec{g_\nu}|\vec{g})\}}{\partial s_i} &= \frac{\partial}{\partial s_i}\left(\frac{-M}{2}\log\{2\pi\sigma^2\} - \sum_j \frac{(g_{\nu,j} - \vec{A}_j^T\vec{s})^2}{2\sigma^2}\right)\\ &= \sum_j \frac{(g_{\nu,j} - \vec{A}_j^T\vec{s})}{\sigma^2}A_{j,i} = 0 \ \forall i = 1,\cdots,N \qquad \text{(B.5)}\end{aligned}$$

where N is the number of conventional samples. This results in the system of linear equations

$$\mathbf{A}^T\vec{g_\nu} = \mathbf{A}^T\mathbf{A}\vec{s}. \qquad \text{(B.6)}$$

Since $\mathbf{A}$ is either overdetermined or fully determined, it has full-row rank, which implies that $\mathbf{A}^T\mathbf{A}$ is a square invertible matrix. Thus, the solution to this system of equations is

$$\hat{\vec{s}} = (\mathbf{A}^T\mathbf{A})^{-1}\mathbf{A}^T\vec{g_\nu} \qquad \text{(B.7)}$$

which is the ML estimate of the conventional samples. This estimator has exactly the same form as the reconstruction operator obtained for the noise-free overdetermined case. If $\mathbf{A}$ is fully determined then it can be shown that $(\mathbf{A}^T\mathbf{A})^{-1}\mathbf{A}^T = \mathbf{A}^{-1}$, which is the linear reconstruction operator found in Section 3.3 for the noise-free fully-determined case.

Now the bias and the covariance of the estimates are evaluated. The expected value of the estimate $\hat{\vec{s}}$ is

$$\begin{aligned}E\hat{\vec{s}} &= E(\mathbf{A}^T\mathbf{A})^{-1}\mathbf{A}^T\vec{g_\nu} = (\mathbf{A}^T\mathbf{A})^{-1}\mathbf{A}^T E\vec{g_\nu}\\ &= (\mathbf{A}^T\mathbf{A})^{-1}\mathbf{A}^T\vec{g} = (\mathbf{A}^T\mathbf{A})^{-1}\mathbf{A}^T\mathbf{A}\vec{s} = \vec{s} \qquad \text{(B.8)}\end{aligned}$$

and so the estimate is unbiased. The covariance is

$$\begin{aligned}\mathbf{R}(\hat{\vec{s}}) &= E(\hat{\vec{s}} - E\hat{\vec{s}})(\hat{\vec{s}} - E\hat{\vec{s}})^T\\ &= E((\mathbf{A}^T\mathbf{A})^{-1}\mathbf{A}^T\vec{g_\nu} - \vec{s})((\mathbf{A}^T\mathbf{A})^{-1}\mathbf{A}^T\vec{g_\nu} - \vec{s})^T\\ &= E((\mathbf{A}^T\mathbf{A})^{-1}\mathbf{A}^T\vec{\nu})((\mathbf{A}^T\mathbf{A})^{-1}\mathbf{A}^T\vec{\nu})^T\\ &= (\mathbf{A}^T\mathbf{A})^{-1}\mathbf{A}^T E\vec{\nu}\vec{\nu}^T\mathbf{A}(\mathbf{A}^T\mathbf{A})^{-T}\\ &= \sigma^2(\mathbf{A}^T\mathbf{A})^{-1}\mathbf{A}^T\mathbf{A}(\mathbf{A}^T\mathbf{A})^{-T}\\ &= \sigma^2(\mathbf{A}^T\mathbf{A})^{-T}. \qquad \text{(B.9)}\end{aligned}$$

Components of the Fisher information matrix for the white Gaussian case are

$$\begin{aligned} J_{i,j}(\vec{s}) &= E\sum_{k,l} \frac{(g_{\nu,k} - \vec{A}_k^T\vec{s})}{\sigma^2} A_{k,i} \frac{(g_{\nu,l} - \vec{A}_l^T\vec{s})}{\sigma^2} A_{l,j} \\ &= \sum_k \frac{(g_{\nu,k} - \vec{A}_k^T\vec{s})^2}{\sigma^4} A_{k,i}A_{k,j} = \sum_k \frac{A_{k,i}A_{k,j}}{\sigma^2}. \end{aligned} \tag{B.10}$$

The Fisher information matrix then becomes

$$\mathbf{J}(\vec{s}) = \frac{1}{\sigma^2}\mathbf{A}^T\mathbf{A} \tag{B.11}$$

which is invertible and has the inverse $\mathbf{J}(\vec{s})^{-1} = \sigma^2(\mathbf{A}^T\mathbf{A})^{-1}$. Observe that $\mathbf{A}^T\mathbf{A}$ is symmetric (i.e., $\mathbf{A}^T\mathbf{A} = (\mathbf{A}^T\mathbf{A})^T$) and the inverse is also symmetric. Therefore,

$$\mathbf{J}(\vec{s})^{-1} = \sigma^2(\mathbf{A}^T\mathbf{A})^{-T} = \mathbf{R}(\hat{\vec{s}}) \tag{B.12}$$

implying that this estimator is a minimum-variance unbiased estimator.

B.2.2 Singular Fisher Information

Consider the case with Gaussian white noise on the aperture-filtered samples in which $\mathbf{A}$ is underdetermined. The MAP estimate with a maximum-entropy prior (zero-mean Gaussian) is

$$\begin{aligned} \hat{\vec{s}} &= \underset{\vec{s}}{\operatorname{argmax}}\{f(\vec{g}_\nu|\vec{g})f(\vec{s})\} = \underset{\vec{s}}{\operatorname{argmax}}\{\log\{f(\vec{g}_\nu|\vec{g})f(\vec{s})\}\} \\ &= \underset{\vec{s}}{\operatorname{argmax}}\left\{-\sum_j \frac{(g_{\nu,j} - \vec{A}_j^T\vec{s})^2}{2\sigma^2} - \sum_i \frac{s_i^2}{2\sigma_s^2}\right\} \end{aligned} \tag{B.13}$$

where σ_s is the variance of the Gaussian prior. Note that the constant terms ($\frac{-M}{2}\log\{2\pi\sigma^2\}$ and $\frac{-N}{2}\log\{2\pi\sigma_s^2\}$) have been dropped since they do not affect where the maxima occur. To find the maximum, the derivative with respect to each component of $\vec{s}$ is set equal to zero. This results in

$$\begin{aligned} &\frac{\partial}{\partial s_k}\left\{-\sum_j \frac{(g_{\nu,j} - \vec{A}_j^T\vec{s})^2}{2\sigma^2} - \sum_i \frac{s_i^2}{2\sigma_s^2}\right\} \\ &\quad = \sum_j \frac{(g_{\nu,j} - \vec{A}_j^T\vec{s})}{\sigma^2} A_{k,j} - \frac{s_k}{\sigma_s^2} = 0 \quad \forall k = 1, \cdots, M \end{aligned} \tag{B.14}$$

which can be written as

$$\frac{1}{\sigma^2}(\mathbf{A}^T\vec{g}_\nu - \mathbf{A}^T\mathbf{A}\vec{s}) - \frac{1}{\sigma_s^2}\vec{s} = \vec{0} \tag{B.15}$$

or

$$\mathbf{A}^T\vec{g}_\nu = \left(\mathbf{A}^T\mathbf{A} + \frac{\sigma^2}{\sigma_s^2}\mathbf{I}\right)\vec{s}. \tag{B.16}$$

As long as the ratio $\frac{-\sigma^2}{\sigma_s^2}$ is not equal to any of the eigenvalues of $\mathbf{A}^T\mathbf{A}$, $\left(\mathbf{A}^T\mathbf{A} + \frac{\sigma^2}{\sigma_s^2}\mathbf{I}\right)$ is invertible and the MAP estimate of the conventional samples is

$$\hat{\vec{s}} = \left(\mathbf{A}^T\mathbf{A} + \frac{\sigma^2}{\sigma_s^2}\mathbf{I}\right)^{-1}\mathbf{A}^T\vec{g}_\nu. \tag{B.17}$$

This corresponds to a regularization approach to the inverse of the matrix $\mathbf{A}^T\mathbf{A}$. Observe that the Moore-Penrose pseudo-inverse of $\mathbf{A}$ can be calculated by the limit

$$\mathbf{A}^\dagger = \lim_{\delta\to 0}\left(\mathbf{A}^T\mathbf{A} + \delta\mathbf{I}\right)^{-1}\mathbf{A}^T. \tag{B.18}$$

As σ_s^2 approaches infinity, the ratio $\frac{\sigma^2}{\sigma_s^2}$ approaches zero and so the maximum-entropy MAP estimate is provided by the Moore-Penrose pseudo-inverse. This is exactly the reconstruction operation obtained for the underdetermined system in Section 3.3.

Although the Moore-Penrose pseudo-inverse is not generally a minimum-variance unbiased estimator over the entire domain of $\mathbf{A}$, it is a minimum-variance unbiased estimator over the range space of $\mathbf{A}^\dagger$. In order to show this, we need a lower bound on the covariance. Since the Fisher information is singular, we cannot apply the Cramer-Rao bound directly and must find a lower bound another way. An estimator over any subspace can be obtained by finding a signal model that spans the subspace, estimating the model parameters, and then projecting the model parameter estimates back through the model to estimate the signal. The Cramer-Rao bound on the estimates of the model parameters may be obtained and then scaled by the sensitivity of the model to obtain a lower bound on the estimates of the signals over the subspace. More precisely the model $\vec{s} = \mathbf{A}^\dagger\vec{a}$ is applied where $\vec{a}$ are the model parameters. This results in the Fisher information matrix for estimating the model parameters

$$\mathbf{J}(\vec{a}) = \frac{1}{\sigma^2}\mathbf{I}. \tag{B.19}$$

The sensitivity of the model is

$$\frac{\partial}{\partial\vec{a}}\mathbf{A}^\dagger\vec{a} = \mathbf{A}^\dagger \tag{B.20}$$

resulting in the lower bound

$$\mathbf{R}(\hat{\vec{s}}) \geq \left(\frac{\partial}{\partial\vec{a}}\mathbf{A}^\dagger\vec{a}\right)\mathbf{J}(\vec{a})^{-1}\left(\frac{\partial}{\partial\vec{a}}\mathbf{A}^\dagger\vec{a}\right)^T = \sigma^2\mathbf{A}^\dagger\mathbf{A}^{\dagger T}. \tag{B.21}$$

Now the bias and covariance of the MAP estimator over the range space of $\mathbf{A}^\dagger$ are obtained. The expected value of the estimate is

$$E(\hat{\vec{s}}) = E(\mathbf{A}^\dagger\vec{g}_\nu) = \mathbf{A}^\dagger\vec{g} = \mathbf{A}^\dagger\mathbf{A}\vec{s} \tag{B.22}$$

and if $\vec{s} = \mathbf{A}^\dagger \vec{a}$ then

$$E(\hat{\vec{s}}) = \mathbf{A}^\dagger \mathbf{A} \mathbf{A}^\dagger \vec{a} = \mathbf{A}^\dagger \vec{a} = \vec{s}. \tag{B.23}$$

Thus, the MAP estimator for white Gaussian noise is unbiased over the range space of $\mathbf{A}^\dagger$. The covariance of the MAP estimator over the range space of $\mathbf{A}^\dagger$ is

$$\begin{aligned} \mathbf{R}(\hat{\vec{s}}) &= E(\vec{s} - \mathbf{A}^\dagger \vec{g})(\vec{s} - \mathbf{A}^\dagger \vec{g})^T \\ &= E(\mathbf{A}^\dagger \vec{g}_\nu)(\mathbf{A}^\dagger \vec{g}_\nu)^T - \vec{s}\vec{s}^T \\ &= \mathbf{A}^\dagger (\vec{g}\vec{g}^T + \sigma^2 \mathbf{I} - \vec{a}\vec{a}^T) \mathbf{A}^{\dagger T} \\ &= \mathbf{A}^\dagger (\mathbf{A}\mathbf{A}^\dagger \vec{a}\vec{a}^T (\mathbf{A}\mathbf{A}^\dagger)^T + \sigma^2 \mathbf{I} - \vec{a}\vec{a}^T) \mathbf{A}^{\dagger T} \\ &= \sigma^2 \mathbf{A}^\dagger \mathbf{A}^{\dagger T}. \end{aligned} \tag{B.24}$$

Thus, the covariance achieves the lower bound and so the MAP estimator is a minimum-variance unbiased estimator over the range space of $\mathbf{A}^\dagger$ for white Gaussian noise.

B.3 Scatterometer ML Estimator

Here, the ML scatterometer reconstruction estimator is obtained assuming that the sampling matrix is not underdetermined. It is also shown that an analytic form for the estimator may be obtained, although the expression is rather complicated and multiple solutions (local maxima) are possible.

The ML estimator for the scatterometer noise model searches for the conventional samples $\vec{s}$ that maximize the log-likelihood function

$$L_{ML} = -\sum_i \left[\frac{(g_{\nu,i} - \vec{A}_i^T \vec{s})^2}{2R_{i,i}} + 1/2 \log\{2\pi R_{i,i}\} \right]. \tag{B.25}$$

The local maxima is obtained by setting the gradient to zero and solving the resulting system of equations. The partial derivative of L_{ML} with respect to the j^{th} component of $\vec{s}$ is

$$\begin{aligned} \frac{\partial L_{ML}}{\partial s_j} &= \sum_i \frac{-A_{i,j}}{R_{i,i}} \left[-g_{\nu,i} + \vec{A}_i^T \vec{s} + \alpha_i \vec{A}_i^T \vec{s} + \beta_i/2 - \frac{(g_{\nu,i} - \vec{A}_i^T \vec{s})^2 (\alpha_i \vec{A}_i^T \vec{s} + \beta_i/2)}{R_{i,i}} \right] \\ &= \vec{A}_j^T \vec{K}(\vec{s}). \end{aligned} \tag{B.26}$$

Taking the partial derivatives with respect to each component and setting them equal to zero produces the system

$$\mathbf{A}^T \vec{K}(\vec{s}) = \vec{0} \tag{B.27}$$

which implies that $\vec{K}(\vec{s}) = \vec{0}$ or that $\vec{K}(\vec{s})$ is in the null space of $\mathbf{A}^T$. If $\mathbf{A}$ is fully determined or overdetermined, there is no null space and the only solutions are when $\vec{K}(\vec{s}) = \vec{0}$. If each element of $\vec{K}(\vec{s})$ is set to zero, cubic equations in $\vec{A}_i^T \vec{s}$ are obtained for each i that have at least one and up to three real roots. Each of these roots can be solved analytically via the cubic equation. The solutions to the entire system of equations result in a linear system in $\vec{s}$. That is, if $\vec{z}$ is a solution to the cubic system of equations $\vec{K}(\vec{s}) = \vec{0}$, then $\vec{A}_i^T \vec{s} = z_i$ for each i and the linear system $\mathbf{A}\vec{s} = \vec{z}$ is obtained. If $\mathbf{A}$ is fully determined, then $\hat{\vec{s}} = \mathbf{A}^{-1}\vec{z}$, and if it is overdetermined, then $\hat{\vec{s}} = (\mathbf{A}^T\mathbf{A})^{-1}\mathbf{A}^T\vec{z}$.

Note that there are potentially N^3 local maxima of L_{ML} where N is the number of conventional samples, although in practice there tend to be fewer local maxima. The N^3 local maxima correspond to every combination of the three roots of the cubic equations. To find the ML estimate, all of the local maxima must be found and checked to see which one has the highest maxima. This is too cumbersome for a practical implementation and so a simple gradient search is used to find a local maxima near an initial guess.

Appendix C

Appendix to Chapter 7

This appendix considers several issues involved in the scatterometer wind field reconstruction approach developed in Chapter 7. First, noise-free reconstruction of the continuous forward operator is discussed. The relationship between the wave number spectra of the wind and the associated σ^0 fields is then addressed. Next, noise-free wind field reconstruction of the discrete forward operator is considered. An approach to deal with Geophysical noise is presented. The gradient of the MAP objective function is derived. Finally, an approach to obtain a lower bound on the estimates of the MAP reconstruction estimator is developed.

C.1 Inversion of the Continuous Noise-free Forward Operator

In theory, the continuous sampling operation can be inverted using constrained optimization. That is, we define a metric $d(\vec{U}(x), \vec{z}(x))$ over the wind field domain to optimize subject to a consistent forward sampling operation $\vec{\sigma}_t^0 = \mathcal{T}(\vec{U}(x))$. To find the optima, the Lagrangian

$$L = d(\vec{U}(x), \vec{z}(x)) + \vec{\lambda}^T(\vec{\sigma}_t^0 - \mathcal{T}(\vec{U}(x))) \tag{C.1}$$

is used. The gradient with respect to the wind field and $\vec{\lambda}$ are set to zero to find the critical points. Depending on the metric and the sampling geometry, a second derivative test may be required to distinguish maxima from minima. For a given set of noise-free measurements $\vec{\sigma}_t^0$, solutions to these equations and inequality constraints represent wind fields that are consistent with the forward operator that optimize the metric. As a function of $\vec{\sigma}_t^0$, the set of equations and inequalities define a finite-dimensional manifold in the wind domain representing all consistent solutions that optimize the metric. This manifold defines the class of signals that can be reconstructed under the metric. A different metric may result in a different class of reconstructible signals. In principle, the manifold may be parameterized, producing a wind field model with finitely many parameters that can be estimated from the σ^0 measurements.

Note that although this approach allows the reconstructible wind field signals to be represented with a finite number of parameters, because of the nonlinearity the manifold cannot in general be contained within the span of a finite linear basis. Since bandlimited spaces are finite linear subspaces, the class of reconstructible wind fields is generally not bandlimited. Even if all the aperture functions are bandlimited, they may not impose a bandlimit on the wind fields (nor the σ^0 fields because they must be consistent with the wind field). Therefore, it may be possible to obtain wind estimates (and corresponding σ^0 field estimates) with higher frequency content than the band limit of the aperture functions.

C.2 Relationship Between Spectra of Wind and σ^0 Fields

This section presents the relationship between the wave-number spectrum (Fourier transform) of the spatially continuous σ^0 fields for each measurement and the wave-number spectrum of the components of the wind field. First, a theorem and proof for the relationship between the spectrum of the σ^0 fields and the spectrum of the components of the wind/rain field are stated. Then some practical considerations for the relationship of the bandlimit of the σ^0 fields and the bandlimit of the wind fields are presented.

Theorem: For the nonlinear operator $\mathcal{T}$ defined in Eq. 3.2 with a GMF that can be represented by a finite power series (where N_1 and N_2 are the order of the wind vector components), we have:

(1) The Fourier transform of the i^{th} σ^0 field $\sigma_i(x) = gmf(\vec{U}(x), \theta_i(x), \psi_i(x))$ is related to the Fourier transform of the components of wind field $U_1(x)$ and $U_2(x)$ by

$$\mathcal{F}\{\sigma_i(x)\} = \sum_{n_1,n_2=0}^{N_1,N_2} \mathcal{F}\{a_{i,n_1,n_2}(x)\} * \left[\mathop{*}_{k=1}^{2} \left[\mathop{*}_{j=1}^{n_k} \mathcal{F}\{U_k(x)\} - \mathcal{F}\{c_k\} \right]\right] \tag{C.2}$$

where $\mathcal{F}$ represents the Fourier transform, $a_{i,n_1,n_2}(x)$ is the power series coefficient corresponding to $U_1(x)$ and $U_2(x)$, c_k represents a reference wind field component that is constant in x, and $*_{j=1}^{n}$ represents n nested convolutions.

(2) If the wind field components are bandlimited by ω_{U_1} and ω_{U_2}, and the power series coefficients are bandlimited by ω_a, then the σ^0 field components are bandlimited by

$$\omega_\sigma \leq N_1\omega_{U_1} + N_2\omega_{U_2} + \omega_a. \tag{C.3}$$

Proof: Showing part (1) is straight forward. The power series expansion of $\sigma_i = \text{gmf}(\vec{U}(x), \theta_i(x), \psi_i(x))$ is

$$\sigma_i(x) = \sum_{n_1,n_2=0}^{N_1,N_2} a_{i,n_1,n_2}(x) \prod_{k=1}^{2} (U_k(x) - c_k)^{n_k}. \tag{C.4}$$

Taking the Fourier transform produces

$$\begin{aligned} \mathcal{F}\{\sigma_i(x)\} &= \mathcal{F}\left\{ \sum_{n_1,n_2=0}^{N_1,N_2} a_{i,n_1,n_2}(x) \prod_{k=1}^{2} (U_k(x) - c_k)^{n_k} \right\} \\ &= \sum_{n_1,n_2=0}^{N_1,N_2} \mathcal{F}\{a_{i,n_1,n_2}(x)\} * \mathcal{F}\{\prod_{k=1}^{2}\prod_{j=1}^{n_k} (U_k(x) - c_k)\} \\ &= \sum_{n_1,n_2=0}^{N_1,N_2} \mathcal{F}\{a_{i,n_1,n_2}(x)\} * \left[\mathop{*}_{k=1}^{2} \left[\mathop{*}_{j=1}^{n_k} (\mathcal{F}\{U_k(x)\} - \mathcal{F}\{c_k\}) \right]\right] \end{aligned} \tag{C.5}$$

which is Eq. C.2.

To show part (2), we start with bandlimited wind field components with bandlimits ω_{U_k} for each component k. Note that since c_k is a constant for each k, $\mathcal{F}\{c_k\}$ is a delta function centered at zero. The term

$$\left[\overset{n_k}{\underset{j=1}{*}}(\mathcal{F}\{U_k(x)\} - \mathcal{F}\{c_k\})\right] \tag{C.6}$$

represents the convolution of the k^{th} wind field component with itself n_k times with the DC term modified. Each autoconvolution expands the spectrum by ω_{U_k} so the term above has a bandlimit of $n_1\omega_{U_1}$ for $k = 1$. This term is then convolved with the autoconvolution of the other wind field component (i.e., $k = 2$), which has a bandlimit of $n_2\omega_{U_2}$, producing a bandlimit of $n_1\omega_{U_1} + n_2\omega_{U_2}$. This quantity is then convolved with $\mathcal{F}\{a_{i,n_1,n_2}(x)\}$, resulting in a band limit of $n_1\omega_{U_1} + n_2\omega_{U_2} + \omega_a$. Then each combination of n_1 and n_2 is added together. The resulting bandlimit is the highest bandlimit of any of the terms in the sum, which corresponds to the term where $n_1 = N_1$ and $n_2 = N_2$, resulting in the bandlimit $N_1\omega_{U_1} + N_2\omega_{U_2} + \omega_a$. In case some high frequency content of the different terms in the sum cancel out portions of the spectrum, an inequality relation is obtained. Thus,

$$\omega_\sigma \leq N_1\omega_{U_1} + N_2\omega_{U_2} + \omega_a. \tag{C.7}$$

■

Note that $a_{i,n_1,n_2}(x)$ is a function of x because the look geometry changes in x. If the aperture functions are sufficiently narrow such that variation of the look geometry is negligible over the main lobe, then $a_{i,n_1,n_2}(x)$ can be approximated as constant in x and the result in part (2) of the theorem reduces to

$$\omega_\sigma \leq N_1\omega_{U_2} + N_2\omega_{U_2}. \tag{C.8}$$

The relationship between the bandlimit of the σ^0 fields and the bandlimit of the wind field components suggests that an up-sampled version of the wind field should be projected through the sampling operator when calculating the forward projection. Although the actual bandlimit of the σ^0 fields can be as high as the result in part (2) of the theorem, it may be possible to assume that the σ^0 bandlimit is similar to the bandlimit of the wind components without introducing significant errors. This is because the autoconvolutions in Eq. C.2 tend to produce spectra with relatively low energy at high frequencies. To illustrate this, consider the one-dimensional case. The magnitude of the autoconvolution of a bandlimited signal is less than autoconvolution of the magnitude. That is,

$$\begin{aligned} |X(\omega) * X(\omega)| &= |\int X(\tau)X(\tau-\omega)d\tau| \\ &\leq \int |X(\tau)||X(\tau-\omega)|d\tau = |X(\omega)| * |X(\omega)|. \end{aligned} \tag{C.9}$$

Also, note that $|X(\omega)| \leq \alpha B(\omega)$ for some α and for every ω, where $B(\omega)$ is a boxcar function centered at zero. Thus,

$$\begin{aligned} |X(\omega) * X(\omega)| &\leq (\alpha B(\omega)) * |X(\omega)| \\ &\leq (\alpha B(\omega)) * (\alpha B(\omega)) = \alpha^2 (B(\omega) * B(\omega)). \end{aligned} \tag{C.10}$$

Extending this to multiple nested convolutions we have

$$|\mathop{*}_{j=1}^{n} X(\omega)| \leq \alpha^n \mathop{*}_{j=1}^{n} B(\omega). \tag{C.11}$$

Now, consider the autoconvolution of the boxcar function. Each increasing n extends the tail into higher frequencies, but the higher frequencies have lower values than lower frequencies.

C.3 Noise-free Wind Field Reconstruction

In the noise-free case, reconstruction is accomplished by inverting the discrete sampling operation (i.e., by estimating the uniformly spaced samples of the wind vector field $\vec{U}[x']$). Although in practice scatterometer measurements are noisy, considering the noise-free case gives insight into the nature of the problem. This section of the appendix considers noise-free reconstruction of the uniform samples of the wind field $\vec{U}[x']$.

Note that the sampling operation in Eq. 7.5 represents a system of nonlinear equations with N equations and M unknowns where N is the number of σ^0 measurements and M is the number of samples required to represent the wind field with the assumed bandlimit. Since the bandlimit is not explicitly set by the aperture functions, a high enough bandlimit may be assumed such that the system of equations in 7.5 is underdetermined for any sampling scheme (i.e., a high bandlimit may be chosen so that $M > N$). Thus, the scatterometer wind inversion problem is generally ill-posed meaning that more parameters than data points are to be estimated. For the noisy case, this translates into having unobservable parameters (i.e., a singular Fisher information matrix).

The underdetermined operator $\mathbf{T}$ cannot be inverted without imposing additional structure on the signal. Structure may be imposed by employing a field-wise model or additional constraints.

Model based methods assume that the wind field is in the span of a field-wise model. A low-order model is chosen so that an inverse mapping from the measurements to the model parameters may be obtained that is fully or overdetermined. The model parameters can then be estimated and the wind field recovered by projecting the model parameter estimates through the model.

Constrained optimization is a more general way to regularize the problem. This is the approach taken in the continuous case in Section C.1. Constrained optimization for the discrete case can be expressed as

optimize $d(\vec{U}[x'], \vec{z}[x'])$,

subject to $\vec{\sigma}_t^0 = \mathbf{T}(\mathbf{H}\vec{U}[x'])$

where $d(\vec{U}[x'], \vec{z}[x'])$ is a metric in the discrete wind domain. The optima can be found by obtaining the Lagrangian $L(\vec{U}[x']) = d(\vec{U}[x'], \vec{z}[x']) + \vec{\lambda}^T(\vec{\sigma}_t^0 = \mathbf{T}(\mathbf{H}\vec{U}[x']))$, setting the gradient to zero, and solving the resulting nonlinear system of equations. If the metric is chosen appropriately, this approach results in a fully determined system of equations that may have multiple solutions. If there are multiple global minima, then these represent field-wise ambiguities and cannot be distinguished. In the noisy case, the possibility of multiple solutions contributes to the unidentifiability (or more precisely the set-wise identifiability) of the scatterometer problem.

C.3.1 Observability

In wind field reconstruction from σ^0 measurements the parameters to estimate are the uniformly spaced conventional samples of the wind vector field. These parameters are observable if the Fisher information matrix is invertible. By observable, we mean that the parameters can be estimated with finite precision from the σ^0 measurements alone.

Recall that the noise-free forward operation is generally underdetermined. When including the scatterometer noise model, a singular Fisher information matrix results. Thus, the wind fields are generally unobservable for scatterometer sampling schemes. Scatterometer wind field estimation is ill-posed, and in order to estimate the wind field, some structure must be imposed on the signal. As noted, this can be done directly by imposing a signal model, or by applying some additional constraints from other data or prior knowledge of the signal structure. In Chapter 7 a Bayesian approach is employed, which uses a prior distribution to regularize the problem.

C.3.2 Identifiability

The nonlinearity of the GMF introduces the possibility of multiple solutions, which is related to identifiability. Identifiability has to do with the number of solutions to the inverse problem. For example, in the noise-free case, the parameters are identifiable if there is a single element in the inverse image for every accessible set of noise-free σ^0 measurements. By accessible noise-free σ^0 measurements, we mean any $\vec{\sigma}^0_t$ in the range space of $\mathbf{T}(\cdot)$. If there are a finite or countable number of elements in the inverse image, the inverse problem is said to be set-wise identifiable. If there are infinitely (uncountable) many solutions, the system is considered to be unidentifiable.

In the noisy case, identifiability can be thought of as having to do with the number of near consistent solutions. That is, the inverse image is always the entire domain of the sampling operator; however, some portions of the domain are more likely to produce the observed σ^0 measurements than others. Identifiability in the noisy case has to do with the number of local maxima of the likelihood function $f(\vec{\sigma}^0_m|\vec{\sigma}^0_t)$. For wind scatterometry, if the forward sampling operation is underdetermined, then there are an uncountably infinite number of wind fields that are equally most-likely to produce the same measurements. In general, wind scatterometry is unidentifiable. However, the MAP estimation approach proposed in Chapter 7 to make the parameters observable also makes the parameters set-wise identifiable for wind scatterometry. That is, if the prior is chosen appropriately, MAP estimation regularizes the problem to make each local maximum of the posterior distribution have exactly one equally probable element. The different local maxima represent field-wise ambiguities. The MAP likelihood values of the different local maxima may have different values providing some skill in discriminating between them.

The sources of field-wise ambiguities derive from three factors: 1) the point-wise nonlinearity introduced by the GMF, 2) the underdetermined sampling operator, and 3) the fact that the likelihood function may be multimodal as a function of true σ^0 fields since the variance is a function of the true σ^0.

C.4 Noisy GMF

The GMF can be modeled as a random variable by adding a zero-mean random variable to the deterministic mapping

$$\sigma_i[x] = \mathrm{gmf}(\vec{U}[x], \theta_i[x], \psi_i[x]) + \nu_{gmf,i}[x] \tag{C.12}$$

where $\sigma_i[x]$ is the discrete σ^0 field associated with the i^{th} σ^0 measurement, and each component of $\nu_{gmf,i}[x]$ is a zero-mean random variable. Note that the sampling operation can be expressed as

$$\mathbf{T}(\mathbf{H}\vec{U}[x']) = \mathbf{T}(\vec{U}[x]) = \mathbf{A}(\vec{\sigma}[x]) \tag{C.13}$$

where $\vec{\sigma}[x]$ is the vector of $\sigma_i[x]$s, and $\mathbf{A}$ is the operator defined as

$$\mathbf{A}(\vec{\sigma}[x]) = \left[\begin{array}{c} \sum_x A_1[x]\sigma_1[x] \\ \vdots \\ \sum_x A_N[x]\sigma_N[x] \end{array} \right]. \tag{C.14}$$

Because the rows of $\mathbf{A}$ are linear, the modified noise model becomes

$$\begin{aligned} \vec{\sigma}^0_m &= \vec{\sigma}^0_t + \mathbf{A}(\vec{\nu}_{gmf}[x]) + \vec{\nu} \\ &= \vec{\sigma}^0_t + \tilde{\vec{\nu}} \end{aligned} \tag{C.15}$$

where each component of $\tilde{\vec{\nu}}$ is a zero-mean random variable.

C.5 Gradient of MAP Objective Function

The gradient of the MAP objective function is required for practical implementation of the MAP wind reconstruction method. Here, the gradient of the MAP objective function is derived.

The MAP objective function is the sum of the log-likelihood function $\log f(\vec{\sigma^0_m}|\vec{\sigma^0_t})$ (or equivalently $\log f(\vec{\sigma^0_m}|\vec{U}[x])$) and the log of the prior $\log f(\vec{U}[x])$. For the scatterometer noise model used in this paper, the partial of the log-likelihood function with respect to the

i^{th} wind vector component at location x is

$$\begin{aligned}
&\frac{\partial \log f(\vec{\sigma}^0_m|\vec{U}[x'])}{\partial U_i[x]} \\
&= \frac{\partial}{\partial U_i[x]} \sum_n \frac{-(\sigma^0_{m,n} - T_n(\mathbf{H}\vec{U}[x']))^2}{2R_{n,n}} + \frac{\partial}{\partial U_i[x]} \log\{(2\pi)^{N/2} \prod_n R_{n,n}\} \\
&= -\sum_n \frac{\partial}{\partial U_i[x]} \left[\frac{(\sigma^0_{m,n} - T_n(\mathbf{H}\vec{U}[x']))^2}{2R_{n,n}} + \frac{1}{2}(\log\{2\pi\} + \log\{R_{n,n}\}) \right].
\end{aligned} \tag{C.16}$$

The first term in the sum is

$$\begin{aligned}
&\frac{\partial}{\partial U_i[x]} \left[\frac{(\sigma^0_{m,n} - T_n(\mathbf{H}\vec{U}[x']))^2}{2R_{n,n}} \right] \\
&= \frac{2(\sigma^0_{m,n} - T_n(\mathbf{H}\vec{U}[x'])(-\sum_y A_n[y] \frac{\partial \mathrm{gmf}_n(\mathbf{H}\vec{U}[x'])}{\partial U_i[x]})}{4R^2_{n,n}} - \frac{(\sigma^0_{m,n} - T_n(\mathbf{H}\vec{U}[x']))^2}{4R^2_{n,n}} \frac{\partial 2R_{n,n}}{\partial U_i[x]} \\
&= -\frac{(\sigma^0_{m,n} - T_n(\mathbf{H}\vec{U}[x'])A_n[x] \frac{\partial \mathrm{gmf}_n(\vec{U}[x])}{\partial U_i[x]})}{R_{n,n}} - \frac{(\sigma^0_{m,n} - T_n(\mathbf{H}\vec{U}[x']))^2}{2R^2_{n,n}} \frac{\partial R_{n,n}}{\partial U_i[x]}
\end{aligned} \tag{C.17}$$

where $T_n = \sum_y A_n[y]\mathrm{gmf}_n(\mathbf{H}\vec{U}[x'])$. The second term in the sum in Eq. C.16 is

$$\frac{\partial}{\partial U_i[x]} \frac{1}{2} \left[\log\{2\pi\} + \log\{R_{n,n}\}\right] = \frac{1}{2R_{n,n}} \frac{\partial R_{n,n}}{\partial U_i[x]}. \tag{C.18}$$

Note that the partial derivative of $R_{n,n}$ is

$$\frac{\partial R_{n,n}}{\partial U_i[x]} = (2\alpha_n T_n(\mathbf{H}\vec{U}[x']) + \beta_n) A_n[x] \frac{\partial \mathrm{gmf}_n(\vec{U}[x])}{\partial U_i[x]}. \tag{C.19}$$

Thus,

$$\begin{aligned}
\frac{\partial \log f(\vec{\sigma}^0_m|\vec{U}[x'])}{\partial U_i[x]} &= \sum_n \left[\frac{(\sigma^0_{m,n} - T_n(\mathbf{H}\vec{U}[x']) - (\alpha_n T_n(\mathbf{H}\vec{U}[x']) + \beta_n/2)}{R_{n,n}} \right. \\
&\qquad \left. + \frac{(\sigma^0_{m,n} - T_n(\mathbf{H}\vec{U}[x'])^2 (\alpha_n T_n(\mathbf{H}\vec{U}[x']) + \beta_n/2)}{R^2_{n,n}} \right] A_n[x] \frac{\partial \mathrm{gmf}_n(\vec{U}[x])}{\partial U_i[x]} \\
&= \sum_n -K_n A_n[x] \frac{\partial \mathrm{gmf}_n(\vec{U}[x])}{\partial U_i[x]}
\end{aligned} \tag{C.20}$$

where

$$\begin{aligned} K_n \;&=\; \left[\frac{(\sigma^0_{m,n} - T_n(\mathbf{H}\vec{U}[x']) - (\alpha_n T_n(\mathbf{H}\vec{U}[x']) + \beta_n/2)}{R_{n,n}} \right. \\ &\qquad \left. + \frac{(\sigma^0_{m,n} - T_n(\mathbf{H}\vec{U}[x'])^2(\alpha_n T_n(\mathbf{H}\vec{U}[x']) + \beta_n/2)}{R^2_{n,n}} \right]. \end{aligned} \tag{C.21}$$

The gradient of the log of the prior expressed in Eq. 7.11 and Eq. 7.12 is

$$\frac{\partial \log f(\vec{U}[x'])}{\partial U_i[x]} \;=\; \sum_n \frac{-1}{p}(\sigma^0_n - \mathrm{gmf}_n(\vec{U}[x]))\frac{\partial \mathrm{gmf}_n(\vec{U}[x])}{\partial U_i[x]}. \tag{C.22}$$

Adding this expression to Eq. C.20 results in the gradient of the MAP objective function.

C.6 Fisher Information and Cramer-Rao Bound for Estimating the Wind Field Using the σ^0 Measurements and a Gaussian Maximum-Entropy Prior

Recall that the Fisher information matrix for the scatterometer wind field estimation problem is generally singular. This makes it difficult to evaluate the quality of the estimates using the Cramer-Rao bound. This section considers an extension of the Cramer-Rao bound that is appropriate for a MAP estimator.

Note that using a prior to perform MAP estimation is mathematically equivalent to (although philosophically different from) ML estimation with additional statistically independent data whose noise distribution is the prior. The Fisher information corresponding to the MAP estimator can be obtained in a similar manner as the Fisher information corresponding the ML estimator. A Cramer-Rao bound for any unbiased estimator that uses the original data and the additional data (or equivalently the prior) can be obtained.

To illustrate that the MAP estimator is equivalent to a ML estimator with additional data, suppose that we have additional independent noisy measurements of the wind field components, $\vec{U}_m[x']$, along with the original noisy aperture-filtered σ^0 measurements, $\vec{\sigma}^0_m$. The joint distribution of all the measurements given the noise-free wind component measurements $\vec{U}[x']$ is $f(\vec{\sigma}^0_m, \vec{U}_m[x'] | \vec{U}[x'])$. Since $\vec{\sigma}^0_m$ and $\vec{U}_m[x']$ are statistically independent they are conditionally independent and so $f(\vec{\sigma}^0_m, \vec{U}_m[x'] | \vec{U}[x']) = f(\vec{\sigma}^0_m | \vec{U}[x']) f(\vec{U}_m[x'] | \vec{U}[x'])$. This is exactly the form of the MAP estimator if $f(\vec{U}_m[x'] | \vec{U}[x'])$ the same form as the prior distribution $f(\vec{U}[x'])$ defined above.

The elements of the Fisher information matrix for estimating the wind vector samples from the noisy σ^0 measurements and the additional noisy wind vector samples are

$$\begin{aligned}
& J^{joint}_{i,j,x,y}(\vec{U}[x']) \\
={}& E\left(\tfrac{\partial}{\partial U_i[x]}\log\{f(\vec{\sigma}^0_m|\vec{U}[x'])f(\vec{U}_m[x']|\vec{U}[x'])\}\right)\left(\tfrac{\partial}{\partial U_j[y]}\log\{f(\vec{\sigma}^0_m|\vec{U}[x'])f(\vec{U}_m[x']|\vec{U}[x'])\}\right) \\
={}& E\left(\tfrac{\partial}{\partial U_i[x]}\log\{f(\vec{\sigma}^0_m|\vec{U}[x'])\}\right)\left(\tfrac{\partial}{\partial U_j[y]}\log\{f(\vec{\sigma}^0_m|\vec{U}[x'])\}\right) \\
&+E\left(\tfrac{\partial}{\partial U_i[x]}\log\{f(\vec{U}_m[x']|\vec{U}[x'])\}\right)\left(\tfrac{\partial}{\partial U_j[y]}\log\{f(\vec{U}_m[x']|\vec{U}[x'])\}\right) \\
&+E\left(\tfrac{\partial}{\partial U_i[x]}\log\{f(\vec{\sigma}^0_m|\vec{U}[x'])\}\right)\left(\tfrac{\partial}{\partial U_j[y]}\log\{f(\vec{U}_m[x']|\vec{U}[x'])\}\right) \\
&+E\left(\tfrac{\partial}{\partial U_i[x]}\log\{f(\vec{U}_m[x']|\vec{U}[x'])\}\right)\left(\tfrac{\partial}{\partial U_j[y]}\log\{f(\vec{\sigma}^0_m|\vec{U}[x'])\}\right) \\
={}& J^{ML}_{i,j,x,y}(\vec{U}[x']) + J^{Prior}_{i,j,x,y}(\vec{U}[x']) \\
&+E\left(\tfrac{\partial}{\partial U_i[x]}\log\{f(\vec{\sigma}^0_m|\vec{U}[x'])\}\right)E\left(\tfrac{\partial}{\partial U_j[y]}\log\{f(\vec{U}_m[x']|\vec{U}[x'])\}\right) \\
&+E\left(\tfrac{\partial}{\partial U_i[x]}\log\{f(\vec{U}_m[x']|\vec{U}[x'])\}\right)E\left(\tfrac{\partial}{\partial U_j[y]}\log\{f(\vec{\sigma}^0_m|\vec{U}[x'])\}\right) \\
={}& J^{ML}_{i,j,x,y}(\vec{U}[x']) + J^{Prior}_{i,j,x,y}(\vec{U}[x'])
\end{aligned} \tag{C.23}$$

where $J^{ML}_{i,j,x,y}(\vec{U}[x'])$ is the $\{i,j,x,y\}^{th}$ element of the Fisher information for estimating the wind field samples from the σ^0 measurements, and $J^{Prior}_{i,j,x,y}(\vec{U}[x'])$ is the $\{i,j,x,y\}^{th}$ element of the Fisher information for estimating wind field samples from the additional samples. The third and fourth terms in the expression are zero since the σ^0 measurements and the additional wind component measurements are independent and the expected value of the gradient of any differentiable log-likelihood function is zero [35]. The corresponding Fisher information matrix using any wind prior that is statistically independent of the σ^0 measurements can be written as

$$\mathbf{J}^{joint}(\vec{U}[x']) = \mathbf{J}^{ML}(\vec{U}[x']) + \mathbf{J}^{Prior}(\vec{U}[x']). \tag{C.24}$$

Now consider the case with a zero-mean Gaussian prior with an arbitrarily large variance (i.e., the Gaussian maximum entropy zero-mean prior). For this case, MAP estimation is equivalent to having additional statistically independent samples of the wind field components that are all zero (i.e., $\vec{U}_m[x'] = \vec{0}$) but whose variance is arbitrarily large. For this Gaussian case the Fisher information is the inverse of the covariance matrix (i.e., $\mathbf{J}^{Prior}(\vec{U}[x']) = \frac{1}{p}\mathbf{I}$). This results in the joint Fisher information for using the σ^0 measurements and the additional noisy samples of the wind field

$$\mathbf{J}^{joint}(\vec{U}[x']) \;=\; \mathbf{J}^{ML}(\vec{U}[x']) + \frac{1}{p}\mathbf{I} \tag{C.25}$$

and the Cramer-Rao bound becomes

$$\mathbf{R}(\hat{\vec{U}}[x']) \;\geq\; \left(\mathbf{J}^{ML}(\vec{U}[x']) + \frac{1}{p}\mathbf{I}\right)^{-1}. \tag{C.26}$$

Note that if we let p get arbitrarily large, the bound becomes

$$\mathbf{R}(\vec{U}[x']) \quad \geq \quad \mathbf{J}^{ML}(\vec{U}[x'])^{\dagger} \tag{C.27}$$

where $\mathbf{J}^{ML}(\vec{U}[x'])^{\dagger}$ is the Moore-Penrose pseudo-inverse of $\mathbf{J}^{ML}(\vec{U}[x'])$. Therefore, the pseudo-inverse of the ML Fisher information provides a lower bound on any unbiased estimator of the wind field samples from the σ^0 measurements and the additional wind field samples composed of the mean of the maximum-entropy prior.

Although there may be theoretical issues in assuming the Fisher information and Cramer-Rao bound obtained here can be applied to the MAP estimation problem, doing so can provide valuable insight into the problem and may result in practical design tools. Thus, we define the Fisher information matrix corresponding to the MAP estimation problem as

$$\mathbf{J}^{MAP}(\vec{U}[x']) = \mathbf{J}^{joint}(\vec{U}[x']) = \mathbf{J}^{ML}(\vec{U}[x']) + \mathbf{J}^{Prior}(\vec{U}[x']) \tag{C.28}$$

which is a regularized version of the standard Fisher information matrix.

Note that this result applies to both the σ^0 imaging problem and the wind estimation problem. The result yields a bound on the variability of an unbiased estimator that uses the data and a particular prior. However, with the scatterometer noise model, both the MAP σ^0 image reconstruction estimator and the MAP wind field reconstruction estimator are generally biased estimators. A biased Cramer-Rao bound may be obtained using the gradient of the bias [30]. However, it is difficult to find an analytic form for the gradient of the bias and so a numerical methods may be applied. Monte-Carlo methods are useful to obtain the bias and gradient of the bias of a MAP estimator, which can be used to come up with a bound. However, Monte-Carlo simulation can be applied to simultaneously estimate the variability of the estimates and the bias, making a bound unnecessary. Nevertheless, the unbiased bound allows us to compare the results of a biased estimator to the lowest variability of any unbiased estimator.

In the following we provide the prior Fisher information matrix $\mathbf{J}^{Prior}(\vec{U}[x'])$ for the various priors applied in the σ^0 imaging and wind estimation problems. First, consider the exponential prior for the MAP σ^0 imaging problem (i.e., $f(s[x']) = \prod_{x'} \lambda \exp\{\lambda s[x']\}$ where $s[x']$ is the σ^0 image). The components of the corresponding prior Fisher information matrix can be expressed as

$$\begin{aligned} J^{Prior}_{x,y}(s[x']) &= E\left(\frac{\partial}{\partial s[x]}\log\{f(s[x'])\}\right)\left(\frac{\partial}{\partial s[y]}\log\{f(s[x'])\}\right) \\ &= E\left(-\lambda\frac{\partial s[x']}{\partial s[x]}\right)\left(-\lambda\frac{\partial s[x']}{\partial s[y]}\right) = \lambda^2\delta(x-x')\delta(y-x') \end{aligned} \tag{C.29}$$

where $\delta(x-x')$ and $\delta(y-x')$ are delta functions. This results in the Fisher information matrix

$$\mathbf{J}^{Prior}(s[x']) = \lambda^2\mathbf{I}. \tag{C.30}$$

If the log-normal prior is used for σ^0 image reconstruction described in Eq. 4.5, the components of the prior Fisher information matrix are

$$\begin{aligned} J^{Prior}_{x,y}(s[x']) &= E\left(\frac{\partial}{\partial s[x]}\log\{f(s[x'])\}\right)\left(\frac{\partial}{\partial s[y]}\log\{f(s[x'])\}\right) \\ &= E\left(\frac{100(10\log_{10}(s_{AVE}[x]) - 10\log_{10}(s[x]))}{p^2\ln(10)^2 s[x]}\right) \\ &\quad \left(\frac{100(10\log_{10}(s_{AVE}[y]) - 10\log_{10}(s[y]))}{p^2\ln(10)^2 s[y]}\right). \end{aligned} \tag{C.31}$$

Note that this expression assumes that $s_{AVE}[x']$ is not a function of the true σ^0 image, and so the result is only an approximation.

The prior Fisher information matrix for the prior used in wind field reconstruction in Eq. 7.12 is

$$\begin{aligned} J^{Prior}_{i,j,x,y}(\vec{U}[x']) &= E\left(\frac{\partial}{\partial U_i[x]}\log\{f(\vec{U}[x'])\}\right)\left(\frac{\partial}{\partial U_j[y]}\log\{f(\vec{U}[x'])\}\right) \\ &= E\left(\sum_k \frac{(\sigma^0_{m,k} - \text{gmf}_k(\vec{U}[x']))}{p^2}\frac{\partial \text{gmf}_k(\vec{U}[x'])}{\partial U_j[y]}\right) \\ &\quad \left(\sum_l \frac{(\sigma^0_{m,l} - \text{gmf}_l(\vec{U}[x']))}{p^2}\frac{\partial \text{gmf}_l(\vec{U}[x'])}{\partial U_j[y]}\right). \end{aligned} \tag{C.32}$$

Note that this expression assumes that the mean of the prior $\vec{\sigma}_m$ is not a function of the true wind field. Since the measurements are a function of the true wind, this prior is not independent of the measurements and the result shown above should be used with caution. In order to calculate this Fisher information matrix in practice, numerical integration can be employed. This approach can be quite cumbersome. As a result, the Monte-Carlo method is a practical alternative to calculating the Cramer-Rao bound.

Appendix D

σ^0 Filtering and Inconsistency Correction

This appendix describes an entirely new method for initializing scatterometer wind ambiguity selection, especially for high resolution winds. The new method is analyzed using both real data and simulation. Some limitations and future improvements of the method are considered.

D.1 Method

The new method improves the high resolution ambiguity selection by obtaining a high quality nudging field from the scatterometer data. This field is obtained by spatially low-pass filtering the ultra high resolution σ^0 fields, retrieving the wind, and then correcting the remaining directional inconsistencies in the ML first ambiguity field. The resulting wind field is used to initialize median filter based ambiguity selection for the high resolution ambiguities. Figure D.1 illustrates the overall procedure.

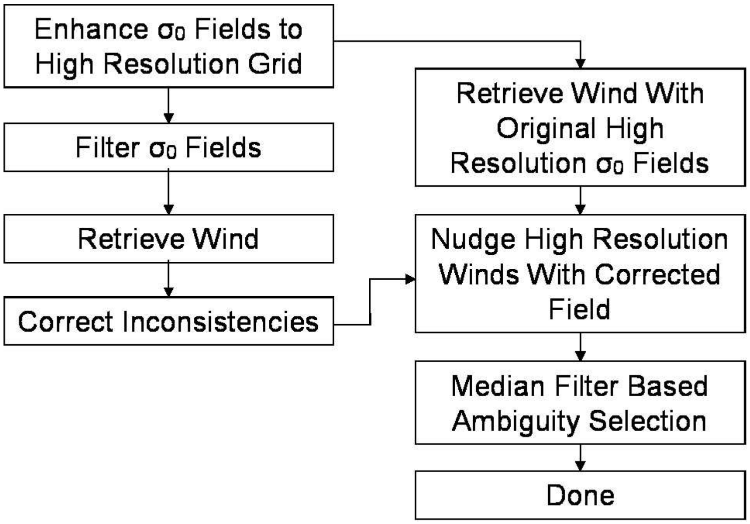

Figure D.1: Overall procedure of the new SFIC algorithm.

D.1.1 Resolution Enhancement

For the new method, the first step in obtaining a high quality nudging field is to enhance the resolution of the σ^0 fields obtained by the scatterometer. This paper employs the UHR method described in Chapters 2 and 5 to improve the spatial resolution to 2.5 km for each of the four azimuth looks.

D.1.2 Backscatter Filtering

Given the enhanced resolution σ^0 fields, the first step to obtain an initializing field is to spatially low-pass filter or smooth each high resolution σ^0 field separately. This reduces the variability of the ML estimate and results in a higher quality first ambiguity wind field.

A weighted averaging filter used is

$$\hat{\sigma}_0(m,n) = \frac{\sum_{i,j=-s}^{s} W(m+i,n+j)\ \sigma^0(m+i,n+j)}{\sum_{i,j=-s}^{s} W(m+i,n+j)} \tag{D.1}$$

where s controls the filter size and W is a weighting function that takes on the values of 1 if the measurement is over the ocean and 0 if it is over land. This ensures that measurements near coastal regions are not biased by land. Furthermore, the filter preserves the dense spatial sampling (2.5 km/vector) in order to aid high resolution nudging and promote a higher spatial correlation. Next, point-wise wind retrieval is performed on the smoothed σ^0 data at 2.5 km/pixel. This results in four ambiguities where the first ambiguity (ML wind estimate) is improved.

Several factors constrain the size of the low-pass filter. The power of the wind falls off approximately as k^{-2} [69]. Since the backscatter is approximately proportional to the magnitude of the wind squared, the backscatter falls off as approximately k^{-1}. Low-pass filtering the σ^0 fields destroys some high frequency information about the wind, thus degrading the resolution. Therefore, there is a trade-off between resolution and noise when choosing a filter size. However, by only using the lower resolution field to initialize a selection algorithm with the original high resolution ambiguities, the high resolution is preserved while loosely constraining the result to be consistent with the low resolution estimate.

D.1.3 Inconsistency Correction

Even after filtering the σ^0 fields, the resulting ML first ambiguity wind field generally contains regions of directional discontinuities or inconsistencies. Therefore, the second step in the method is an inconsistency correction (IC) procedure. The IC procedure is similar to the method described by Draper and Long [70]; however, the dilation phase is modified to favor concave edges. The IC procedure begins by searching out and flagging inconsistencies in the σ^0-filtered ML wind field. After flagging the inconsistent vectors, a series of dilations and erosions are performed to flag inconsistent regions. The flagged regions are then flipped 180 degrees and the result is median filtered. This process is repeated until a maximum number of iterations is performed. The resulting field is smooth and more consistent. Thus, the new σ^0-filtering with inconsistency correction (SFIC) method produces a high quality nudging field for the high resolution ambiguities.

D.2 Analysis

Actual and simulated data are employed to explore the effectiveness of each phase of the algorithm and to choose tuning parameters. High resolution wind simulation is employed to provide a truth data set with which the results of the SFIC method can be compared.

In order to validate the method, the algorithm is applied to various real data sets and compared with results obtained by the other techniques, including conventional low resolution winds and numerical weather prediction models. The new procedure produces more reliable high resolution wind field estimates.

D.2.1 Simulation

In order to determine the error between the SFIC and the true winds, a high resolution geostrophic wind simulation is implemented. The synthetic "true" wind is derived by constraining the magnitude of the Fourier transform to fall off as k^{-2} and generating a random phase [71]. This synthetic wind field is used to simulate noisy σ^0 fields on which the new method is applied.

Simulation is utilized to determine the optimal parameter settings of the SFIC algorithm, and then the effectiveness of the procedure with the optimal parameter settings is tested extensively. The IC procedure is done on both the original high resolution and the filtered σ^0 wind fields. Table D.1 shows the average percentage and RMS error of vectors closest to the simulated wind for several steps in the algorithm.

Table D.1: Percentages of vectors closest to the true wind field and RMS error from true wind for the inner portion of the swath (averaged over 100 realizations).

Category	Percent Closest	
	No σ^0 Filter	σ^0 Filter
1^{st} Ambiguity (skill)	57.0 %	78 0%
Median filtered 1^{st} ambiguity	66.5%	87.0 %
Inconsistency corrected	63.2 %	87.8 %
High resolution result	63.2 %	88.1 %

Category	RMS Error	
	No σ^0 Filter	σ^0 Filter
1^{st} Ambiguity (skill)	24.5	17.3
Median filtered 1^{st} ambiguity	23.8	12.0
Inconsistency corrected	23.1	9.5
High resolution result	23.1	12.1

Filtering the σ^0 fields dramatically improves the skill (the percentage of vectors that are closest to the "true" wind) in high resolution retrieval from about 60% to about 80%.

Although merely applying a median filter-based ambiguity selection procedure results in about the same percent of vectors closest to the true wind as performing the IC procedure (87 percent), the IC procedure reduces the RMS error, suggesting that the SFIC result is closer to the "true" wind. Finally, the SFIC high resolution result chooses about 88% of the ambiguities closest to the true wind.

These results assume a simple rain free geostrophic wind model and the results applied to real data may differ. However, the simulation suggests that the SFIC method is an appropriate method for high resolution ambiguity removal.

D.2.2 Validation

Lacking high resolution "truth" data for validation, the effectiveness of the algorithm is validated by applying it to several cases of real data and comparing the results with the low resolution L2B results and the Numerical Weather Prediction (NWP) winds. Two different weather prediction winds are used: the National Center for Environmental Prediction (NCEP) winds and the European Center for Medium-Range Weather Forecasting (ECMWF) winds. Both hurricane and non-hurricane cases are considered.

For regions not containing hurricanes, the SFIC algorithm is applied to several sets of QuikSCAT data and the results are compared to the L2B, NCEP and ECMWF winds for different wind speed regimes (less than 5 m/s, between 5 and 15 m/s, greater than 5 m/s, and all wind speeds). The percent of high resolution ambiguities closest to the L2B, NCEP, and ECMWF winds that are the same as the SFIC high resolution result are computed. Table D.2 shows the results of the comparison and Figure D.2 illustrates an example of the L2B and the SFIC results for a non-storm region and for a small storm.

About 89 percent of the SFIC high resolution winds are the same as the ambiguities closest to the model winds and the L2B winds. The L2B and NWP winds agree very well with the SFIC low resolution winds for typical wind speed regions (wind speeds less than 15 m/s), choosing about 90 percent of the same high resolution ambiguities. For the stormy regions and regions of high wind speed the L2B winds differ from the SFIC winds; however, the difference is relatively small and both methods choose close to 80 percent of the same high resolution ambiguities. This suggests that the SFIC method produces a suitable nudging field for high resolution wind fields.

The difference between the SFIC winds and the L2B and NWP winds at high wind speeds could be due to several factors. The NWP estimates often spatially mislocate storms and regions of high wind speeds. Furthermore, rain contaminates the scatterometer-derived wind estimates making the speed appear higher and modifying the direction; however, the σ^0 filtering may ameliorate this effect.

For hurricane cases, the NWP and L2B winds are compared with the SFIC winds along with characterizing features of the wind (such as the eye of a hurricane whose location can be determined strictly from the high resolution speed field). Figure D.3 illustrates one hurricane example where the SFIC method produces a more accurate estimate of the hurricane eye than the L2B winds, although their remains a cross swath bias in some regions that is indicative of rain contamination. Thus, the SFIC method can improve the nudging field over the L2B winds even in storm and hurricane cases, but further investigation must be done to explore rain effects.

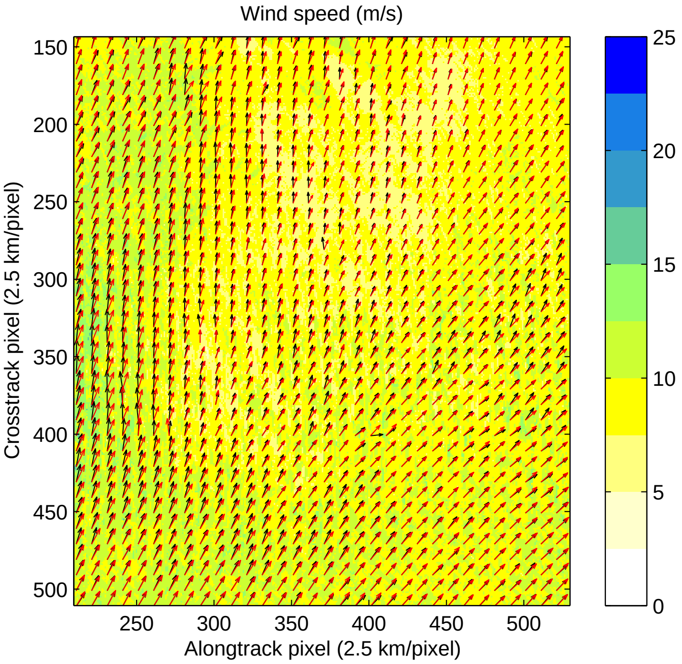

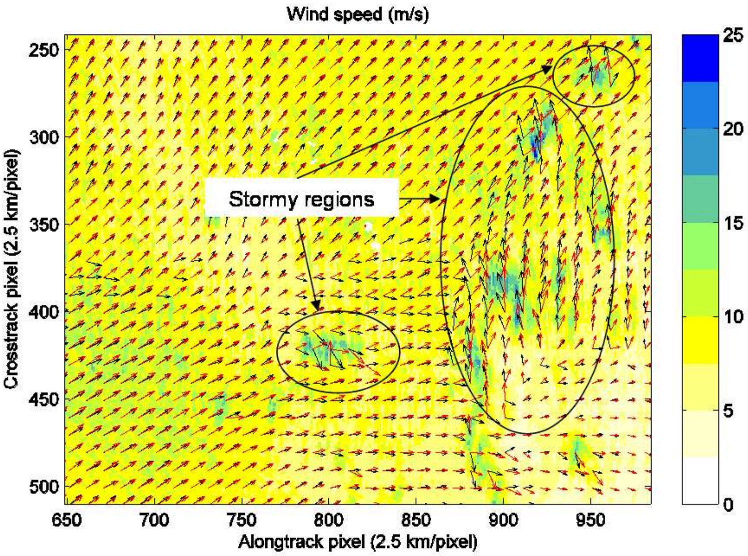

Figure D.2: L2B and SFIC low resolution results for a non-storm (top) and for a small storm (bottom) derived from σ^0 data obtained by QuikSCAT. The red vectors are the L2B winds, The black vectors are the down sampled SFIC low resolution winds. The SFIC low resolution result matches the L2B result very well everywhere but in the stormy regions where rain could be contaminating the ML estimate of the filtered σ^0 fields.

Table D.2: Percentage of cells were SFIC method chooses the same high resolution ambiguities as nudging with the L2B or NWP winds.

	Percent Same			Total cells in bin
	L2B	NCEP	ECMWF	
S<5 m/s	90.5%	90.8%	96.2%	41450
5≤S<15 m/s	91.4 %	90.6%	90.2 %	1074136
S≥15 m/s	78.5%	78.4%	78.3 %	219530
All speed bins	89.9%	89.2%	88.9%	1335382

D.3 Conclusion

Backscatter filtering combined with inconsistency correction can produce high quality initializing fields for ultra high resolution ambiguity selection that are independent of external data. Filtering the backscatter fields improves the high resolution ML estimator because it reduces noise. However, even in a noise-free environment, inconsistencies complicate ambiguity removal. Fortunately, these inconsistencies have structure and can often be corrected.

Simulation methods confirm that this ambiguity selection method performs well in the inner portion of the swath. The SFIC method strongly agrees with NWP winds for wind speeds less than 15 m/s but differs for high winds and hurricane cases, thus validating the new method for the majority of ocean surface wind fields. Furthermore, in some hurricane cases the new method even improves the L2B winds as a nudging field, although heavy rain seems to remain a problem.

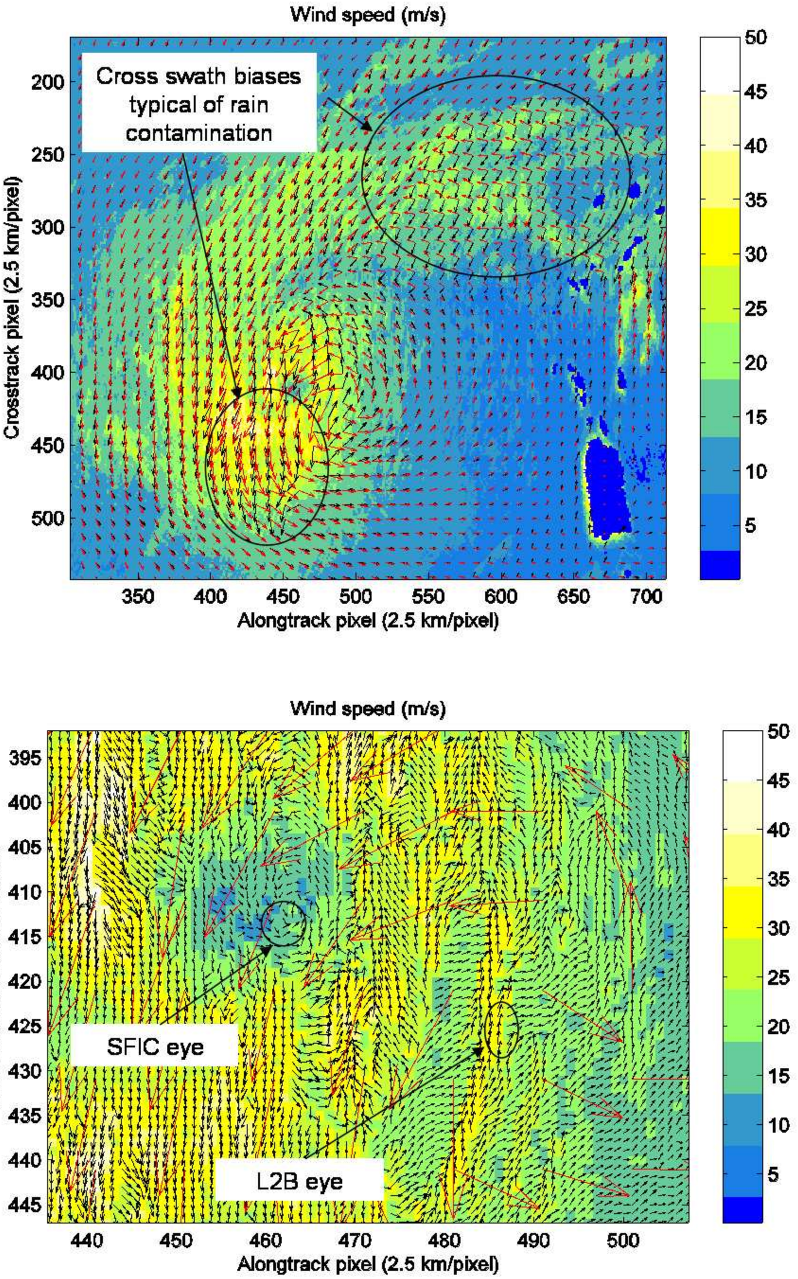

Figure D.3: Hurricane Floyd example in swath along-track/cross-track coordinates. North is approximately to the left. The image on the top shows the large scale view of the storm. Land is shown in dark blue. The bottom image is an expanded view of the eye area. On both images red vectors represent the L2B winds. For the top figure the black vectors are the down sampled SFIC low resolution winds while for the bottom figure the black vectors are the noisy SFIC high resolution winds. Although there exists a cross swath direction bias that is typical of rain contamination, the SFIC method produces a better estimate of the hurricane eye location than the L2B winds for this case.

Appendix E

Resolution

The notion of ‘resolution’ is not a well-defined concept. In different applications, different meanings are associated with the term. For example, a bandlimited signal can be said to have a resolution (temporal or spatial) defined as one over the band limit, since it requires samples with spacing at least this fine to exactly represent the signal by samples. Also, the resolution of an image may be defined as the pixel spacing required to distinguish any two lines or points raised at least 3 dB above the background image.

The resolution of a random process can be defined by the *width* of the power spectrum or correlation function, which indicates how a sample at a particular location is related to the samples at other locations [72]. A random process also has a measurement resolution (sometimes called radiometric resolution) defined by the *height* of the covariance, which is a measure of uncertainty around the mean.

The above notions of resolution are properties of *signals*. When a signal is passed through a filter (or an operator), the resolution of the output is modified by the filter. Filters can impose a resolution on signals that pass through them. A notion of the resolution of a linear operator or filter is the width of the impulse response, which indicates how the portion of a signal at a particular location is spread out by the filter. Note that if the filter is not shift invariant, the resolution may change as a function of where the impulse is centered. For discrete linear operators, this leads to the notions of sampling resolution (or pixel resolution) and effective resolution. The pixel resolution of a discrete linear operator is the pixel spacing corresponding to the highest resolution impulse response, and the effective resolution varies with location.

A symmetric linear operator has a spectral resolution defined by the eigenvalue decomposition, which provides a linear basis that spans the range space of the operator with the eigenvalues indicating how the components of a signal are scaled by the operator. For discrete linear operators, the notion of spectral resolution can be extended to non-symmetric operators using singular value decomposition.

Now consider the case where we have a signal with noise that can be expressed as a deterministic signal plus a zero-mean random variable. When filtering such a random process, the filter imposes structure on both the spatial resolution and the measurement resolution (i.e., both the signal and noise are filtered). The correlation of the signal and the covariance of the noise are both generally modified by the filter. If the filter is linear, the same structure is imposed on both the signal and the noise, but if the filter is nonlinear the noise may be filtered differently than the signal. The relationship between the mean of the input and the mean of the output can be considered the filter response applied to the signal, while the relationship between the zero-mean random variable on the input and zero-mean random variable on the output can be thought of as the filter response applied to the noise. If the filter is linear, then the output of the filter of the sum of the signal and noise is the same as the sum of the output of the filter on the signal-only component and the output of the filter on the noise-only component (i.e., the signal and noise are filtered the same). With a nonlinear operator, the output of the sum of the inputs is not the sum of the outputs of the signal and noise. There are generally cross terms and coupling between the signal and noise, which can be represented as different filtering operations on the signal and the noise.

For this appendix, we are interested in the effective resolution imposed by the sampling and estimation operations of the scatterometer σ^0 imaging and wind estimation problems. Since the reconstruction estimators for the σ^0 imaging and wind estimation problems are difficult to express explicitly as an operator, we develop methods to estimate the filter response from input/output relationships. First, we consider linear shift-invariant operators and linear shift-varying operators. Then, nonlinear operators are investigated. Only the discrete cases are considered.

E.1 Linear Shift-invariant Operators

Suppose that the sampling operation and the estimator are both linear and shift invariant. This corresponds to sampling with the same aperture function shifted regularly in time or space. The operation defined by the sampling operation followed by the reconstruction operation can be expressed as a linear shift-invariant filter with impulse response $h[x]$. The estimate or output $\hat{s}[x]$ can be expressed as a convolution of the input $s[x]$ with the impulse response, i.e.,

$$\hat{s}[x] = \sum_{x'} h[x - x']s[x']. \tag{E.1}$$

Although for the linear case it may be possible to obtain the filter response of the sampling operator and estimator analytically, we take an approach that is later extended to the more difficult nonlinear case. Note that a known signal can be put into the filter and the filter response can be estimated from input/output relationship using standard transfer function methods [42]. That is, the convolution in time/space becomes multiplication when a Fourier transform is applied. Thus,

$$\hat{S}[\omega] = H[\omega]S[\omega] \tag{E.2}$$

where $\hat{S}[\omega]$, $H[\omega]$, and $S[\omega]$ are the Fourier transforms of $\hat{s}[x]$, $h[x]$, and $s[x]$ respectively. For frequencies where the spectral response of the input $s[x]$ is non-zero,

$$H[\omega] = \frac{\hat{S}[\omega]}{S[\omega]} \tag{E.3}$$

and an estimated filter response can be found as the inverse Fourier transform of $H[\omega]$.

A measure of spatial resolution can be obtained as the 'width' of the correlation function of the filter response. The correlation R_h is defined as $R_h = \sum_{x'} h[x]h[x + x']$ and can be obtained by taking the inverse Fourier transform of $H[\omega]H^*[\omega]$ where $*$ denotes the conjugate. The width of the correlation function can be defined in many ways. If x is a two-dimensional index as it is with scatterometry, the width may be different in different directions (i.e., the correlation function may be long in one direction and narrow in another).

A particular measure of resolution that can handle the resolution being different in different directions is to take the second central moment of a scaled magnitude of the correlation function. More precisely,

$$\Delta_r = \sum_x (x - x_0)(x - x_0)^T \frac{|R_h[x]|}{\sum_x |R_h[x]|} \tag{E.4}$$

where x_0 is the location of the maximum of the correlation function. Note that for multidimensional x, Δ_r is a matrix whose eigenvalues indicate the correlation length in the dominant directions and the eigenvectors indicate the directions.

E.2 Linear Shift-varying Operators

Now suppose that the aperture functions are different for different samples, but the sampling and reconstruction estimators are still linear. The effective filter is then a linear shift-varying filter and the input/output relationship can be represented as

$$\hat{s}[x] = \sum_{x'} h[x, x']s[x'] \tag{E.5}$$

which can be expressed as

$$\hat{\vec{s}} = \mathbf{H}\vec{s} \tag{E.6}$$

where $\mathbf{H}$ is a matrix, and $\vec{s}$ and $\hat{\vec{s}}$ are the vectorized versions of $s[x]$ and $\hat{s}[x]$ respectively. Estimating the filter response for this case is a system identification problem that has N^2 parameters to estimate, where N is the number of samples of the signals. Generally, a shift-varying filter cannot be identified from only one input/output relationship. Several inputs (e.g., impulses at every sample location) may be used to identify the response of the filter. This results in a correlation function that varies in time/space (i.e., the correlation function can be expressed as $R_h[x, x']$). The effective resolution can be defined a similar way as above

$$\Delta_r[x'] = \sum_x (x - x_0)(x - x_0)^T \frac{|R_h[x, x']|}{\sum_x |R_h[x, x']|}. \tag{E.7}$$

Note that for a multidimensional x, this definition results in a matrix that indicates resolution in different directions that potentially vary with location.

E.3 Nonlinear Operators

The notion of resolution of a nonlinear filter is difficult to express. Here, some nonlinear extensions of the linear concept of resolution are developed.

Note that for any *one* input/output relationship from a nonlinear operator, there exists a linear operator with that same relationship. We can analyze the resolution of the linear operator and assume the results apply to the nonlinear operator, but there are some severe limitations to this approach. First, there may be several linear operators with the same input/output relationship, resulting in ambiguous results for the resolution. Furthermore, if the input is changed, the corresponding linear operator is also changed (i.e., we only have one input/output relationship for each linear version of the nonlinear operator). Since a shift-varying filter requires several input/output relationships to estimate the filter response, shift-varying filters cannot be analyzed without imposing some more constraints on the system identification problem.

A few approaches can be taken to obtain a metric for the resolution of a nonlinear operator. For a given input signal, the system can be assumed to be linear and shift invariant, allowing the filter response to be obtained from a single input/output relationship. With this assumption, a unique linear filter can be estimated using the transfer function method described above. This results in a correlation function that does not vary in time/space, but is a function of the input signal. The resolution can be expressed as

$$\Delta_r(s[x]) = \sum_x (x - x_0)(x - x_0)^T \frac{|R_h(x, s[x])|}{\sum_x |R_h(x, s[x])|}. \tag{E.8}$$

This resolution metric is appropriate for nonlinear systems that when linearized around $s[x]$ vary slowly over the time/space window of the data.

For scatterometer sampling and reconstruction, the aperture functions vary significantly over the swath, and thus a more suitable assumption may be applied to obtain a measure of the effective resolution as a function of swath location. For example, the swath may be partitioned into small, overlapping chunks and the same approach described above may be applied to each chunk. That is, over the smaller chunks the system is assumed to be linear and shift invariant and the effective resolution $\Delta_r(s[x])$ is calculated for chunks of data centered at each location x'. This results in a resolution metric that varies in location and with the signal

$$\Delta_r(x', s[x]) = \sum_x (x - x_0)(x - x_0)^T \frac{|R_h(x, x', s[x])|}{\sum_x |R_h(x, x', s[x])|}. \tag{E.9}$$

This method is similar to time/frequency analysis (i.e., it is an application of the short-time Fourier transform) and other time frequency analysis methods may also be applied [73]. Note that it may be useful to average out the signal dependence from the effective resolution to obtain a result similar to the linear case (i.e., independent of the signal). This can be done by assuming a distribution for the signal and taking the expected value of the effective resolution.

The above expressions for effective resolution of a nonlinear operator indicate how the signal is filtered by the operator. When noise is added to the aperture-filtered samples before reconstruction, the noise may be filtered differently than the signal. A measure of the effective spatial resolution of the noise is contained in the covariance of the estimates. The covariance of the estimates is a matrix and each row is a correlation function that indicates how the noise of the estimate at a particular location is correlated with the estimates of other locations. The noise correlation length indicates how the noise gets spread by the estimator and may vary from row to row (i.e., the effective noise resolution may vary in time/space). Note that if the noise is correlated on the input of the estimator, the covariance of the estimates contains information about the original noise correlation and the correlation imposed by the estimator. For the scatterometer noise model, the noise is uncorrelated on the input to the estimators and so the covariance of the estimates is an indicator of the effective resolution of the estimator on the noise. Note also that the effective resolution of the noise may be used as a rough indicator of the effective signal resolution imposed by the estimator, since in the linear case they coincide.

The covariance of the estimates can be estimated using Monte-Carlo simulation and estimates of the effective resolution of the noise may be derived. This results in the same expression as in Eq. E.9, but replacing $R_h(x, x', s[x])$ with the the row of the covariance matrix corresponding to location x'.

As noted above, when filtering a noisy signal with a nonlinear operator, the noise and signal become coupled. In fact, the effective filter response on the signal may be different from the filter response on the same signal when noise is introduced. Thus, in the definition of the effective signal resolution defined in Eq. E.9, the correlation $R_h(x, x', s[x])$ is obtained from input/output relationship between the input signal and the mean of the output.

Another approach may be applied to obtain a measure of resolution of a nonlinear operator if a functional form can be found. If we have a function form for the nonlinear operator, it can be linearized around a nominal signal and standard linear operator analysis can be applied directly to the linearized operator for all signals within a ball of the nominal signal.

Appendix F

Coherent and Incoherent Applications

The reconstruction procedure developed in Chapter 3 applies not only to scatterometers, but for general microwave imaging applications. Imaging from either passive or active systems, or coherent or incoherent systems, can be approached as reconstruction from aperture-filtered samples. This Appendix considers fully coherent reconstruction from synthetic aperture radars, and fully incoherent reconstruction from microwave radiometers.

F.1 Coherent Detection and Synthetic Aperture Processing

Although scatterometers apply pulse compression or range/Doppler processing to partition each pulse into several slice σ^0 measurements, the sampling operation is assumed to incoherently integrate in space (i.e., magnitude sum) the responses from all of the targets weighted by the spatial response functions of the slice measurements. Incoherent integration is only an approximation and leads to significant fading and increases the variability in the noise model. In reality, the backscattered signals of different targets interfere because the signals are integrated coherently (i.e., complex linear sum) over the aperture functions. If we have a radar that detects the magnitude and phase of the incoming signal (or the output of the range/Doppler matched filter) rather than only the squared magnitude (i.e., power law detection) it is possible to reduce fading and produce an image with lower noise power. This is the basis behind synthetic aperture radar (SAR).

SAR is a special case of reconstruction from aperture-filtered samples. The received baseband signal from a coherent radar can be expressed as [74]

$$y(t) = \int |G(x,t)|^2 a\left(t - \frac{2R(x,t)}{c}\right) e^{-j\theta(t-\frac{2R(x,t)}{c})}\sigma(x)e^{-j\psi(x)}dx \tag{F.1}$$

where $R(x,t)$ is the range to the resolution cell centered at location x at time t, $|G(x,t)|^2$ is the two way antenna gain pattern which shifts as a function of time, $a(t)$ is the pulse amplitude modulation, $\theta(t)$ is the phase modulation, $\sigma(x)$ is the magnitude of the radar cross section at location x and $\psi(x)$ is the phase. The antenna pattern and the pulse modulation can be lumped together producing the linear sampling operation

$$y(t) = \int A(x,t)\sigma_c(x)dx = \mathcal{A}(\sigma_c(x)) \tag{F.2}$$

where $\sigma_c(x)$ is the complex radar cross section. Generally, a radar digitizes $y(t)$ by sampling and in SAR processing each resolution element is assumed to have one isotropic scatterer at the center of the cell. Thus, the operation becomes a discrete linear operation which can be expressed as a matrix equation $\vec{y} = \mathbf{A}\vec{\sigma_c}$. Every SAR processing algorithm is effectively a method of inverting $\mathbf{A}$ (or a slightly modified version) that imposes some assumptions on the matrix to make the inversion fast.

Note that some SAR systems may not actually sample the complex base-band signal. For example, linear frequency modulated systems often multiply the incoming signal with a shifted version of the transmitted chirp, low-pass filter the result, and then sample the wave form. The sampled waveform of such a system can be expressed as the complex samples of the output of a matched filter (or samples of the Fourier transform of the output of a matched filter). The relationship between the sampled waveform and the σ_c image for this case, and for any preprocessing done in hardware, is generally expressible as a matrix equation $\vec{y} = \mathbf{A}\vec{\sigma_c}$, where $\mathbf{A}$ and $\vec{y}$ may be different than above.

The noise of a coherent radar can be approximated as a white, zero-mean complex-Gaussian random process and so the Moore-Penrose pseudo-inverse of $\mathbf{A}$ (or the least squares pseudo-inverse if the system is overdetermined) is the optimal reconstruction estimator and effectively does the matched filtering and the reconstruction in the same step. Alternatively, the speckle, which is caused by fading and the assumption that each resolution element has one isotopic scatterer, may be modeled as a noise process and a reconstruction estimator can be obtained that minimizes speckle.

Note that in conventional SAR systems, the matrix A has a very special structure which makes it possible to calculate the Moore-Penrose pseudo-inverse very efficiently using standard SAR processing methods. However, when there is significant deviation of the platform from the nominal trajectory, artifacts result in the conventional SAR processed image. Motion compensation methods have been successfully implemented at the cost of complexity and increased processing time. For the motion compensation case, it may be beneficial to apply an iterative method, such as a gradient search of the ML or MAP objective function, to recover the SAR image from the raw measurements. The computations required for a gradient search method are NML where N is the number of image pixels, M is the number of measurement samples, and L is the number of iterations. Although many iterations L may be required for the gradient search to converge, it may be possible to obtain a sufficiently focused image that can account for nonuniform motion with relatively few iterations. This approach can be applied as an iterative form of the computationally taxing back-projection algorithm.

F.2 Fully Incoherent Reconstruction: Application to Radiometry

A microwave radiometer is a passive device that measures the microwave emissions from the Earth's surface. Since radiometers are passive, they cannot employ pulse compression or range/Doppler processing, and each measurement can be approximated as the inner-product of the antenna gain pattern with the emissions from many particles on the Earth's surface and atmosphere. For low frequencies, the contributions from the atmosphere can be neglected, while for higher frequencies atmospheric effects may be significant.

Assuming incoherent integration results in a residual cross term that acts as a fading random variable. This can be represented as a zero-mean Gaussian random variable with a variance that is a function of the signal magnitude, similar to the scatterometer problem.

The measurement that is often of interest in radiometry is the brightness temperature T_b. However, radiometers measure a quantity called the apparent brightness temperature T_{AP} that has contributions from upwelling and reflected down-welling from the atmosphere. The measured T_{AP} is related to the apparent brightness temperature from the each point on the Earth as

$$T_{AP,i} = \int T_{AP}(\theta_i, \phi_i) G(\theta_i, \phi_i) d\Omega + \nu_i \tag{F.3}$$

where θ_i and ϕ_i are the azimuth and incidence angle of the i^{th} measurement, and ν_i is a zero-mean Gaussian random variable with variance ΔT where ΔT is a function of the system noise, the amplifier gain uncertainties, and the signal. $T_{AP}(\theta_i, \phi_i)$ represents the contributions from emitters from the surface and the atmosphere and can be expressed as [68]

$$\begin{aligned} T_{AP}(\theta_i, \phi_i) &= T_{AP}(\theta_i, \phi_i, 0) + \textstyle\int_0^r T_{AP}(\theta_i, \phi_i, r')dr' \\ &= T_{AP}(\theta_i, \phi_i, 0) + \textstyle\int_0^r \kappa_e(\theta_i, \phi_i, r')[(1-a)T(\theta_i, \phi_i, r') + aT_{SC}(\theta_i, \phi_i, r')]dr' \end{aligned} \tag{F.4}$$

where r is the range from the surface of the Earth to the radiometer, κ_e is the extinction coefficient, a is the albedo, T is the physical temperature, and T_{SC} is the scattering temperature. Note that if atmospheric effects are negligible, $T_{AP}(\theta_i, \phi_i) = T_{AP}(\theta_i, \phi_i, 0)$.

If atmospheric effects are negligible and the emitters are assumed to be isotropic, each $T_{AP,i}$ measurement can be expressed as

$$T_{AP,i} = \int T_{AP}(x) A_i(x) dx + \nu_i \tag{F.5}$$

where x is a two-dimensional spatial variable on the Earth's surface, and $A_i(x)$ is the antenna gain pattern of the i^{th} measurement projected on the Earth's surface. The multiple measurements can be stacked into a vector resulting in

$$\vec{T}_{AP} = \begin{bmatrix} \int T_{AP}(x) A_1(x) dx + \nu_1 \\ \vdots \\ \int T_{AP}(x) A_N(x) dx + \nu_N \end{bmatrix} = \mathcal{A}(T_{AP}(x)) + \vec{\nu}. \tag{F.6}$$

Since the antenna has finite length and the far field antenna pattern is approximately the Fourier transform of the near field, the antenna gain pattern can be assumed to be bandlimited and the sampling operator $\mathcal{A}$ can be represented by a discrete matrix operation on conventional samples of $T_{AP}(x)$. That is,

$$\vec{T}_{AP} = \mathbf{A}(T_{AP}[x]) + \vec{\nu} \tag{F.7}$$

where $\mathbf{A}$ is a matrix and the square brackets $[x]$ represent a sampled version of $T_{AP}(x)$.

Neglecting noise, the brightness temperature image can be reconstructed by applying an inverse or a pseudo-inverse of the sampling matrix $\mathbf{A}$. But because of the structure of the noise, a ML or MAP estimator may be more appropriate.

The assumption that atmospheric effects are negligible may be appropriate for lower frequency channels when there is no significant weather; however, rain, water vapor, and oxygen concentrations in the atmosphere can significantly affect the apparent brightness temperature for certain radiometer channels. Imaging of the surface in the manner described above in Eq. F.7 limits the use of some radiometer channels. The higher frequency channels have a higher resolution, but are more limited in observing surface effects. Using each channel to reconstruct some other quantity that is common or related among them may result in a higher resolution image of the surface, as well as a tomographic image of the atmosphere.

Equation F.4 expresses the apparent brightness temperature for each channel as a function of the surface contributions and atmospheric contributions. Note that the surface contributions, the extinction coefficient, the albedo, and the scattering temperature are functions of the physical material and all vary with frequency. The physical temperature, however, is constant with frequency. The contributions from the surface can be approximated as $T_{AP} = \epsilon T$ where ϵ is the emissivity which varies with material and texture, and T is the physical temperature.

A geophysical model function that describes relationship between the type of material (i.e., concentrations of gasses/liquids in the atmosphere, and type of surface material and texture) and the albedo, the extinction coefficient, the scattering temperature, and the surface emissivity can be used to simultaneously estimate all of these quantities with the temperature profile using all channels of the radiometer. Thus, instead of reconstructing T_{AP} for each channel, an ϵ map and temperature map may be reconstructed for the surface, and a three-dimensional tomographic image of κ_e, T_{SC}, and a may be obtained, along with the surface classification and gas concentration maps.